SILICIFICATION ACROSS THE BETZE-POST CARLIN-TYPE AU DEPOSIT: CLUES TO ORE FLUID PROPERTIES AND SOURCES, NORTHERN CARLIN TREND, NEVADA

by

Jared D. Lubben

Bachelor of Science
Winona State University
2000

A thesis submitted in partial fulfillment
of the requirements for the

Master of Science Degree in Geoscience
Department of Geoscience
College of Sciences

Graduate College
University of Nevada, Las Vegas
August 2004

ABSTRACT

Silicification across the Betze-Post Carlin-type Au Deposit: Clues to Ore Fluid Properties and Sources, Northern Carlin Trend, Nevada

by

Jared D. Lubben

Dr. Jean S. Cline, Examination Committee Chair
Professor of Geoscience
University of Nevada, Las Vegas

Ore fluid properties and sources at the Betze-Post deposit, the largest Carlin-type gold system in the world (~ 49 million ounces Au), are not well understood. To improve knowledge of ore fluids, the geochemical, textural, and fluid inclusion characteristics of ore, late-ore, and post-ore quartz associated with Au-bearing pyrite were determined. Various stages of quartz were identified by integrating petrographic, fluid inclusion, oxygen isotope, cathodoluminescence studies, and spatially associated Au-bearing pyrite. Ore stage jasperoid displays CL-dark luminescence and was overgrown by late-ore-stage CL-dark drusy quartz. Multiple generations of post-ore drusy quartz overgrow ore and late-ore quartz and exhibit CL-bright and CL-multiple luminescence. Microthermometry indicates ore stage fluids have low salinities and were trapped between 180°C and 240°C. δD_{H2O} and $\delta^{18}O$ values in ore fluids and quartz, respectively, indicate that ore stage fluids were highly evolved but were diluted by unevolved meteoric fluids with time and as fluids migrated west, as the ore system waned.

TABLE OF CONTENTS

LIST OF FIGURES

ACKNOWLEDGEMENTS

This work was conducted in conjunction with the work of Chris Henkelman of the University of Nevada, Las Vegas under the oversight of Dr. Jean S. Cline of the University of Nevada, Las Vegas.

Major funding for this project was provided by Barrick Gold Corporation, the Ralph J. Roberts Center for Research in Economic Geology (CREG), the Geological Society of America (GSA), the Society of Economic Geologists (SEG), and the UNLV Department of Geoscience.

Microbeam analyses were conducted at the Electron Microanalysis and Imaging laboratory (EMiL) located at the University of Nevada, Las Vegas, under the direction and helpful guidance of Dr. Robert Fairhurst and Dr. Clay Crow. SIMS analysis was conducted at Arizona State University under the direction of Dr. Richard Hervig and Dr. Frank Mazdab. Doubly polished thick sections were produced by Mark Mercer. Hydrogen isotope and conventional oxygen isotope analyses were conducted by Dr. Al Hofstra at the USGS, Denver.

Thanks to the Barrick exploration and mine geology staffs for invaluable discussions of Carlin-type gold systems, Nevada geology, and Elko-life. Thanks to Bob Leonardson, Keith Testerman, and Jerry Rahn for taking me into the Betze-Post pit for descriptions of Betze-Post geology and sample collection. Special thanks to Pam Zohar and Kent Thompsen for assistance during core logging and sample description.

I am particularity indebted Dr. Jean Cline for first, providing me with the opportunity to study at UNLV and to allow me to pursue my interest in ore deposits, and second, for her extensive editing, effective advice, valuable prompts, and support over the last three years. I could not have worked with a more capable, considerate, and helpful advisor.

Finally, I extend my most sincere and loving thanks to Nicole, Chelsie, Royal, Dora, and my parents, and to all of my friends who have stuck with me through all of the curveballs life has thrown my way during my time in Las Vegas. I am most appreciative for your invaluable and loving advice and support. I will always remember what you have done for me!! I owe you one!

CHAPTER 1

INTRODUCTION

The Carlin, Getchell, and Battle Mountain-Eureka trends along with the Alligator Ridge and Jerritt Canyon districts host the Carlin-type gold deposits of northern Nevada (Figure 1). The Carlin trend, one of the world's largest gold districts trends NW to SE and is a 60-km alignment of many Carlin-type deposits including the Betze-Post deposit.

More than one hundred Carlin-type deposits have been discovered in Nevada and, including production, reserves, and resources, they form the largest and most prolific accumulation of gold in North America (NBMG, 1997). The mining of Carlin-type deposits has made Nevada one of the leading gold producers in the world.

This study focuses on answering several important questions surrounding the role of silicification at the Betze-Post Carlin-type gold deposit. Silicification is a primary hydrothermal alteration process in Carlin-type gold deposits and quartz, usually in the form of jasperoid, is precipitated (Bakken & Einaudi, 1986; Arehart, 1996; Hofstra & Cline, 2000). Silicification indicates that ore fluids saturated in silica cooled and, in these deposits, precipitated jasperoid that replaced carbonate host rocks.

Previous paragenetic studies demonstrated that gold mineralization is spatially associated with jasperoid mineralization (Arehart, 1996; Cline and Hofstra, 2000; Hofstra and Cline, 2000). Fluid inclusion studies on quartz indicated that ore fluid temperatures

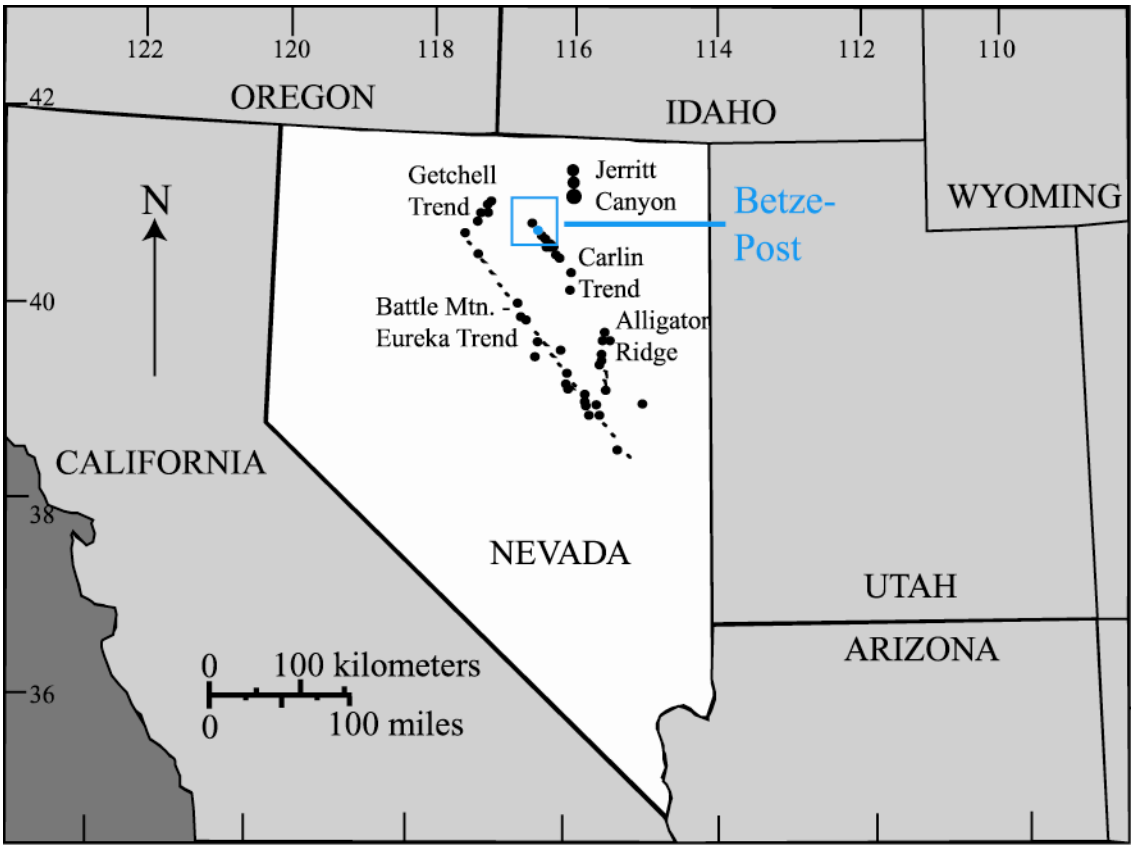

Figure 1. Carlin-type gold deposits in Northern Nevada are hosted within three major trends including the Carlin trend, Getchell trend, and Battle Mountain - Eureka trend (modified from Hofstra and Cline, 2000).

ranged from 180°C to 240°C (Cline and Hofstra, 2000; Hofstra and Cline, 2000). Fluid inclusions in quartz spatially associated with gold have been identified in a few deposits within the Betze-Post system; however, few fluid inclusion data are available from this major Carlin-type system (Hofstra and Cline, 2000). Preliminary electron microprobe analyses of quartz at the Getchell Carlin-type gold deposit suggested that trace concentrations of Al and Fe may be present in ore-stage quartz (J. Cline, personal communication, 2001). Cathodoluminescence studies indicated that quartz of different generations luminesces different colors (Hofstra, 1994; Weaver, 2001; Emsbo, 1999) and support the likelihood of trace element variations in quartz.

Significant advances in understanding the physical properties of Carlin-type gold systems have been made; however, ore fluid origin remains an enigmatic topic. Previous research has indicated that ore fluids for several Carlin-type gold deposits have a meteoric origin (Radtke et al., 1980; Kuehn & Rose, 1992; Emsbo et al, 1999; Emsbo, 1999; Emsbo et al., 2003). However, ore fluids for gold deposits along the Getchell trend have been linked to a deep-seated magmatic or metamorphic origin (Cline et al., 1996; Groff et al., 1997; Cline & Hofstra, 2000; Cline et al., 2002). Mixing between two fluids, one of meteoric origin and the other of a more evolved meteoric origin have also been linked to gold mineralization in Carlin-type systems (Hofstra et al., 1991; Kuehn & Rose, 1992). This study focused on constraining the source of fluids responsible for gold deposition at the Betze-Post deposit.

It is widely accepted that in Carlin-type gold systems ore fluids migrated vertically along high angle faults until contact with less permeable units forced fluids to migrate laterally and react with more permeable and porous carbonate formations. Several ore

zones exist within the Betze-Post deposit with some ore zones proximal to deeply penetrating, high-angle faults that are believed to be major conduits for ore fluids at the Betze-Post deposit. Other ore zones within the Betze-Post deposit are distal to the high angle faults, and little is known in regards to the fluid pathways between ore zones.

This study tested the hypothesis that ore fluids at the Betze-Post Carlin-type gold deposit varied in temperature and produced quartz that is spatially associated with gold, and which has a distinctive chemistry and texture. These variations in temperature coupled with chemically and texturally distinct quartz can be reliable indicators of ore fluid origin and pathways. This study also tests the hypotheses that ore fluids from a deep-seated magmatic, metamorphic, or deeply circulating meteoric source migrated upwards along high angle fault systems and reacted with the Fe in the host rocks to deposit gold.

The goals of this study were three-fold. The first goal was to document variations in quartz chemistry, texture, and fluid inclusion temperature and salinity both laterally and with depth at the Betze-Post deposit. This goal was accomplished by integrating paragenetic, fluid inclusion, trace element chemistry, and oxygen isotope studies. The second goal was to identify ore fluid sources at the Betze-Post deposit by analyzing oxygen and hydrogen isotopic signatures of inclusion fluids in quartz associated with gold mineralization at the Betze-Post deposit. The third goal was to identify ore fluid migration patterns in the Betze-Post deposit to identify possible vectors to ore useful in exploration. Interpreting chemical, textural, and temperature variations between various ore stages at the Betze-Post deposit accomplished this goal.

CHAPTER 2

CHARACTERISTICS OF CARLIN-TYPE GOLD DEPOSITS

Carlin-type gold deposits are defined as sediment-hosted disseminated gold deposits. The majority of Carlin-type systems occur within north-central Nevada; however, several gold deposits, sharing similar characteristics with Nevada Carlin-type deposits, have been discovered in China (Ashley et al., 1991; Mao, 1991), Indonesia (Sillitoe and Bonham, 1990; Garwin et al., 1995), and South America (Alvarez and Noble, 1988) and are described as Carlin-type systems.

In Nevada, Carlin-type deposits occur within the Basin and Range physiographic province. These deposits generally host large low- to medium-grade ore zones with associated high-grade ore zones localized at depth. Ore in Carlin-type systems is typically hosted within Paleozoic silt-rich carbonate rocks; however, occurrences of ore within pre-existing plutonic and volcanic lithologies has been documented (Hofstra and Cline, 2000; Bettles, 2002; Emsbo, 2003).

Gold in Carlin-type deposits is submicron in size and localized within arsenic-rich pyrite grains, which are disseminated within their carbonate host formations. Therefore, gold in Carlin-type systems does not form visible accumulations. The arsenic-rich and Au-rich pyrite commonly occurs as overgrowth rims on younger gold-poor pyrite cores that pre-date Carlin-type mineralization (Wells and Mullens, 1973; Radtke, 1985;

Bakken, 1990; Arehart et al., 1993; Arehart, 1996; Cline and Hofstra, 2000; Cline, 2001; Henkelman, et. al., 2003; Henkelman, 2004). These rims generally display distinct textures that can be used as indicators of higher gold concentrations relative to gold-free Fe-sulfide minerals (Cline and Hofstra, 2000; Cline, 2001; Henkelman et al., 2003; Henkelman, 2004). Gold is commonly associated with a distinct suite of trace elements which include Sb, Hg, Te, Tl, Cu, and Ag (Christensen, 1995; Weaver and Cline, 1999; Wells and Mullens, 1973; Arehart et al., 1993; Cline and Hofstra, 2000; Cline, 2001; Henkelman et al., 2003; Henkelman, 2004).

The age of mineralization in Carlin-type deposits has been difficult to constrain and was widely disputed. The fine-grained occurrence of most ore-stage minerals and enigmatic textural relationships between datable minerals and gold mineralization in these types of systems has stirred significant debate over the age of gold mineralization. However, crosscutting relationships indicate a general acceptance of Late-Eocene age (Hofstra et al., 1999). The best documented age of gold mineralization in Carlin-type systems in north central Nevada is 39.8±0.6 Ma based on Rb-Sr dating of galkhaite, a Hg-Tl-Cs sulfosalt, associated with gold mineralization at the Rodeo Carlin-type gold deposit (Arehart et al., 1993; Bettles, 2002).

Ore fluids in Carlin-type gold systems induced hydrothermal alteration of host rocks, which varies in intensity and produces distinct mineral zoning patterns. Alteration processes associated with Carlin-type gold deposition include carbonate dissolution (Bakken & Einaudi, 1986; Arehart, 1996; Hofstra & Cline, 2000), sulfidation (Hofstra et al., 1991; Arehart, 1996; Hofstra & Cline, 2000), silicification (Bakken & Einaudi, 1986;

Arehart, 1996; Hofstra & Cline, 2000), and argillic alteration (Kuehn & Rose, 1992; Arehart, 1996; Hofstra & Cline, 2000) (Figure 2).

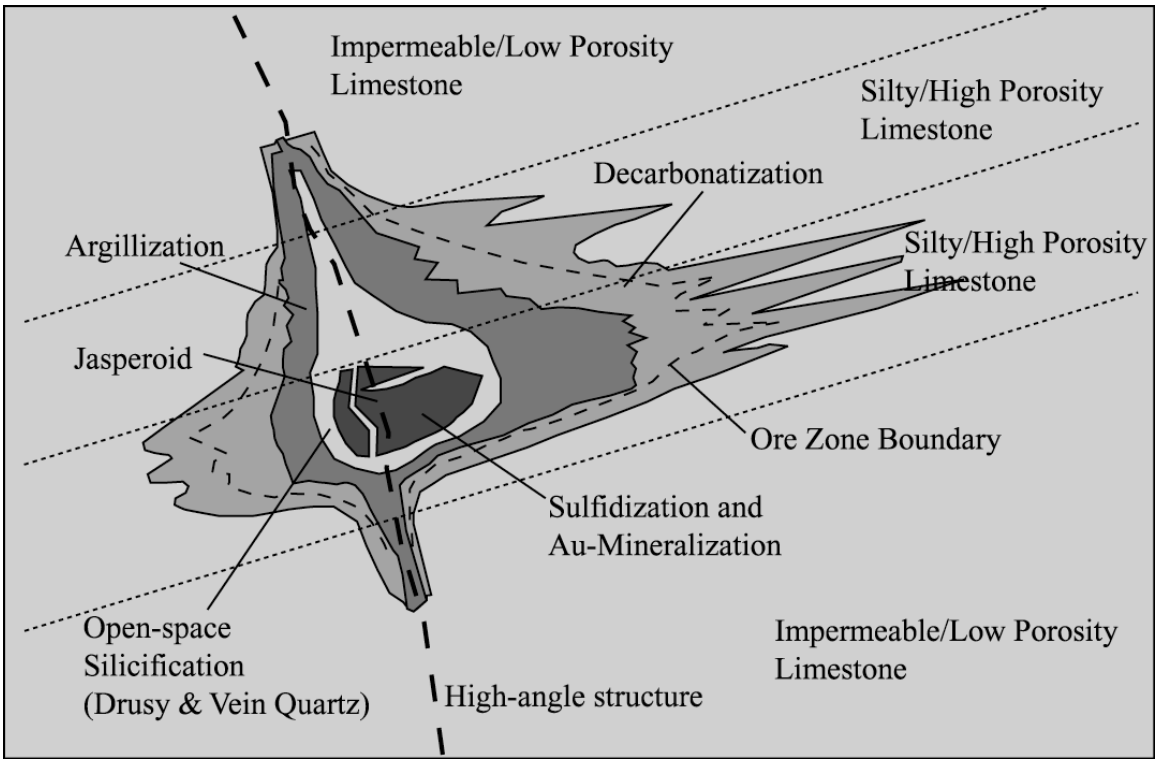

Figure 2. Schematic cross-section through a Carlin-type ore zone illustrating the major alteration and mineralization features adjacent to a fluid conduit. Note the spatial relationship between Au mineralization and silicification types (modified from Arehart, 1996).

CHAPTER 3

THE BETZE-POST CARLIN-TYPE GOLD DEPOSIT

The Barrick Goldstrike property hosts the Betze-Post Carlin-type gold deposit, which is located in the Blue Star-Goldstrike sub-district of the northern Carlin Trend. The Betze-Post deposit is the largest of the many disseminated, sediment-hosted Carlin-type gold deposits in north-central Nevada (Figure 3). The Betze-Post deposit is divided into five sub-deposits including, from east to west, Deep Post, North Post, Betze, North Betze, and Screamer. Production at Betze-Post has accumulated to 49 million ounces of Au at an average grade of approximately 0.360 oz/ton (ounces per ton) Au (Bettles, 2002). As of the end of 2001, reserves at Betze-Post totaled 108.85 million short tons (98.75 Mt) at 0.151 oz/ton (5.18 g/t) of gold, for 16.43 million ounces (511 t) of gold reserves (Bettles, 2002).

Structural Control for the Betze-Post Deposit

Ground preparation for the Betze-Post deposit was initiated by extension produced during Neoprotorozoic rifting. This extension produced high angle normal faults that would become basement structures and control the orientation of subsequent deformation. These later faults may have served as collecting points and conduits for

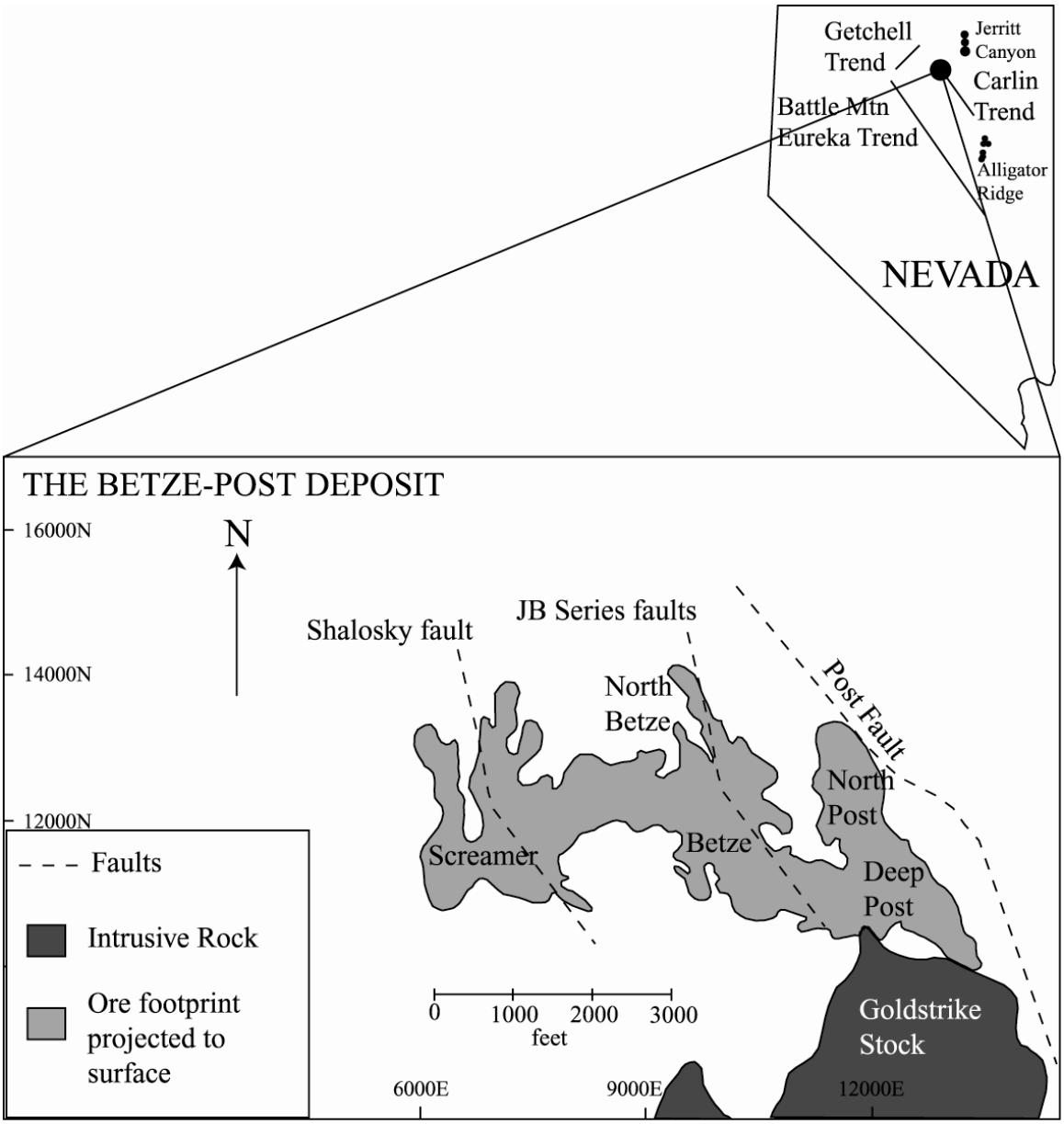

Figure 3. The Betze-Post deposit consists of several ore zones including North Post, Deep Post, Betze, North Betze, and Screamer (modified from Hofstra and Cline, 2000).

later hydrothermal fluids derived from greater depths (Robert, 1966; Tosdal et al., 2000; Grauch et al., 2003).

During Early-Paleozoic time, northern Nevada coincided with the western margin of the North American craton. Subsequent to rifting, a miogeoclinal sequence developed on the trailing continental margin. This early-Paleozoic miogeocline consists of an eastern shallow-water, continental-shelf carbonate facies of limestone, dolomite, and minor shale and sandstone. To the west, an assemblage of offshore, deep water siliceous chert, shale, quartzite, and mafic volcanic rocks interbedded with thin calcareous units was deposited (Stewart, 1980). During loading and the formation of the miogeocline, syn-sedimentary faults that link with underlying basement structures formed and may have hosted reactivation during additional sediment loading or subsequent extension (Cline et al., 2003).

These two suites of rocks were deformed by a series of compressional events including from oldest to youngest the 1) late Devonian through middle Mississippian Antler orogeny (Hotz and Wilden, 1964; Stewart, 1980), 2) the Late-Permian through Early-Triassic Sonoma orogeny (Silbering and Roberts, 1962; Stewart, 1980), 3) the Late-Jurassic Elko orogeny (Thorman et al., 1990, 1992), and 4) the Sevier orogeny during the Late-Cretaceous (Armstrong, 1968). Localized features reflecting or occurring coeval with these compressional regimes are documented at Betze-Post (Leonardson and Rahn, 1996).

Eastward-directed compression associated with the Antler orogeny produced the Roberts Mountains thrust fault. This thrust placed the western assemblage of predominantly siliciclastic rocks over the eastern assemblage of predominantly silty

carbonate rocks (Hotz and Wilden, 1964; Roberts et al., 1971; Stewart, 1980). This compression was integral in the formation of the Betze-Post deposit because it created a localized aquitard by placing less favorable impermeable siliciclastic rocks over more favorable highly permeable, highly porous silty carbonate rocks. Aquitards force fluids laterally away from conduits and into more favorable host lithologies preventing fluids from migrating into the groundwater and venting at the surface (Nutt and Hofstra, 2003).

The Sonoma orogeny forced post-Antler siliciclastic and carbonate formations eastward over the Roberts Mountain allochthon (Silberling & Roberts, 1962; Stewart, 1980). During the Elko orogeny, these rocks were further deformed by local east directed folds and thrusts (Thorman et al., 1990, 1992). These compressional events produced a series of uniformly spaced, regional doubly plunging anticlines with north to north-northwest strikes. These structures cross-cut Betze-Post ore zones and are believed to represent prominent structural traps for gold-bearing fluids (Leonardson and Rahn, 1996).

The latest compression occurred coeval with Jurassic subduction resulting in the emplacement of the Goldstrike intrusive complex (Figure 3). The effects of this compression are evident in folding induced when the Goldstrike intrusive complex penetrated the sedimentary section from the south-southwest toward north-northeast. This stress regime produced local shortening within the primary rock formations that host gold at Betze-Post (Leonardson and Rahn, 1996).

Local Jurassic extension, also associated with the emplacement of the Goldstrike intrusion, re-opened favorably oriented structures and provided permeability needed for ore fluid migration and gold deposition. This extension opened structures related to the previous three tectonic regimes at Betze-Post. Flatter dips on previous fault zones and

low-angle faults over the Goldstrike intrusion to the south are distinct characteristics of this pre-ore tectonic event (Leonardson and Rahn, 1996). This extension, along with uplift and erosion, created windows in the upper plate of the Roberts Mountains thrust fault, locally exposing the lower plate carbonate rocks (Hotz & Willden, 1964; Stewart, 1980).

Late Eocene extension, associated with formation of the Elko Basin, contributed to formation of Carlin-type gold deposits by forming or reopening existing high-angle normal faults, and creating conduits for ore fluids. The Eocene hosted two periods of extension with differing magnitudes with the greater extensional period resulting in extensive reactivation along pre-Eocene structures. The higher magnitude extension was accommodated by a pervasive set of mainly westerly dipping, domino-style faults that sliced the Elko basin into mainly northeasterly to northerly trending fault blocks (Henry et al., 2001; Moore, 2001). Ore fluids are believed to have migrated vertically along these high-angle fault systems until they contacted low permeability aquitards that caused fluids to migrate laterally and react with permeable and porous lower plate carbonate formations.

According to low-temperature-apatite thermochronology studies, exhumation rates during the Eocene were determined for the northern Carlin trend (Hickey, 2003; Hickey et al., 2003). According to these studies, deposits along the northern Carlin trend formed at depths of approximately 2 kilometers.

Comprehensive examination of mineralized structures at the Betze-Post deposit indicates that two primary fault sets controlled gold mineralization. These fault sets include a family of moderate-to steep-dipping, north-northwest striking normal faults and

a family of east-northeast striking normal faults that also have moderate to steep dips (Leonardson and Rahn, 1996). These major structures were primary feeders for ore fluids that deposited Au-bearing sulfide minerals at Betze-Post. The NNW structural feeders include from east to west, the Post fault system, the JB series faults, and the Shalosky Fault (Figure 4). The Post fault system cross-cuts the North Post and Deep Post ore zones and forms their eastern boundary. The JB series faults intersect the Betze and North Betze ore zones while the Shalosky fault crosscuts the Screamer ore zone.

Finally, post-mineralization structural events documented at Betze-Post include 1) local deformation related to contraction of the Carlin hydrothermal system, 2) extension related to Basin and Range normal faulting, and 3) right-lateral strike-slip faulting, which displaced Basin and Range faults (Leonardson and Rahn, 1996). These structural events are products of mid-crustal extension and the exhumation of metamorphic core complexes and induced oxidation and supergene alteration of the Betze-Post deposit. These processes drove fluids along the same fractures that controlled Carlin-type gold mineralization, and are believed to be responsible for post-Carlin mineralogy identified at Betze-Post.

Betze-Post Stratigraphy

The majority of Carlin-type gold deposits are hosted within carbonate facies localized in the lower plate of the Roberts Mountains thrust system (Figure 5). Carbonaceous, silt-rich, limestone facies are the most common host for Carlin-type gold mineralization because these limestone bodies reacted with hydrothermal fluids and the carbonate component was dissolved. This fluid-rock interaction increased permeability and

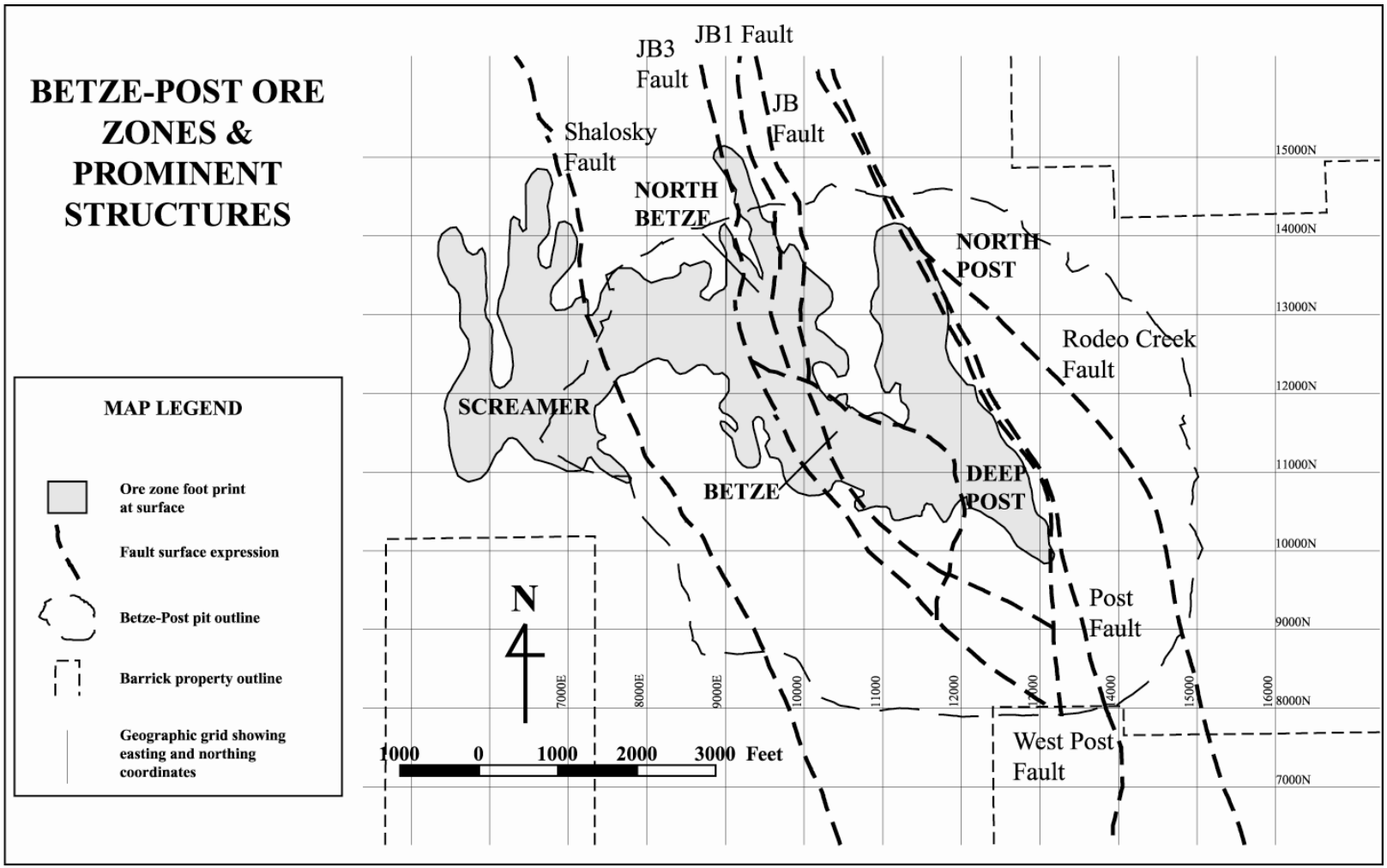

Figure 4. Map illustrates prominent NW to SE trending structures that cross-cut the Betze-Post deposit. These structures are hypothesized to be the primary controls for ore fluid flow throughout the Betze-Post deposit.

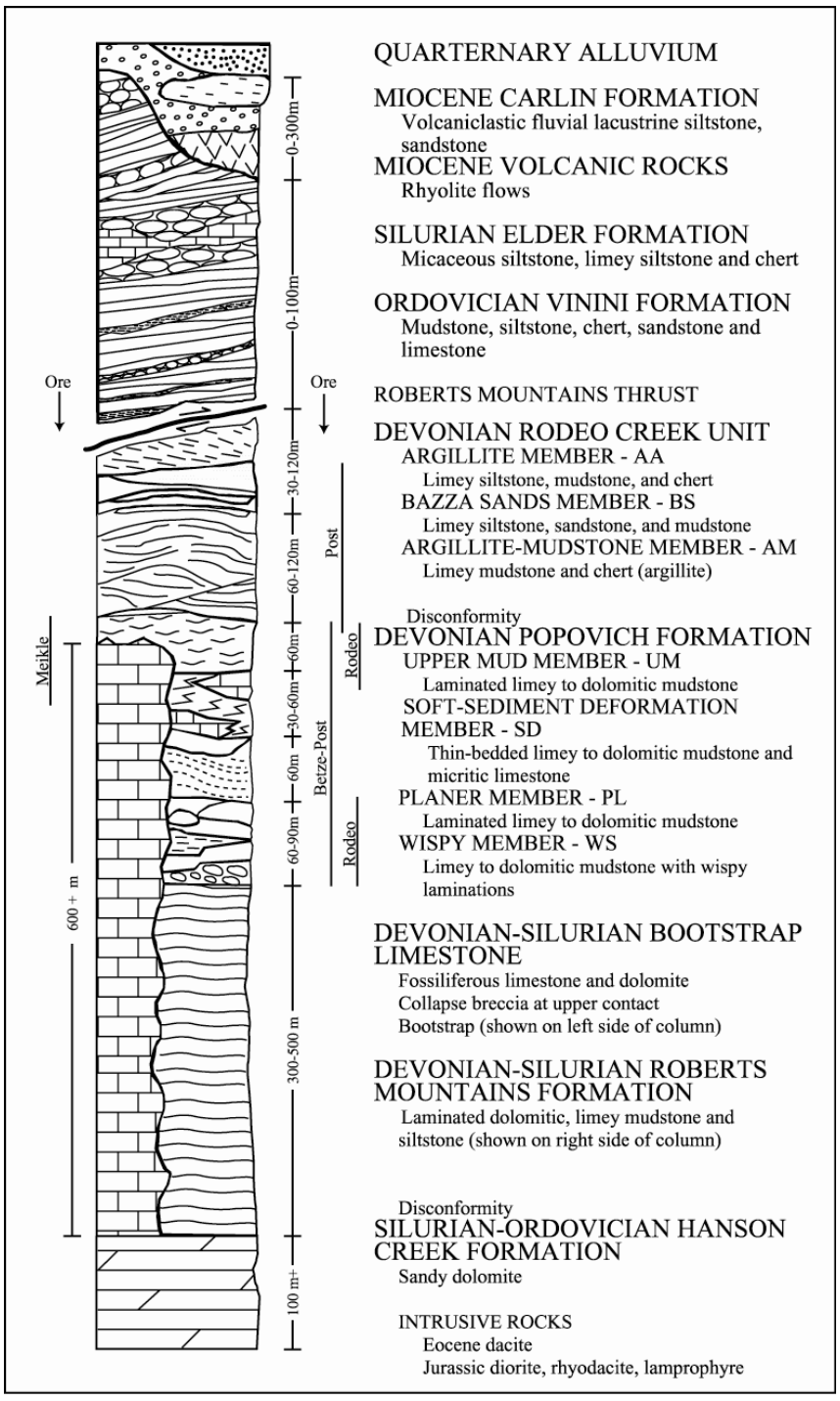

Figure 5. Stratigraphic column of the Betze-Post deposit, showing relationship between major ore bodies and stratigraphic units. Vertical lines indicate stratigraphic host for individual deposits. Modified from Bettles and Lauha (1991) and Volk et. al. (2001).

porosity and produced the open space needed for fluid flow and gold deposition. The Betze-Post deposit lies primarily within the Devonian Popovich Formation, but some ore occurs within the Silurian-Devonian Roberts Mountains Formation and the Devonian Rodeo Creek unit (Furley, 2001; Bettles, 2002).

The Devonian-Silurian Roberts Mountains Formation is a laminated dolomitic lime mudstone to siltstone deposited as turbiditic anoxic basinal facies. A brecciated zone is consistently present along the contact between the upper Roberts Mountains and the lower Popovich Formations. This breccia possesses angular clasts derived from the upper Roberts Mountains Formation and the lower Popovich Formation (Furley, 2001; Volk et al., 2001). This breccia is believed to have formed by a variety of geologic processes including hydrothermal activity, faulting, and diagenetic causes.

The Early to Late Devonian Popovich Formation lies conformably on the Roberts Mountains Formation, and is composed of a sequence of carbonaceous, calcareous, and dolomitic mudstone (Evans, 1980; Furley, 2001; Volk et al., 2001). The Popovich Formation is divided into four separate units that are distinguished by unique sedimentary characteristics. These units include from the base upwards, the Wispy, Planer, Soft-Sediment Deformation, and Upper Mud members (Figure 5).

The Wispy Member represents the lowermost unit of the Popovich Formation and is conformably overlain by the Planer member. The Wispy member is a laminated limy to dolomitic mudstone with distinctive wispy laminations produced by bioturbation (Furley, 2001; Volk et al., 2001). The Wispy member hosts a majority of gold mineralization within the Betze-Post deposit as well as in the other surrounding deposits within the Goldstrike property (Furley, 2001; Bettles, 2002).

The Wispy unit of the Popovich Formation possesses several distinct qualities that make it the most favorable host of ore. Bioturbation zones, debris flows, and sedimentary breccias are common and all are primary features of high porosity that allowed fluids to migrate and promote alteration. The wide range of sedimentary features within the Wispy across the different ore zones at Betze-Post produced wide variability in degree of alteration.

The Planer Member conformably overlies the Wispy Member and is characterized by a laminar limey to dolomitic mudstone. The unit also is free of bioturbation indicating a deeper, more anoxic environment relative to the underlying Wispy unit (Furley, 2001; Volk et al., 2001). The Soft-Sediment Deformation Member is conformably overlain by the Upper Mud Member and is composed of thin- to thick-bedded limey to dolomitic mudstone and micritic limestone. This unit displays deformed bedding and occasional debris flows, which indicate slumping of carbonate mud that under went rapid deposition (Furley, 2001; Volk et al., 2001). The Upper Mud Member is the upper-most unit within the Popovich Formation and is composed of laminated limey to dolomitic mudstone. This is the only unit within the Popovich Formation that completely overlies the adjacent Bootstrap limestone indicating the drowning of the shelf environment (Furley, 2001; Volk et al., 2001).

The boundary between the Popovich Formation and the overlying Rodeo Creek Unit is an unconformity representing a depositional hiatus of approximately 6 million years. The Upper Devonian Rodeo Creek Unit is composed of argillite with interbedded limey to dolomitic siltstone, fine-grained sandstone, and minor limestone. This sequence of

rocks is variably calcareous to dolomitic and was deposited in an anoxic environment (Furley, 2001; Volk et al., 2001).

Breccia Formation

Breccias are abundant across the deposit and include multiple types, which formed as the result of a variety of geologic processes. Breccia types observed at Betze-Post include fault breccias, hydrothermal/collapse breccias, sedimentary breccias, debris flow breccias, tectonic breccias, and fault breccias (K. Thompsen, personal communication, 2002). The presence of these breccias across Betze-Post is important to Carlin-type mineralization because they provide the ground preparation required for gold mineralization. Breccias comprise zones of high porosity and permeability needed for ore fluids to migrate and deposit gold. A strong correlation between brecciation, elevated Au, and elevated silicification is consistently present throughout the sampled drill holes at Betze-Post. Breccia lithologies are commonly present within the Wispy unit as well as along the contact between the Popovich and Roberts Mountains Formations. These brecciated zones exhibit abundant silica and the highest grade Au zones sampled during this study.

CHAPTER 4

METHODOLOGY

Sample collecting from the Betze-Post system was accomplished during an eight-week summer field season. Samples were collected from drill core along transects through mineralized zones. Open-pit exposures were mapped and additional sample transects were collected. To learn about ore fluid flux through the Betze-Post system, samples were collected from the North Betze, Betze, Screamer, North Post, and Deep Post ore zones. To reduce variance, sampling was focused within the Wispy member located at the base of the Popovich Formation. Sampling focused on drill core and mine exposures containing quartz associated with gold mineralization. Sample transects extended away from ore zones into low-grade rock to aid in identifying alteration features associated with gold deposition. To identify possible variations in composition, texture, and fluid inclusion properties with depth, samples were collected from various elevations within the system. Samples were also collected from areas near Eocene dikes to test for a magmatic contribution to ore fluid evolution. Fifteen drill holes, spanning all five ore zones, were sampled, while an additional 20 samples were collected from the Betze-Post pit (Figure 6). The geologic context of the samples was documented through examination of geologic cross sections intersected by selected drill holes, logging of drill core, describing selected sections of core, correlating drill core to three-dimensional

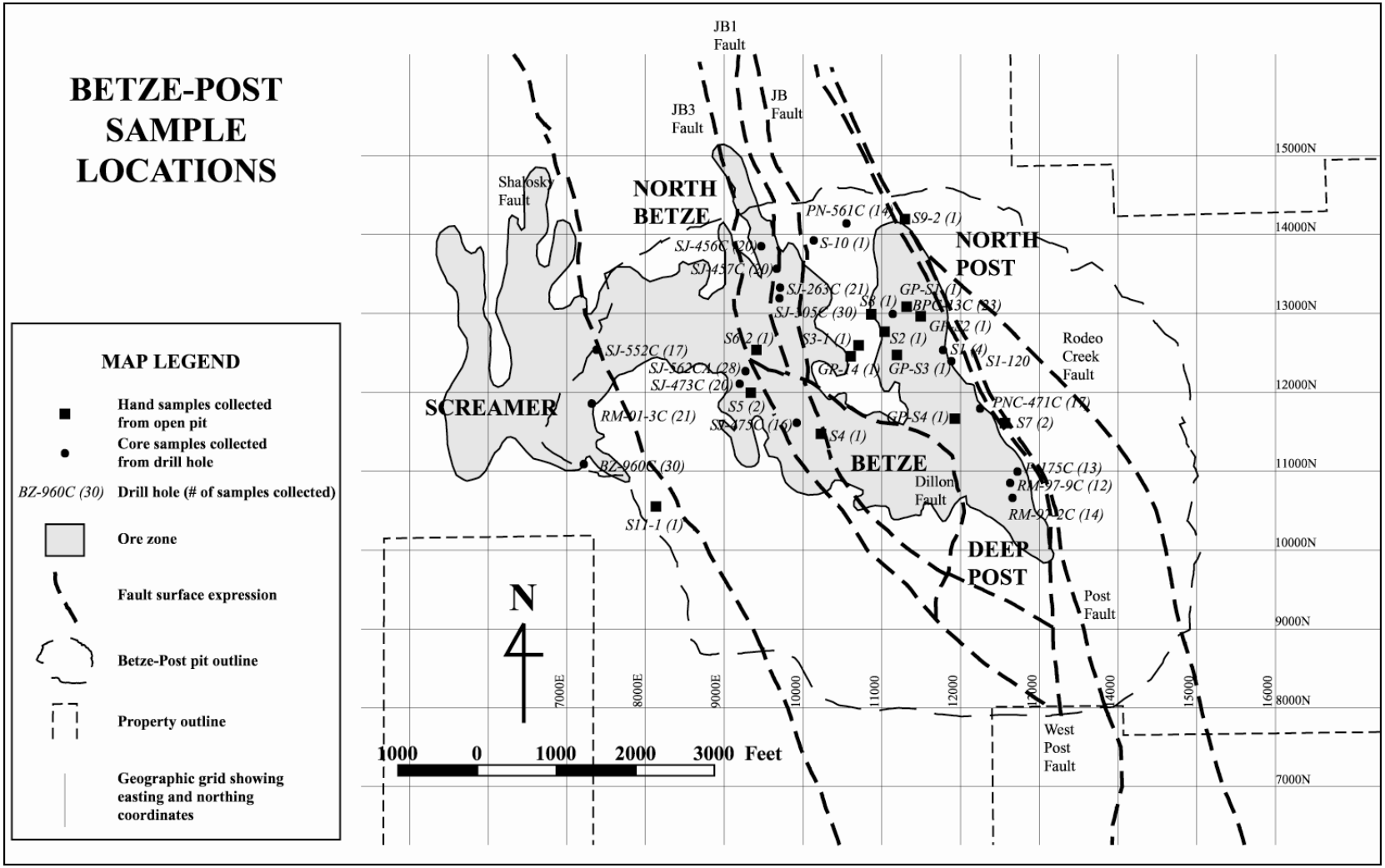

Figure 6. Locations of sampled drill holes (filled circles), pit samples (filled squares), and major structures that cross-cut the Betze-Post deposit. A total of 322 core and hand samples were collected from the Betze-Post deposit.

geologic models, geologic mapping, and documenting petrographic observations made on thin sections.

Drill holes were selected based on alteration patterns and gold grade. Transects trending from low grade to high grade and back to low grade with increasing depth were selected. Approximately 331 core and hand samples from Betze-Post were collected and 70 doubly polished thick sections were prepared from these samples.

Petrography

Petrographic analysis of samples was conducted by both transmitted and reflected light microscopy. The primary goals of petrography were to identify the mineralogy of each sample, identify textural relationships between different minerals in each sample, and to identify and describe different types of silicification. These led to identifying the relative timing relationships between different minerals, as well as different silicification types, within each sample. Petrographic observations contributed to a preliminary mineral paragenesis for each sample that were compiled to produce a comprehensive mineral paragenesis for the Betze-Post deposit. Petrography and paragenetic relationships were critical for selecting types of quartz for further microanalysis.

Microprobe Analysis

A JEOL-5600 Scanning Electron Microscope provided semi-quantitative chemical compositions, and aided in identifying minerals within samples. Energy dispersive spectrometry (EDS) analysis provided the chemical compositions of minerals and

contributed to the classification of different mineral generations within samples from Betze-Post.

A JEOL-8900 Electron Probe Microanalyzer provided quantitative chemical analyses and images. Wavelength dispersive spectrometry (WDS) analyses quantified the trace element chemistry of quartz. Count times averaged around 30 seconds for major elements while count times for trace elements were increased to lower detection limits. Detection limits for these analyses averaged 0.01 wt% (100 ppm) for all elements.

Qualitative imaging methods included backscatter electron imaging (BEI), x-ray mapping, and cathodoluminescence (CL), and aided in distinguishing discrete generations of quartz within each sample. An Oxford/Gatan Mini-CL Cathodoluminescence Detector mounted inside the electron microprobe column was used for CL analysis of different quartz types. CL provides "real time" images, or automated images in tandem with x-ray mapping to characterize the area of interest. The CL mount provided a gray-scale image, thus different degrees of luminosity are identified based on relative brightness.

Backscatter electron imaging (BEI) was used to identify compositionally distinct zones, particularly within a single mineral. BEI provides images that display zones based on atomic number, illustrating differences in composition by different intensities on a gray-scale image. X-ray element mapping provided element maps illustrating relative abundances of selected elements, which could be correlated with zones with differing luminosities. Analyses allowed various stages of quartz to be correlated from sample to sample and the relative timing of various generations of quartz was constrained.

Stable Isotope Analysis

In-situ oxygen isotope analyses were conducted by secondary ion mass spectrometry (SIMS) at Arizona State University. A Cameca IMS-3f ion microprobe was used to collect $\delta^{18}O$ values for various generations of quartz. The quartz standard, Arkansas quartz, was analyzed frequently to ensure precision in the collected $\delta^{18}O$ values. A potassium beam with an accelerating potential of 15 Kv and a primary current between 1-2 nanoamps (nA) was used at extreme energy conditions to gain ^{16}O counts of roughly 300,000, which were measured on an electron multiplier. The analysis spot size induced by the beam was measured at 15 μm by petrography. Isotope values are reported in delta notation, where $\delta^{18}O_{sample} = [(^{18}O/^{16}O)_{sample} / (^{18}O/^{16}O)_{standard} - 1] * 10^3$ in per mil relative to Vienna standard mean ocean water (VSMOW).

Hydrogen isotope analyses of fluids released from quartz samples and representing inclusion fluids were conducted using a helium carrier continuous flow thermochemical conversion gas chromatograph coupled to a Delta mass spectrometer at the USGS in Denver. Samples were selected based on grain size and luminescence. Samples of ~2.0 grams of discrete quartz generations were hand picked from hand samples from which sections were prepared. Ore stage jasperoid samples were picked clean of any drusy quartz while drusy quartz samples were selected by collecting individual crystals. Hydrogen isotope analyses were conducted on a bulk fluid released from fluid inclusions in quartz. The hydrogen analyzed is representative of all the hydrogen sites in the mineral: fluid inclusion water (± other gases such as CH_4, H_2S, etc), OH in the quartz, H-bearing organic matter, or OH-bearing clay minerals. The δD values obtained are on H_2 produced by dropping the samples into a 1400°C reactor containing glassy carbon, which

converted any H_2O, OH, CH_4, H_2, organic matter, or glue present in the samples to CO and H_2 in the reactor.

Conventional bulk $\delta^{18}O$ analysis of the quartz host was paired with each δD analysis. $\delta^{18}O$ values of ~2.0 gram quartz samples were determined using the bromine pentafluoride technique (Clayton and Mayeda, 1963). Surface water was removed from 25-500 mg samples of drusy quartz and jasperoid by baking them in a vacuum overnight at 125°C. $^{18}O/ ^{16}O$ ratios were quantified relative to standard mean ocean water (SMOW).

Fluid Inclusion Analysis

Fluid inclusion populations within quartz were identified and related to various paragenetic stages of quartz. Fluid inclusions were examined for presence in assemblages, presence along growth zones, size, liquid to vapor ratios, presence of daughter crystals, occurrence as arrays along secondary fractures, and occurrence within different quartz types.

Microthermometry was conducted on a computer-automated Linkam heating and freezing fluid inclusion stage. The stage was calibrated by analyzing synthetic fluid inclusions with known homogenization and ice melting temperatures. Analyses of ice melting temperatures were conducted with a measured error of ±0.1°C. Homogenization temperatures were determined by heating inclusions in 10 degree increments until the vapor phase homogenized and did not return with minimal cooling. Ice melting temperatures were determined by monitoring the contraction and expansion of the vapor bubble within individual inclusions during cooling and heating runs. Ice melting

temperatures where determined where cooling no longer caused contraction of vapor bubble. Salinities were calculated as weight percent NaCl equivalent and are based on equations derived by Hall et al. (1988).

CHAPTER 5

PARAGENETIC ANALYSES

Petrographic Analysis

Petrographic analysis of samples collected from the Betze-Post system identified numerous types of quartz, opaque minerals associated with different mineralization events (i.e. pyrite and marcasite), and multiple accessory minerals (i.e. calcite and barite). Observed textural relationships between these three mineral groups indicated a preliminary paragenesis that was further refined by integrating additional microanalytical techniques.

From the 331 total core and pit samples collected from Betze-Post, 61 samples were selected for doubly polished thick section preparation. Thick sections where prepared at thicknesses ranging between 70 and 100 μm. These samples were selected based on high internal hardness, strong concentrations of coarse drusy quartz along vugs and quartz veins, and high Au concentrations. Transmitted and reflected light microscopy was conducted on three sections from three Deep Post drill holes, eight sections from three North Post drill holes, nine sections from three Betze drill holes, twenty sections from four North Betze drill holes, ten sections from three Screamer drill holes, and eleven sections from the twenty-two pit samples collected from the Betze-Post pit.

Discrete types of quartz were identified based on precipitation mode, grain size, grain morphology, setting, habit, and unique texture. Table 1 lists descriptions of the various types of quartz in terms of precipitation mode, distinctive physical properties, significant textural relationships with other types of quartz, spatial relationships with various pyrite generations, and luminescence. Transmitted light and reflected light microscopy studies identified three types of drusy quartz, two types of quartz veins, and four types of jasperoid quartz.

The first order separation of quartz types was based on mode of precipitation, either by open-space deposition or replacement, which are distinguishable by textures. Replacement silicification includes jasperoid precipitation (Table 1), which involved the replacement of carbonate material within the host rock by silica.

Open-space precipitation involves the deposition of silica within available open space within the host rock. Two habits of open-space quartz include drusy quartz along fractures and vugs within the host rock and the filling of fractures by quartz veins. Petrography has identified multiple types of drusy quartz (Table 1) based on grain size, grain morphology, geologic setting, and unique petrographic properties. Quartz veins constitute a second type of open-space filling quartz identified within Betze-Post samples and are referred to as Q5 and Q6 quartz (Table 1).

Documented accessory minerals include calcite, barite, dolomite, and realgar and were described based on observations made using transmitted and reflected light microscopy. All of these minerals, except for dolomite, were deposited by open-space processes and fill fractures and vugs within respective host rocks. Dolomite grains are

Table 1. Classification of quartz types based on petrographic observations and cathodoluminescence imaging

Quartz habit	Sub-type	Distinctive Properties	Significant textural relationships	Luminescence
Intra-vug Drusy Quartz (Q1)	Q1a	100µm - 800µm long euhedral quartz crystals that interlock with one another; crystals show quartz terminations; crystals are elongated; crystals coarsen as quartz gets younger into the center of the vug; this type has a higher abundance of calcite inclusions along the boundary with jasperoid zones	overgrows Q10a,Q10b, Q10c, and Q10d; overgrown by Q1b and Q1c; Q6 quartz veins grow into this type; spatially associated with anhedral pyrite grains that have visible pits. Pyrite grains average 20µm in diameter and are mostly concentrated along the Q1/Q10 interface; pyrite grains display ore-stage textures (Henkelman et al., 2003; Henkelman, 2004)	CL-Dark
	Q1b	euhedral quartz crystals that range from 200µm - 800µm in diameter; grains coarsen as quartz gets younger; crystals are equant; crystals show distinct quartz terminations and are interlocked	overgrows Q1a drusy quartz; overgrown by Q1c drusy quartz; spatially adjacent to Q5 and Q6 quartz veins; there is no spatial association with pyrite	CL-Bright
	Q1c	200µm - 800µm sub- to euhedral quartz crystals that coarsen as quartz gets younger; grain morphology is not as elongated; crystals are interlocking and display distinct termination surfaces	overgrows Q1a and Q1b drusy quartz types; Q5 and Q6 quartz veins grow into this type of drusy quartz; there is no spatial association with pyrite	CL-Multiple
Intra-clast Drusy Quartz (Q2)	Q2a	20µm to ~200µm in diameter; coarsen as the crystals gets younger; similar to Q1a in that the crystals appear to be elongated versus other Q2 quartz types; crystals host a high abundance of calcite inclusions along the boundary with jasperoid zones	overgrows Q10 quartz types; localized within the jasperoid breccia clasts; overgrown by Q2c intraclast drusy quartz; the only associated pyrite is pyrite grains that are hosted within the jasperoid clasts and are localized along the quartz/clast boundary; in some cases the pyrite displays ore-stage textures	CL-Dark

Table 1. Classification of quartz types based on petrographic observations and cathodoluminescence imaging

Quartz habit	Sub-type	Distinctive Properties	Significant textural relationships	Luminescence
Intra-clast Drusy Quartz (Q2)	Q2c	this quartz ranges from 200µm to 600µm in diameter; crystals coarsen as the crystals get younger; crystals are sub- to euhedral and are not as elongated as Q2a quartz	overgrows Q2a intraclast drusy quartz; localized as the innermost drusy quartz layers within all of the intraclast drusy quartz zones that are localized within Q10 zones; pyrite is localized within the adjacent jasperoid clasts; this quartz type generally does not host pyrite	CL-Multiple
Intra-matrix Drusy Quartz (Q3)	Q3a	this type of quartz represent intra-matrix zones of coarse quartz that ranges from 100µm to 400µm; this quartz coarsens as the quartz gets younger; interlocking crystals; the crystals have calcite inclusion with the abundance of inclusion increasing in the grains along the outermost margin of the quartz at the jasperoid/quartz boundary	occurs within Q10a quartz; localized within the matrix zones of the brecciated samples; pyrite is localized within adjacent jasperoid clasts	CL-dark
	Q3b	this type of quartz represent intra-matrix zones of coarse quartz that ranges from 100µm to 400µm; this quartz coarsens as the quartz gets younger; interlocking crystals; the crystals have calcite inclusion with the abundance of inclusion increasing in the grains along the outermost margin of the quartz at the jasperoid/quartz boundary	occurs within Q10a quartz; localized within the matrix zones of the brecciated samples; no apparent spatial association with Au-bearing pyrite grains	CL-bright
Intra-clast vein quartz	Q5	fine grained quartz with an average grain size of less than 10µm long; This quartz occupies veins that completely crosscut the clast but do not cut across into matrix zones and other clasts	veins crosscut Q10 quartz types, however they die out within the clasts; spatial correlation with anhedral pyrite that have less than 5um diameters; pyrite has pits and is isotropic; these pyrite grains display ore stage textures	CL-Dark

Table 1. Classification of quartz types based on petrographic observations and cathodoluminescence imaging

Quartz habit	Sub-type	Distinctive Properties	Significant textural relationships	Luminescence
Intra-matrix vein quartz	Q6	quartz veins that completely crosscut breccia clasts and show offset of the clasts; these veins also are present outside of breccia clasts and can show offset within matrix zones; crystals are equant and range from 20µm to 600µm in diameter	veins are finer grained than Q2 and appear to be an extension from Q1a, Q1b, and Q1c drusy quartz zones; veins intersect one another; veins crosscut Q10a, Q10b, and Q10c, and Q10d; no spatial correlation with ore stage pyrite grains	CL-Bright
Inherited quartz grains	Q7	quartz grains that display rounded surfaces that do not interlock with other grains; these grains are isolated and cemented within a quartz matrix; grains appear mechanically weathered	found within Q10b quartz zones; no apparent association with pyrite	CL-Dark
Jasperoid quartz	Q10a	very fine-grained quartz (~5µm crystals) that is present within individual breccia clasts; contains very fine calcite inclusions; quartz crystals have an abundance of inherited materials that covers-up the finer grained quartz	has sporadic zones of Q2; has multiple Q5a (fine quartz veins); crosscut by Q6 veins and overgrown by Q1a drusy quartz; host both diagenetic and ore-stage pyrite; host very fine-grained sphalerite and Ti-bearing minerals; ore-stage pyrite display distinct core and rim textures and has a localized concentration along the interface between Q10a, Q1a, Q2a, and Q3a quartz	CL-Dark
	Q10b	very fine-grained quartz (coarser than Q10a) that occurs within matrix zones of brecciated samples; displays a lighter gray color than other types of jasperoid clasts in the sample; distinct calcite inclusions; quartz crystals have an abundance of inherited materials	abundant zones of Q2a and Q2c; Q6 veins offset this type of jasperoid; hosts numerous Q7 quartz grains; host both diagenetic and ore-stage pyrite; host very fine-grained sphalerite and Ti-bearing minerals; ore-stage pyrite displays distinct core and rim textures and has a localized concentration along the interface between Q10b and Q1a quartz types	CL-Dark

Table 1. Classification of quartz types based on petrographic observations and cathodoluminescence imaging

Quartz habit	Sub-type	Distinctive Properties	Significant textural relationships	Luminescence
	Q10c	very fine grained quartz crystals that comprise zones where fossil debris has been replaced with silica; can be associated with very subtle evidence of clay minerals intermixed with quartz crystals; host low amounts of inherited material.	overgrown by Q1 drusy quartz types; pyrite is disseminated within this type of jasperoid quartz; host lowest amounts of pyrite relative to other three jasperoid types.	CL-Dark
	Q10d	very fine grained quartz that comprise non-brecciated samples; represent areas where brecciation did not occur and original undisturbed host rock was replaced with silica	overgrown by several drusy quartz types; pyrite is disseminated within this type of jasperoid quartz; host lowest amounts of pyrite relative to other three jasperoid types; well sorted and possesses the lowest amount of inherited material.	CL-Dark

overgrown by open-space quartz and are linked to the original diagenesis of host formations.

Opaque minerals were described and classified with reflected light microscopy and were distinguished by color, brightness, relief, polish, internal reflectance, and texture. Opaque minerals include pyrite, marcasite, bitumen, and sphalerite. Discrete pyrite types and generations were determined based on size, morphology, polish, and relief. After pyrite types were classified, spatial relationships between pyrite types and quartz types were evaluated to determine the mineral paragenesis. Cathodoluminescence (CL) and backscatter electron (BEI) imaging contributed to identifying the spatial relationships between pyrite and quartz types. LA-ICP-MS analyses aided in identifying different pyrite types and confirmed identification of Au-bearing and trace element-rich ore-stage pyrite.

Quartz Cathodoluminescence

Quartz crystals at Betze-Post display varying degrees of luminescence, which reveals zoning between different generations of quartz. Cathodoluminescence studies illustrate the degree of luminescence in different generations of quartz. CL studies were conducted to further distinguish different generations of quartz identified by petrography, and to provide a more accurate mineral paragenesis. BEI images were collected along with CL images for each area analyzed to spatially correlate mineralogy with luminosity.

Luminescence in quartz can be induced by several processes including 1) the substitution of Si by an element of similar charge and size (i.e. Si^{4+} by Al^{3+}), 2) the presence of a charge compensating cation that fills any possible charge vacancy caused

by the previous mentioned substitution process (i.e. Li, Ca, Na), or 3) H_2O or OH present within the quartz lattice.

Numerous elements, in trace amounts, may be substituted for Si in quartz. Trace elements previously recorded in quartz include H, Li, B, Na, Al, Ge, K, Ca, Ti, Cr, Mn, Cu, Fe, Rb, Pb, and U (Watt et al., 1997). Trace elements in quartz can occur interstitially within the quartz lattice and/or by substitution (Cohen, 1960). Substitution for silicon is limited by its high valence state (+4) and relatively small atomic radius (0.400 Angstroms) (Sprunt, 1981). Hydrogen, associated with defects and substitution of Ti^{4+}, Ge^{4+}, Ti^{3+}, Al^{3+}, or Fe^{3+} for Si^{4+} with charge compensating cations such as H^+, Na^+, K^+, and Li^+, is frequently observed in natural quartz (Sprunt, 1981; Kalceff et al., 2000). Quartz origin plays a major role in the distribution of trace elements into the quartz lattice. Numerous geologic environments can produce quartz with each process regulating the composition and quantities of trace element incorporated into the lattice.

It is important to discuss the role of water in the quartz lattice, because H^+, OH^-, and H_2O are important impurities in quartz. Water in quartz is comprised of crystal-bound water (defect structures, dislocations), water in micro-pores, water in micro-cracks, and water in fluid inclusions (Muller, 2000). The relative abundance of water in the lattice is a function of the formation temperature and the salinity of the fluid from which quartz precipitates (Kerkhof & Simon, 2001). Water within the lattice of quartz can produce a stress-induced mechanism referred to as hydrolytic weakening, which can produce defect structures in the quartz lattice (Muller, 2000). It has been hypothesized that water is incorporated into the crystal lattice by the substitution for Si^{4+} by $4H^+$ (Muller, 2000).

CL imaging was conducted on quartz samples from all five ore zones. CL and BEI images were collected from 56 thick sections covering 15 drill holes and 10 pit samples. Images were collected from 4 samples at North Post, 3 samples at Deep Post, 9 samples at Betze, 20 samples at North Betze, 9 samples at Screamer, and 11 samples collected from the Betze-Post pit.

CL studies consistently identified three CL-luminosities (CL-dark, CL-bright, and CL-multiple) (Figure 7a). CL-dark luminescing zones appear black and CL-bright luminescing zones appear bright white. CL-multiple luminescing zones include alternating euhedral black, white, and gray luminescing zones within individual quartz crystals on CL images.

Varying intensities of CL-bright and CL-multiple luminosities are present across the ore zones within the Betze-Post deposit. Post-ore-stage quartz crystals from Betze and North Betze exhibit the strongest CL-bright and CL-multiple luminescence of any quartz crystals analyzed. Furthermore, post-ore-stage quartz samples from Screamer exhibit moderate intensity CL-bright and CL-multiple luminescence. Post-ore-stage quartz samples from North Post exhibit weak CL-bright and CL-multiple luminescence. Finally, post-ore-stage quartz was not identified at Deep Post; thus, no CL-bright or CL-multiple luminescing quartz was identified from this ore zone.

Using these three basic CL-luminosities, several CL-stratigraphies that are consistent with a single paragenesis were identified. Each of these stratigraphies is classified based on observed overgrowth and crosscutting relationships between different quartz generations. It should be noted that each CL-stratigraphy identified includes multiple generations of quartz that are only visible with the help of CL. Quartz generations

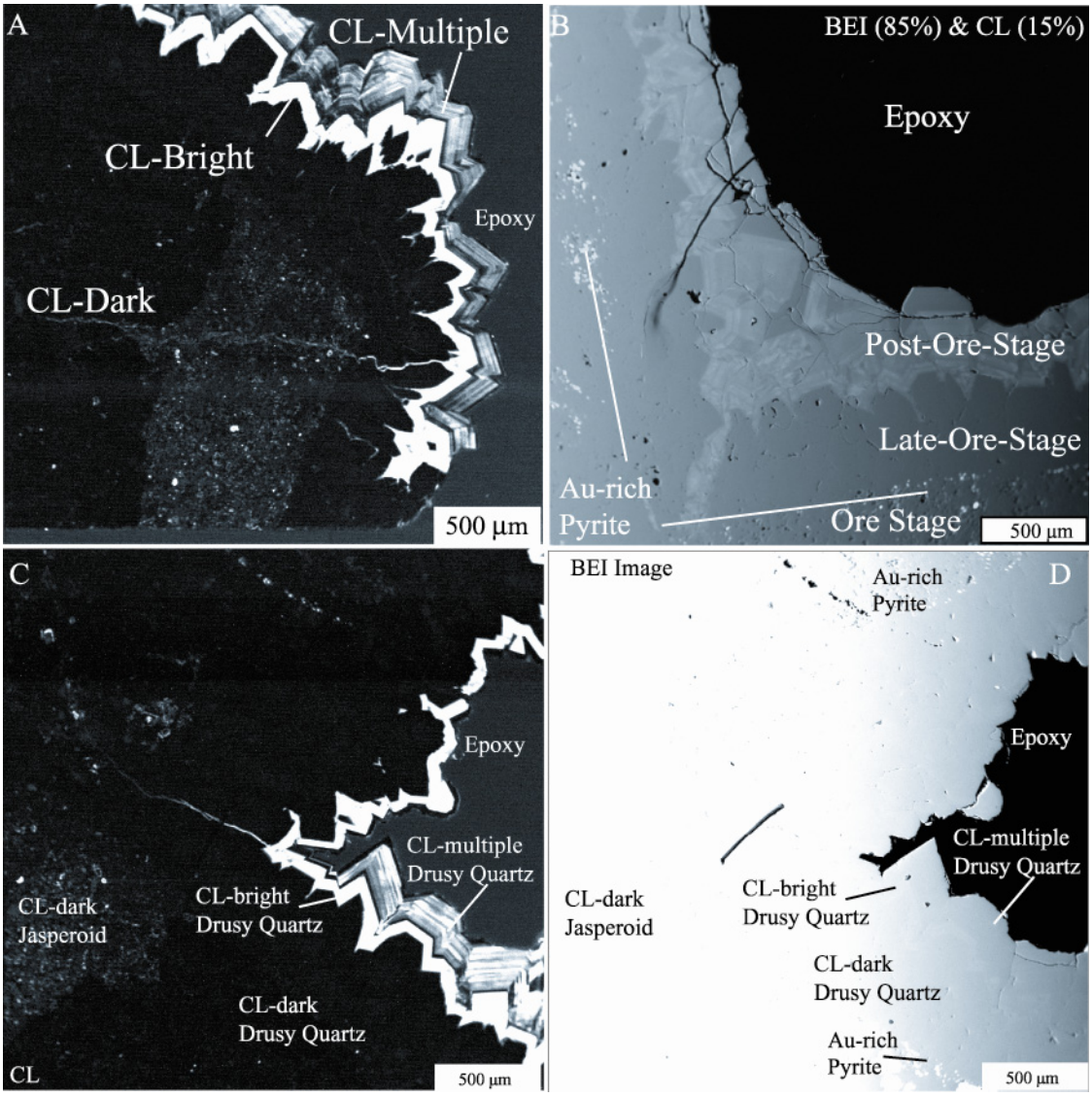

Figure 7. Three distinct luminosities identified by CL-analysis. A) The three CL-luminosities include CL-dark, CL-bright, and CL-multiple. B) Combined CL and backscatter electron image (BEI) illustrating spatial correlation between CL-dark ore stage jasperoid and Au-rich pyrite grains. Note: Au-rich pyrite is absent along the interface between CL-dark and CL-multiple/CL-bright drusy quartz. C) Comprehensive quartz paragenesis illustrating the separate quartz generations that have been identified at Betze-Post. D) BEI image of same region as figure C, and illustrating spatial relationships between quartz and pyrite in samples from Betze-Post.

identified at Betze-Post include four types of CL-dark jasperoid, three types of CL-dark drusy quartz, a single type of CL-dark vein quartz, two types of CL-bright drusy quartz, a single type of CL-bright vein quartz, and a single type of CL-multiple drusy quartz (Figures 7c, 7d) (Table 1). CL analysis was critical in identifying all ore stage quartz generations at Betze-Post. Spatial relationships between gold-bearing pyrite and distinct quartz generations were identified by comparing CL and BEI images and led to ore stage quartz identification (Figure 7b).

CL and BEI images show that pyrite grains, displaying gold-bearing textures identified by Henkelman et al. (2003) and Henkelman (2004) occur as both disseminated grains within CL-dark jasperoid quartz and as localized populations of grains along the interface between CL-dark jasperoid and CL-dark drusy quartz. Based on these observations it is concluded that CL-dark jasperoid represents a main-ore-stage quartz generation that is synchronous with the Carlin mineralization event, while CL-dark drusy quartz represents late-ore-stage silicification that formed after the main Carlin mineralization event. Gold-bearing pyrite is consistently absent along the interfaces between CL-dark drusy quartz and either CL-bright drusy quartz or CL-multiple drusy quartz. These textures demonstrate that CL-bright and CL-multiple drusy formed during post-ore-stage silicification events that post-date the Carlin mineralization event.

CL-dark quartz veins overgrow gold-bearing pyrite grains at the base of their crystals, similar to CL-dark drusy quartz, and are classified as late-ore-stage. CL-bright quartz veins crosscut CL-dark jasperoid clasts completely and transect adjacent clasts indicating they are younger than CL-dark ore-quartz generations. Furthermore, these quartz veins do not correlate spatially with ore stage pyrite grains.

CL analyses proved to be crucial in constraining the relative timing relationships between quartz, accessory minerals (i.e. calcite, barite, realgar, and dolomite), and opaque minerals (i.e. pyrite, marcasite, bitumen, and sphalerite). CL studies also constrained distinct generations of quartz, which allowed other microanalytical techniques to be conducted on paragenetically constrained quartz generations (i.e. microthermometry and SIMS $\delta^{18}O$ analyses).

Betze-Post Mineral Paragenesis

The comprehensive mineral paragenesis identified for the Betze-Post deposit is divided into four stages including; 1) pre-ore, 2) main-ore, 3) late-ore, and 4) post-ore (Figure 8). It should be noted that pre-ore and post-ore stages consist of multiple events that are unrelated to the Carlin-type mineralization event. Mineral occurrences observed at Betze-Post include quartz, pyrite, marcasite, calcite, barite, realgar, orpiment, sphalerite, dolomite, and bitumen. Silicification at Betze-Post is abundant and related to numerous hydrothermal events; thus, it was critical to identify the temporal relationships between different quartz types.

Pre-Ore Stage

Observed pre-ore-stage minerals are defined as precipitating prior to the Carlin-type mineralization event. This mineral assemblage includes quartz, pyrite, calcite, dolomite, bitumen, and sphalerite (Figure 8).

The first identified silicification event is the precipitation of Q7 inherited quartz grains (Figure 9). Q7 quartz grains display rounded edges, appear rotated, and range between 500 μm and 1500 μm. Q7 quartz grains display CL-dark luminescence and host

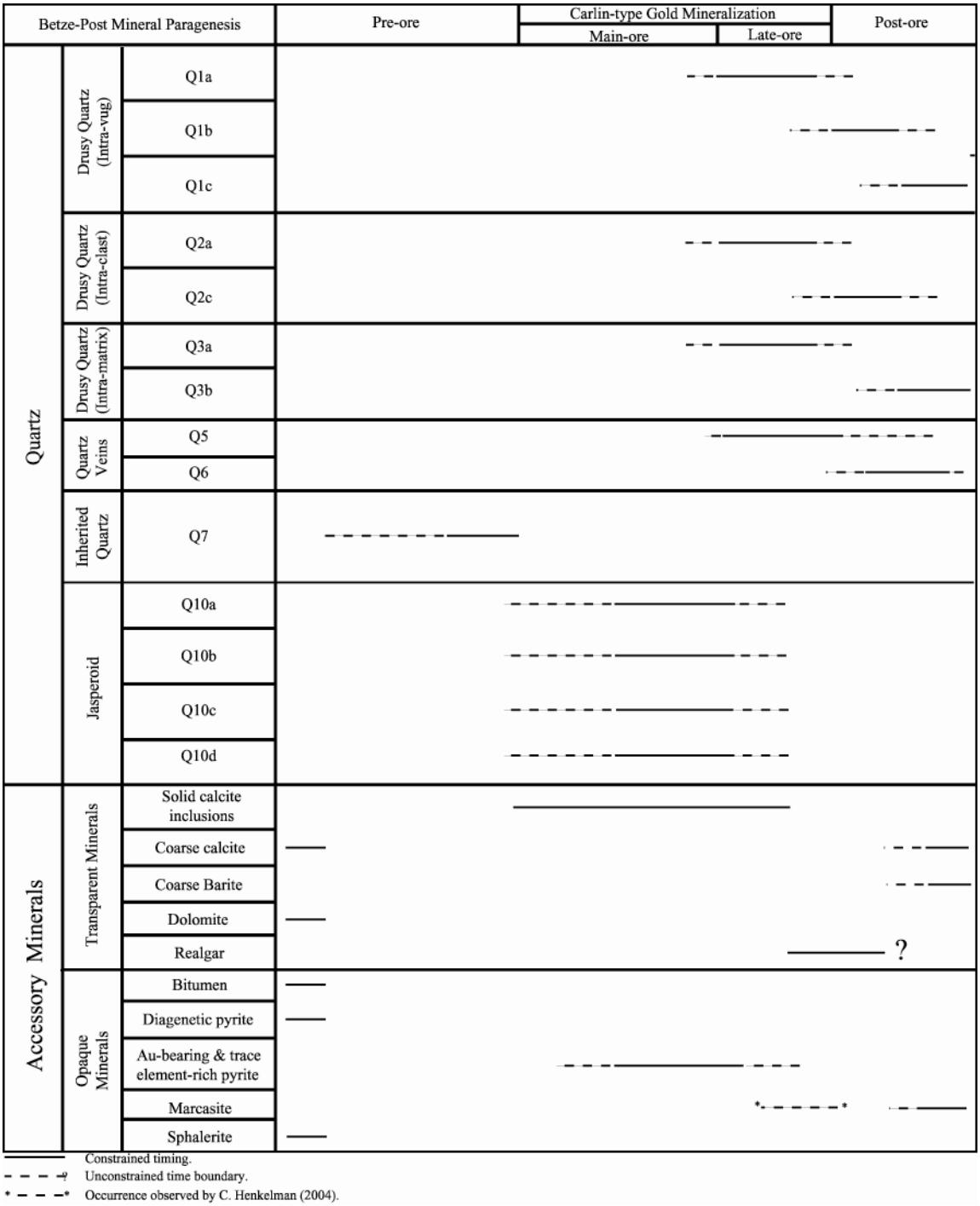

Figure 8. Mineral paragenesis for the Betze-Post Carlin-type gold system.

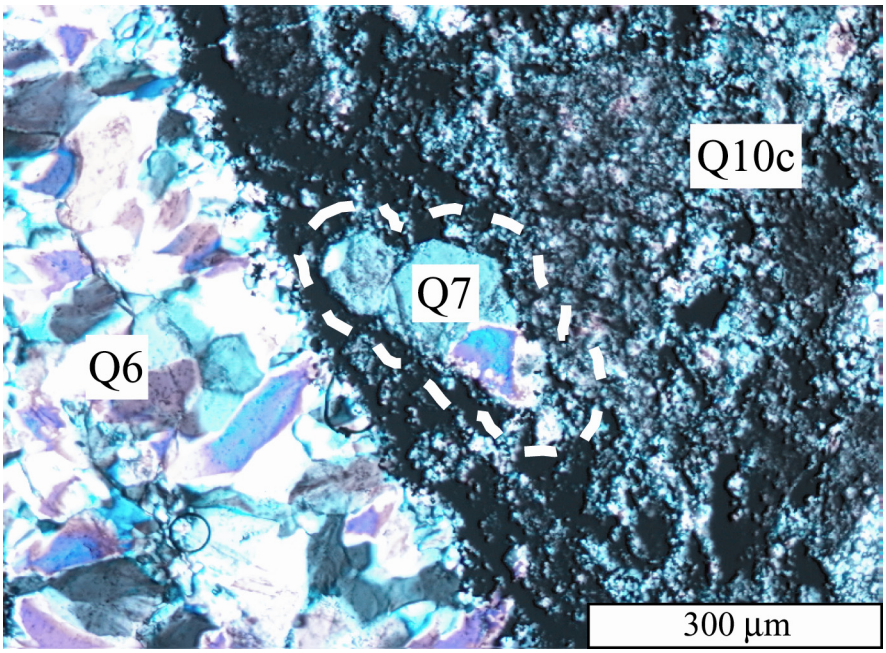

Figure 9. Photomicrograph of Q7 quartz grains in North Betze sample SJ-305C-1041.5 under plane-polarized transmitted light. Q7 quartz displays rounded quartz crystals that appear rotated and re-cemented within younger quartz types.

secondary two-phase fluid inclusion assemblages in fractures that crosscut individual grains. Q7 quartz grains are disseminated within Q10c ore stage silicified debris flow jasperoid zones that comprise the matrix of brecciated samples.

Multiple types of pre-ore pyrite generations are observed. Pre-ore pyrite types are distinguished by their physical properties including morphology, size, polish, relief, and habit. Pre-ore pyrite types exhibit multiple morphologies including grains that range between euhedral (Figure 10), anhedral, and angular. Furthermore, framboidal grains are observed and display a spherical form. Pre-ore pyrite grains typically show a wide range in grain size with grains measured between 10 μm and 600 μm. Pre-ore pyrite grains display varying degrees of polish including a poor polish in some cases, while other types display a very good polish. Furthermore, a pitted appearance has been observed in some types. A distinguishing property of pre-ore-pyrite grains is relief. Pre-ore pyrite grains display high relief throughout the various types. Finally, pre-ore pyrite grains are localized within numerous geologic settings including clusters of multiple grains, as grains disseminated through the host rock, and along bedding planes within the host rock. These pyrite generations are further characterized by Henkelman (2004).

Sphalerite has been identified in samples from Betze-Post and exhibits textures that suggest a pre-ore origin. Sphalerite grains are subhedral to euhedral, coarse, well polished, show high relief, and range between 10 μm and 70 μm (Figure 11). Sphalerite grains are localized along bedding planes and as disseminated grains within jasperoid zones.

Bitumen grains occur in samples from the North Betze ore zone (Figure 12). Bitumen grains are opaque under plane polarized transmitted light and are light brown

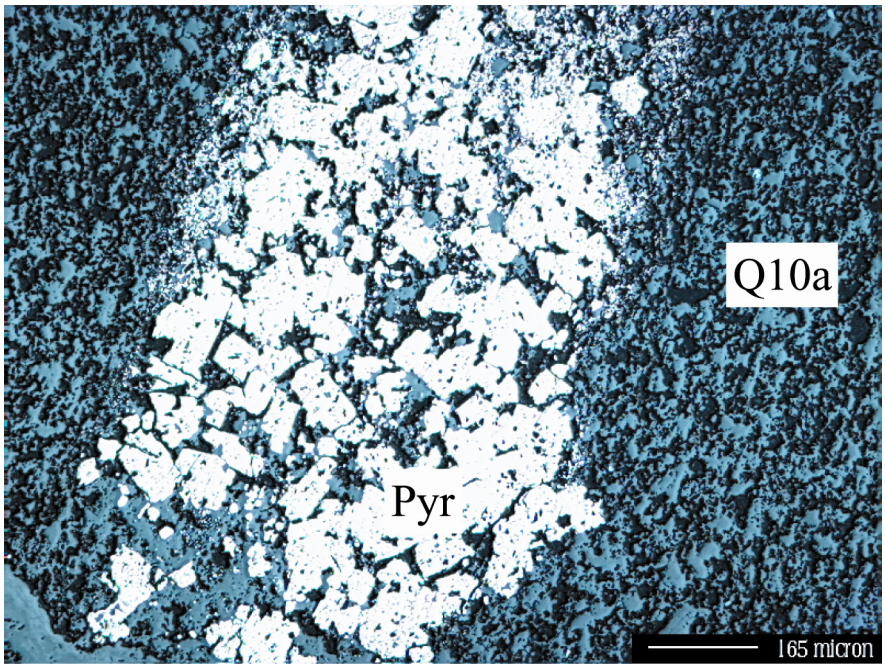

Figure 10. Pre-ore diagenetic pyrite localized along bedding planes within respective host rock in North Betze sample SJ-457C-1052.8. Pre-ore pyrite grains are generally coarse, have a good polish, and are euhedral. Image taken under plane polarized reflected light.

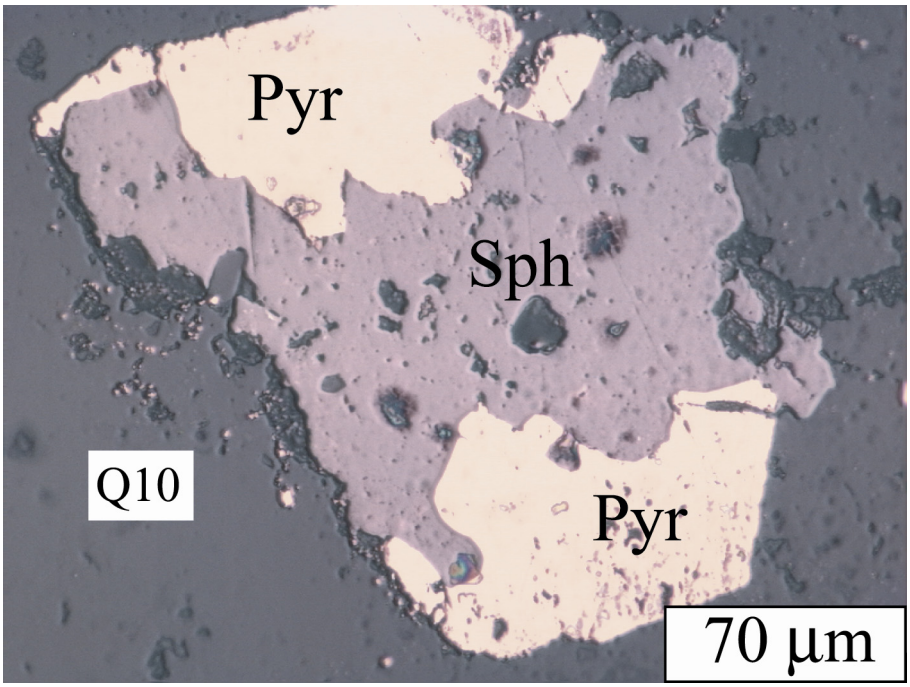

Figure 11. Diagenetic sphalerite localized within jasperoid zones in North Betze sample SJ-305C-1041.2. Sphalerite is grey in color and is euhedral to subhedral (Pyr = Pyrite; Sph = Sphalerite). Image taken under plane polarized reflected light.

under plane polarized reflected light. Bitumen grains range from 10 μm to 1500 μm, are rounded, poorly sorted, disseminated throughout jasperoid zones, and localized along fractures that crosscut jasperoid zones.

Coarse calcite forms veins within fractures in unaltered to minimally altered samples (Figure 13). Calcite crystals range between 300 μm and 2000 μm and display perfect cleavage and, in some grains, display distinct calcite twinning.

Dolomite grains are very coarse and display dull gray and brown colors under plain polarized transmitted light. Dolomite grains range from 300 μm to 600 μm in diameter and are localized within brecciated zones. Dolomite grains occur as clasts within brecciated samples and are overgrown by CL-dark late-ore-stage drusy quartz (Figure 14). Dolomite grains are primarily present at North Betze.

Discussion of Pre-Ore-Stage Mineralogy

The pre-ore stage mineral assemblage consists of several minerals that precipitated during diagenesis, and that would be altered later during the Carlin-type mineralization event. The majority of minerals in the pre-ore assemblage constitute "debris" inherited by jasperoid during replacement of carbonate by silica.

Subhedral Q7 quartz grains, primarily present at North Betze and Screamer, display rounded textures suggesting these grains underwent some degree of transportation before their final cementation. Q7 quartz grains exhibit textures that could reflect either open-space deposition or deposition by replacement. Silicification could have been either associated with diagenesis or pre-Eocene magmatism. These grains share the same CL-dark luminescence as ore stage quartz generations; however, their rounded texture supports a pre-ore age of formation. Furthermore, these grains are disseminated within

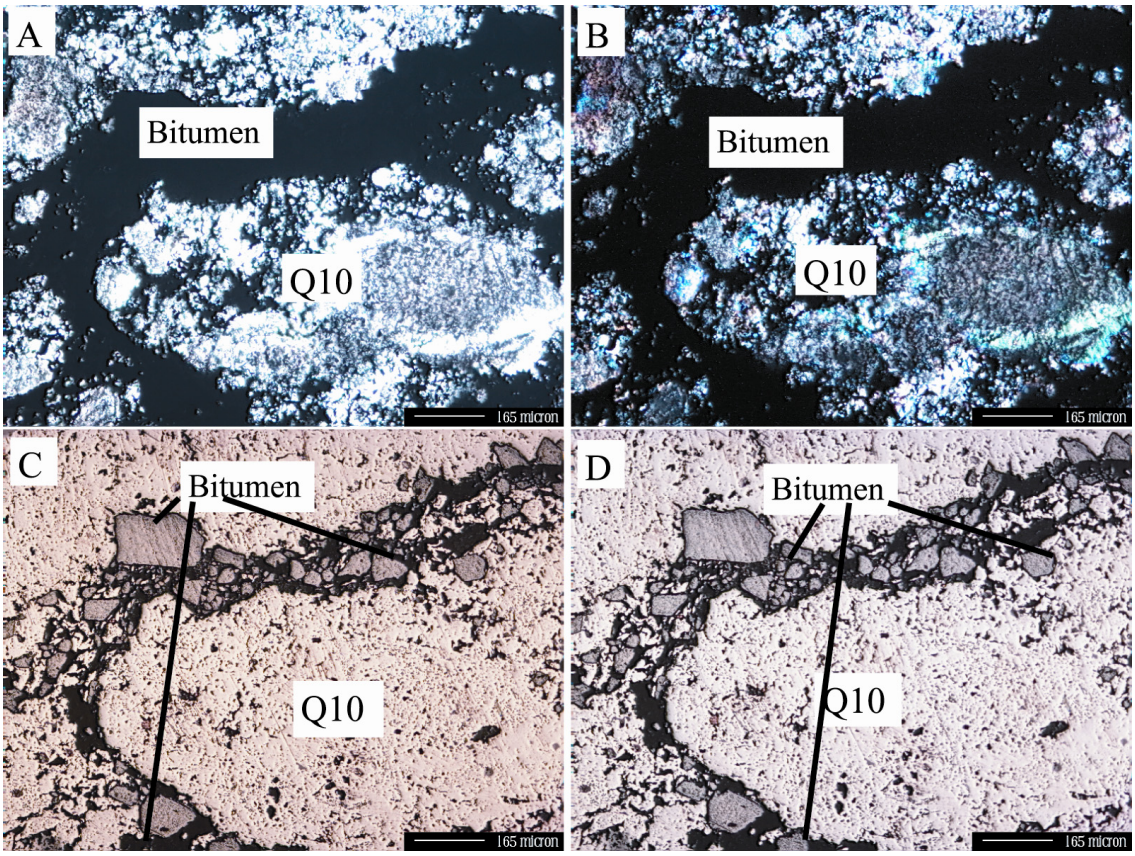

Figure 12. Photomicrographs of pre-ore-stage bitumen in North Betze sample SJ-305C-1052.8. Bitumen is coarse-grained and occurs as disseminated grains throughout jasperoid zones and as grains localized along fractures that cross-cut jasperoid zones. A: Plane polarized transmitted light; B: Crossed-polarized transmitted light; C: Plane polarized reflected light; D: Crossed-polarized reflected light.

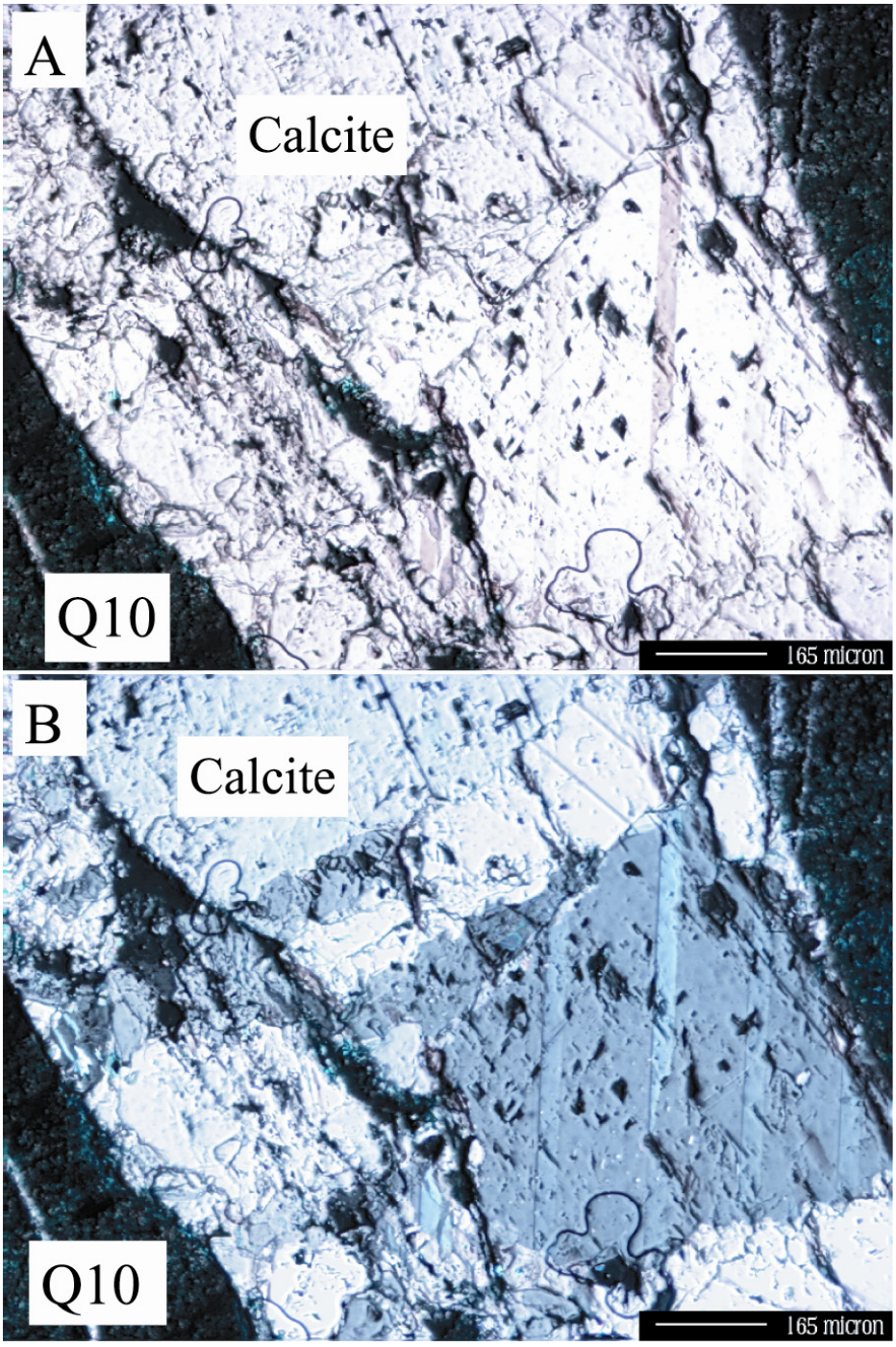

Figure 13. Photomicrographs of pre-ore-stage calcite veins from pit sample S-7 located along the Post Fault. Calcite veins consist of coarse calcite grains and occur within minimally altered to unaltered host rocks. A) Calcite vein under plane polarized transmitted light. B) Calcite vein under crossed-polarized transmitted light.

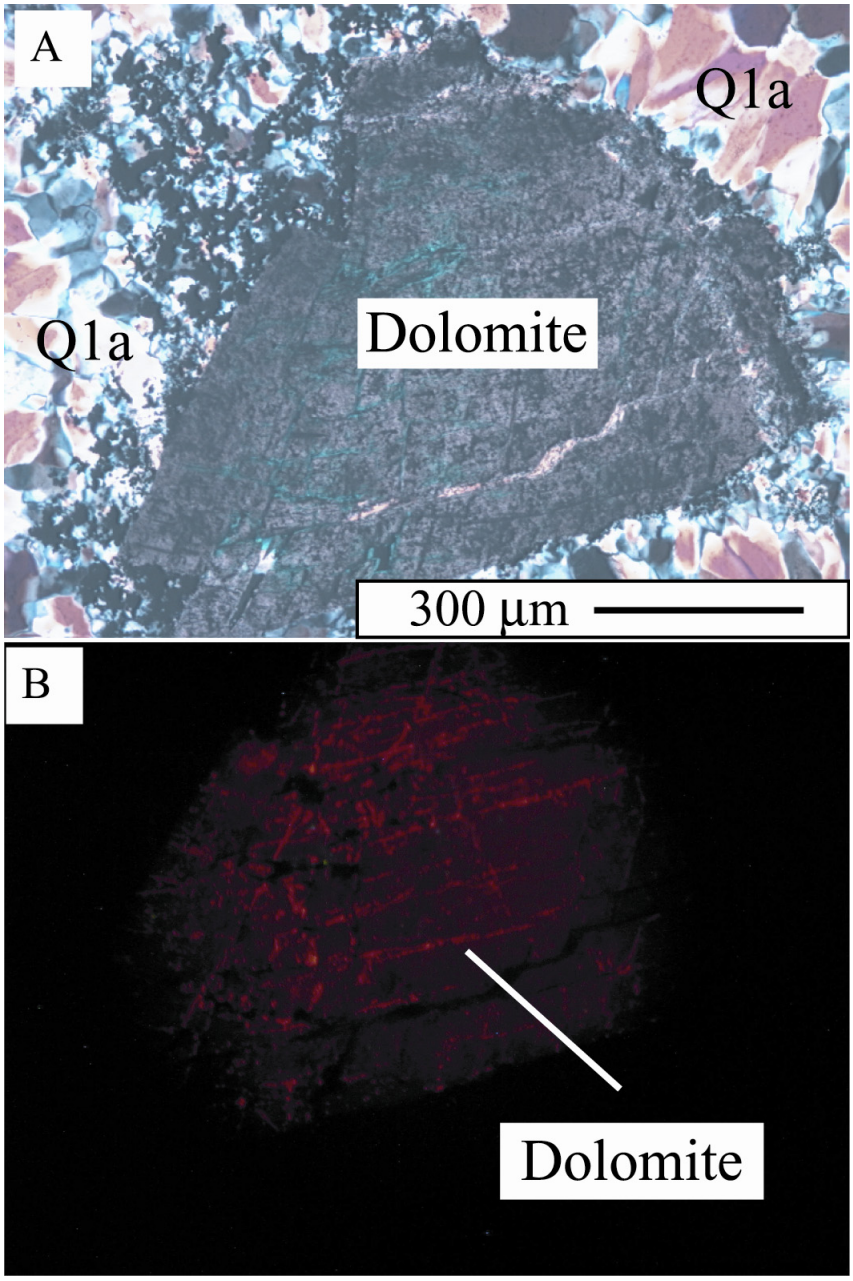

Figure 14. Pre-ore-stage dolomite from North Betze sample SJ-263C-1041.5. A) Photomicrograph of dolomite grains under plane polarized transmitted light. Dolomite grains are overgrown by Q1a drusy quartz crystals. B) Color cathodoluminescence image of dolomite. Grains exhibit distinct red luminescence.

ore stage jasperoid zones, further supporting the interpretation that their original precipitation occurred prior to the Carlin event. However, it is uncertain as to how early these quartz grains were transported and deposited within their debris flow host.

Petrographic characteristics of pre-ore pyrite types suggest that their precipitation occurred very early in the paragenesis. The presence of these pyrite grains along bedding plains suggests that they precipitated during the diagenesis of the original host rock. Furthermore, these pyrite types are present in minimally unaltered to unaltered rocks and clasts indicating a very weak spatial correlation with ore stage alteration and gold mineralization.

Several textures observed between sphalerite, quartz, and pyrite support sphalerite as a pre-Carlin mineral generation. These textures include sphalerite grains along bedding planes, coarse grain size, and textural similarities with pre-ore pyrite grains.

Textures described between bitumen and CL-dark jasperoid types suggest that bitumen grains were remobilized and likely pre-date Carlin-type mineralization at Betze-Post. Previous work by Emsbo (1999) at the Meikle deposit relates bitumen to a hydrocarbon event that pre-dates Carlin-type mineralization.

Coarse calcite grains identified within veins in minimally altered to unaltered zones represent carbonate precipitation coeval with diagenesis of the original host rock. These calcite veins are interpreted to be associated with diagenesis of the host rock.

Dolomite grains are coarse and overgrown by CL-dark drusy quartz types suggesting that these grains pre-date Carlin-type gold mineralization. Furthermore, the coarse grain size, lack of spatial association with ore stage silicification events, and the observation

that dolomite grains are overgrown by all silicification events, suggest that dolomite precipitation likely correlates with diagenesis of the original host rock.

Main-Ore-Stage

An assemblage of minerals, including four types of jasperoid quartz, calcite, and multiple types of Au-bearing pyrite, precipitated during the Carlin-type mineralization event (Figure 8). The main-ore-stage mineralization event includes jasperoid formation which is coeval with gold precipitation. Locally, four different types of jasperoid are identified. Each jasperoid type is distinguished by textures, grain size, and geologic setting. The most critical property of all four jasperoid types is its strong spatial relationship with ore-stage pyrite types. These four jasperoid types host abundant ore stage pyrite, which is disseminated throughout these jasperoid zones. Furthermore, all four jasperoid types exhibit CL-dark luminescence, and are overgrown by CL-dark late-ore-stage drusy quartz.

Q10a jasperoid consists of fine-grained, interlocking quartz crystals (~5 μm) and comprises individual clasts of brecciated samples (Figures 15a, 15b). The fine-grained, interlocking crystals that make up this jasperoid type host abundant solid calcite inclusions as well as unidentified inherited material. Inherited material gives these jasperoid zones a blocky appearance. Q10a jasperoid clasts are overgrown by CL-dark, intra-vug drusy quartz, intergrown by CL-dark intra-matrix drusy quartz, and cross-cut by both CL-dark late-ore-stage and CL-bright post-ore-stage quartz veins.

Q10b jasperoid quartz represents matrix zones within brecciated samples (Figures 15c, 15d). These matrix zones reflect silicified debris flows that are poorly sorted and have a brecciated appearance. Q10b jasperoid represents the matrix of these apparent

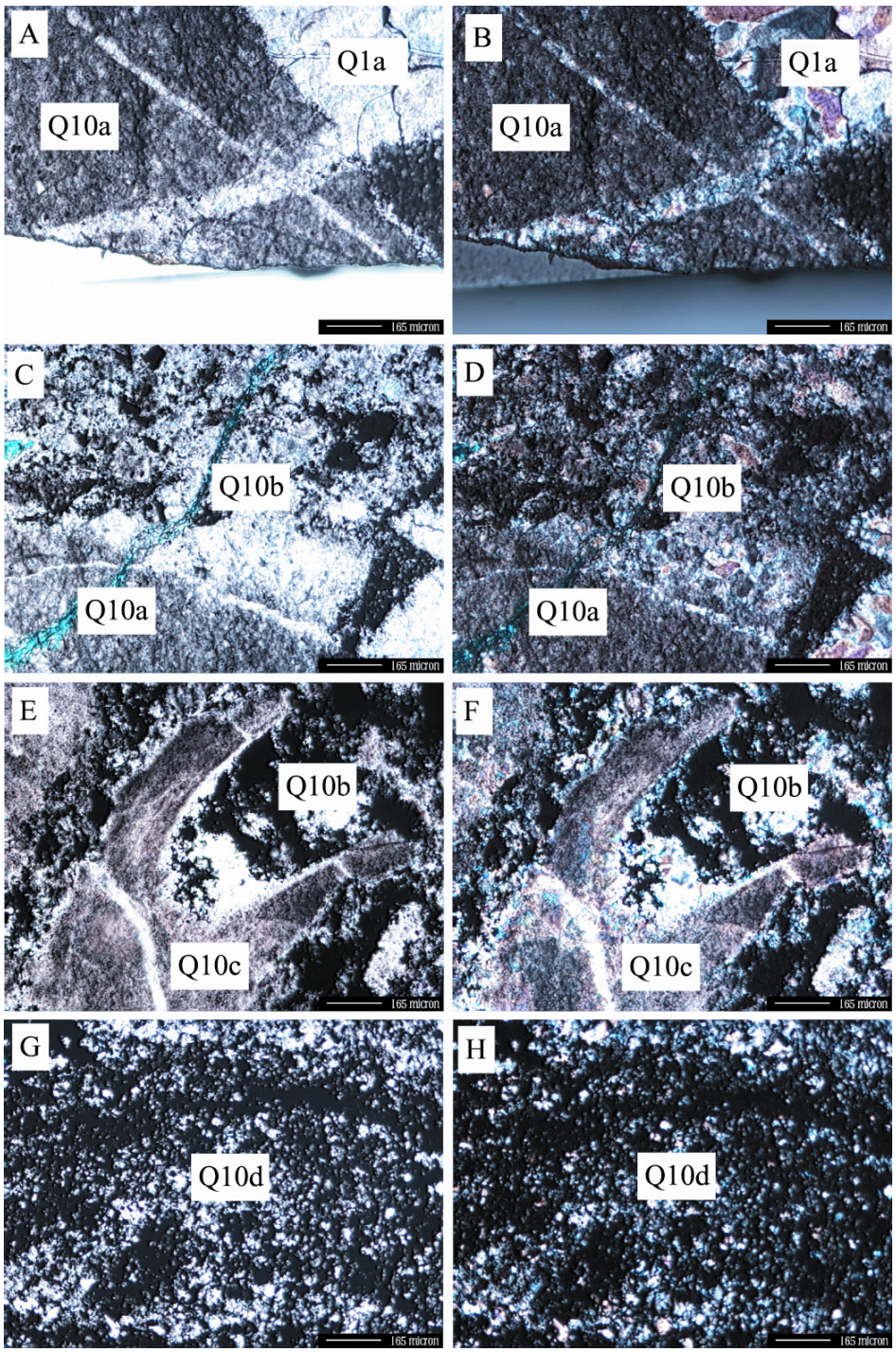

Figure 15. Photomicrographs of the different ore stage jasperoid types classified at Betze-Post. Q10a jasperoid under plane polarized transmitted light (A) and under crossed-polarized transmitted light (B). Q10b jasperoid under plane polarized transmitted light (C) and under crossed-polarized transmitted light (D). Q10c jasperoid under plane polarized transmitted light (E) and under crossed-polarized transmitted light (F). Q10d jasperoid under plane polarized transmitted light (G) and under crossed-polarized transmitted light (H).

brecciated zones. Q10b jasperoid consists of fine-grained, interlocking, euhedral quartz crystals that are slightly coarser than Q10a jasperoid quartz crystals. Q10b jasperoid also hosts abundant calcite inclusions, abundant inherited material, and also displays a blocky appearance in which darker sub-zones of jasperoid are randomly exposed throughout the matrix zones. Q10b jasperoid zones are found adjacent to Q10a jasperoid zones, are overgrown by CL-dark drusy quartz, and crosscut by CL-bright post-ore-stage quartz veins (Q6).

Q10c jasperoid quartz comprises silicified fossil clasts localized within individual breccia clasts and matrix zones (Figures 15e, 15f). Q10c jasperoid consists of fine-grained, interlocking quartz crystals. This jasperoid type maintains the morphology inherited from the original fossil clasts that were replaced. This jasperoid type is located within replaced breccia clasts (Q10a) and breccia matrix zones (Q10b), are overgrown by CL-dark intra-clast (Q1a) and intra-matrix (Q3a) drusy quartz.

Q10d jasperoid quartz comprises undisturbed, unbrecciated, jasperoid zones (Figures 15g, 15h). This jasperoid type also hosts very fine-grained quartz crystals that contain abundant calcite inclusions and inherited material. This type differs from the previous three jasperoid types by hosting the lowest amount of inherited material. Q10d jasperoid areas are intergrown by CL-dark intra-clast drusy quartz (Q2a).

Solid calcite inclusions are hosted within jasperoid crystals and at the interface between ore stage jasperoid and late-ore-stage drusy quartz (Figure 16). Solid calcite inclusions range between 1 μm and 5 μm and are detected using reflected light microscopy.

Multiple types of ore-stage pyrite generations were identified based on distinct textures, morphologies, colors, polish, relief, and size. Distinct textures include 1) porous grains, 2) massive rims encompassing multiple cores of pre-ore pyrite (Figure 17a), 3) narrow rims overgrowing pre-existing pyrite grains (Figure 17b), 4) grains overgrown by drusy quartz, 5) occurrences within clusters, or 5) occurrences along fractures (Henkelman, 2004).

Observed morphologies of ore-stage pyrite grains include massive, anhedral, euhedral, prismatic, and bladed forms. Ore-stage pyrite grains generally display a brassy color, fair to good polish, and range between 15 μm to 50 μm in size but may reach 250 μm. Ore-stage pyrite grains show a wide range in terms of relief with some types displaying low relief while other types of ore-stage pyrite grains display a higher relief (Henkelman, 2004). LA-ICP-MS analysis of these pyrite grains identified elevated concentrations of Au as well as other trace elements that are commonly linked with ore-bearing pyrite grains in Carlin-type systems. Ore stage pyrite grains are localized within CL-dark jasperoid clasts, matrix, fossil clasts, and undisturbed zones, and along the contact between CL-dark ore stage jasperoid and CL-dark late-ore-stage drusy quartz.

Discussion of Main-Ore-Stage Mineralogy

The composition of the original carbonate protolith (i.e. silty limestone, breccias, fossil hash, and fossil clasts), the original grain size of the replaced material, and the temperature and pressure conditions of the silicification event can govern the degree of replacement and the formation of jasperoid. Consequently, each ore stage jasperoid type described at Betze-Post reflects differences in these conditions. Q10a, fine-grained jasperoid comprise breccia clasts and are believed to have inherited the original grain size

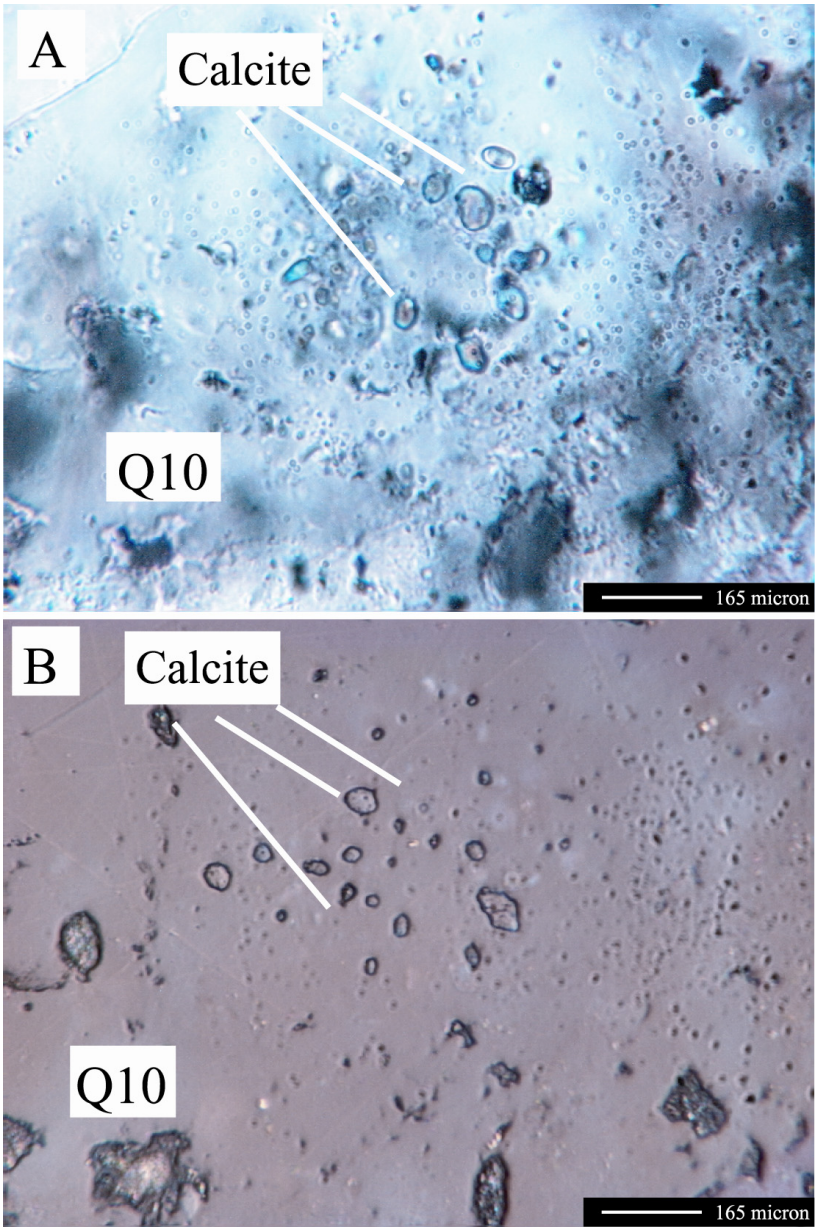

Figure 16. Photomicrographs of ore stage solid calcite inclusions in North Betze sample SJ-305C-1041.2. Solid calcite inclusions are commonly identified within Q10 jasperoid zones. A) Calcite inclusions under plane polarized transmitted light. B) Calcite inclusions under plane polarized reflected light.

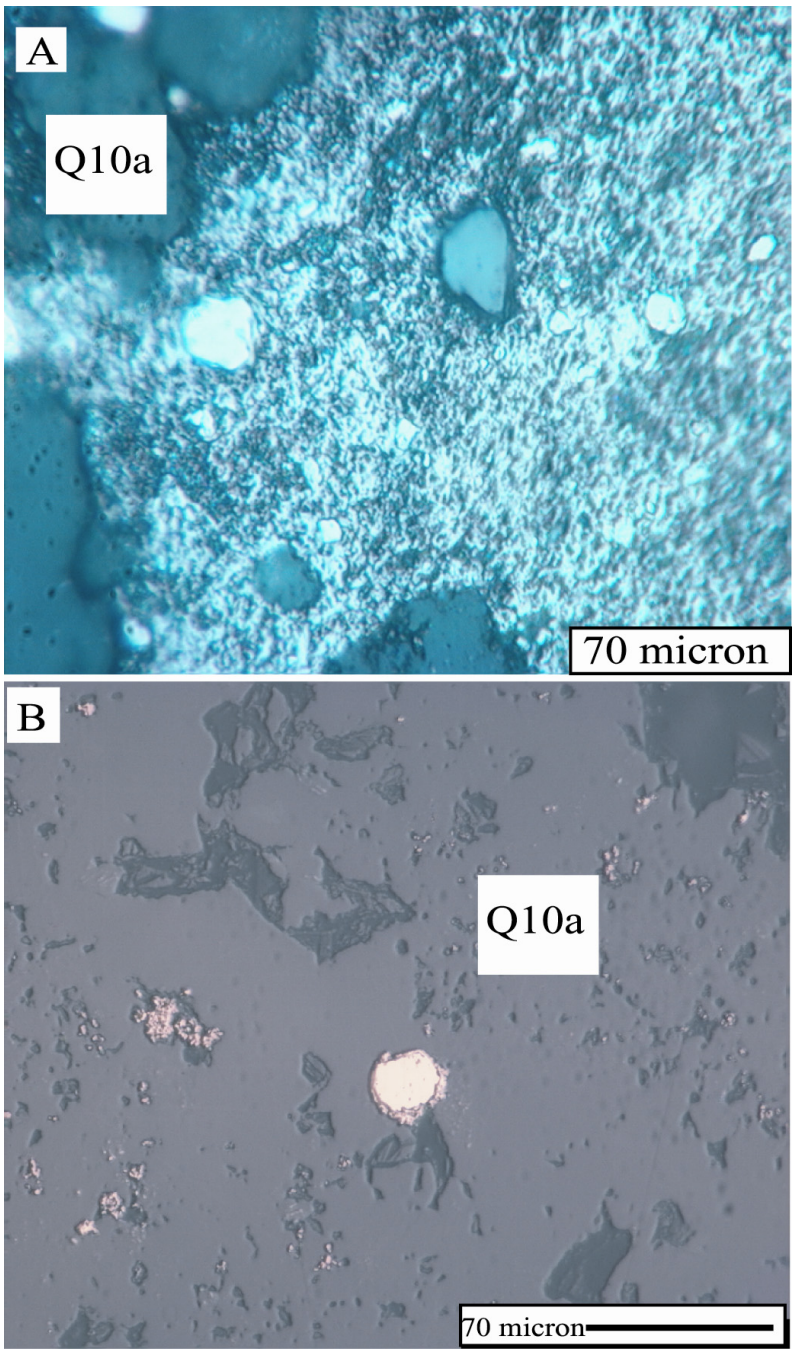

Figure 17. Ore stage pyrite grains from North Betze sample SJ-456C-1167.0. A) Distinctive texture for ore stage pyrite displaying massive fine-grained ore-stage pyrite rim overgrowing multiple pre-ore-stage pyrite cores. B) Second distinctive ore-stage pyrite texture showing narrow ore-stage pyrite rim overgrowing pre-ore-stage pyrite core.

of the replaced carbonate host rock. Q10a jasperoid zones are usually adjacent to Q10b, slightly coarser grained, jasperoid zones that comprise matrix/debris flow zones in brecciated samples. The coarser grains identified in Q10b zones may reflect the slightly coarser nature of the host material being replaced. Poorly sorted debris flows can have a brecciated appearance and can act as matrix for brecciated samples and the poorly sorted nature of these zones can produce a slightly coarser grained jasperoid. Q10c jasperoid with replaced fossil clasts occurs within Q10a and Q10b jasperoid zones. Chemically precipitated fossil clasts usually display a very-fine grained nature. The very fine-grained nature of Q10c jasperoid is believed to be a product of the original grain size of calcite in the fossil clast it replaced. Q10d nonbrecciated jasperoid zones are isolated from other jasperoid types excepting Q10c jasperoid. All four jasperoid types are commonly present across all five ore zones, and multiple jasperoid types are identified within individual samples.

All four jasperoid types display CL-dark luminescence, are overgrown by CL-dark late-ore-stage drusy quartz, and are cross-cut by both CL-dark, late-ore-stage and CL-bright, post-ore-stage quartz veins. These overgrowth and crosscutting relationships clearly define CL-dark jasperoid types as main-ore-stage silicification types.

Solid calcite inclusions in jasperoid crystals are interpreted to form during transitory calcite stability coeval with replacement of carbonate by silica. Petrographic observations of calcite inclusions, which include presence along growth zones within quartz crystals, fine grain size, and presence along the base of late-ore-stage drusy quartz crystals, suggest that these calcite inclusions formed during replacement by precipitation of jasperoid. The presence of solid calcite inclusions in jasperoid indicates quartz

replaced calcite and the inclusions were used in this study to classify different jasperoid types.

The consistent spatial relationships between Q10 quartz types and Au-bearing pyrite grains demonstrate that Q10 quartz types are temporally related to gold-bearing pyrite grains. This indicates that the ore fluid, where quartz accompanies Au, was also saturated in silica and silica replaced carbonate during gold deposition.

Late-Ore Mineralization

An assemblage of minerals has been identified at Betze-Post to precipitate during the later stages of the Carlin-type mineralization event. The minerals in this assemblage are termed late-ore-stage and include drusy quartz, vein quartz, and realgar (Figure 8).

Petrography has identified multiple types of drusy quartz based on grain size, morphology, setting, and unique petrographic properties. Three late-ore-stage drusy quartz types were identified and constrained by combining petrography, CL, and BEI studies (Table 1). An important observation in constraining these quartz types as late-ore-stage include that they host concentrations of ore-stage pyrite grains along the base of their crystals at the interface between these drusy quartz crystals and CL-dark, ore stage jasperoid. Also, these quartz types share the same CL-dark luminescence as ore-stage jasperoid displays.

Q1a drusy quartz occupies vugs and fractures within brecciated and non-brecciated samples and is termed intra-vug drusy quartz (Figure 18). These drusy quartz crystals are localized along the margins of breccia clasts and fill available open space. Q1a drusy quartz crystals are defined as interlocking, euhedral, elongated crystals that range between 100 μm and 800 μm in length and coarsen outward into vugs. Abundant solid

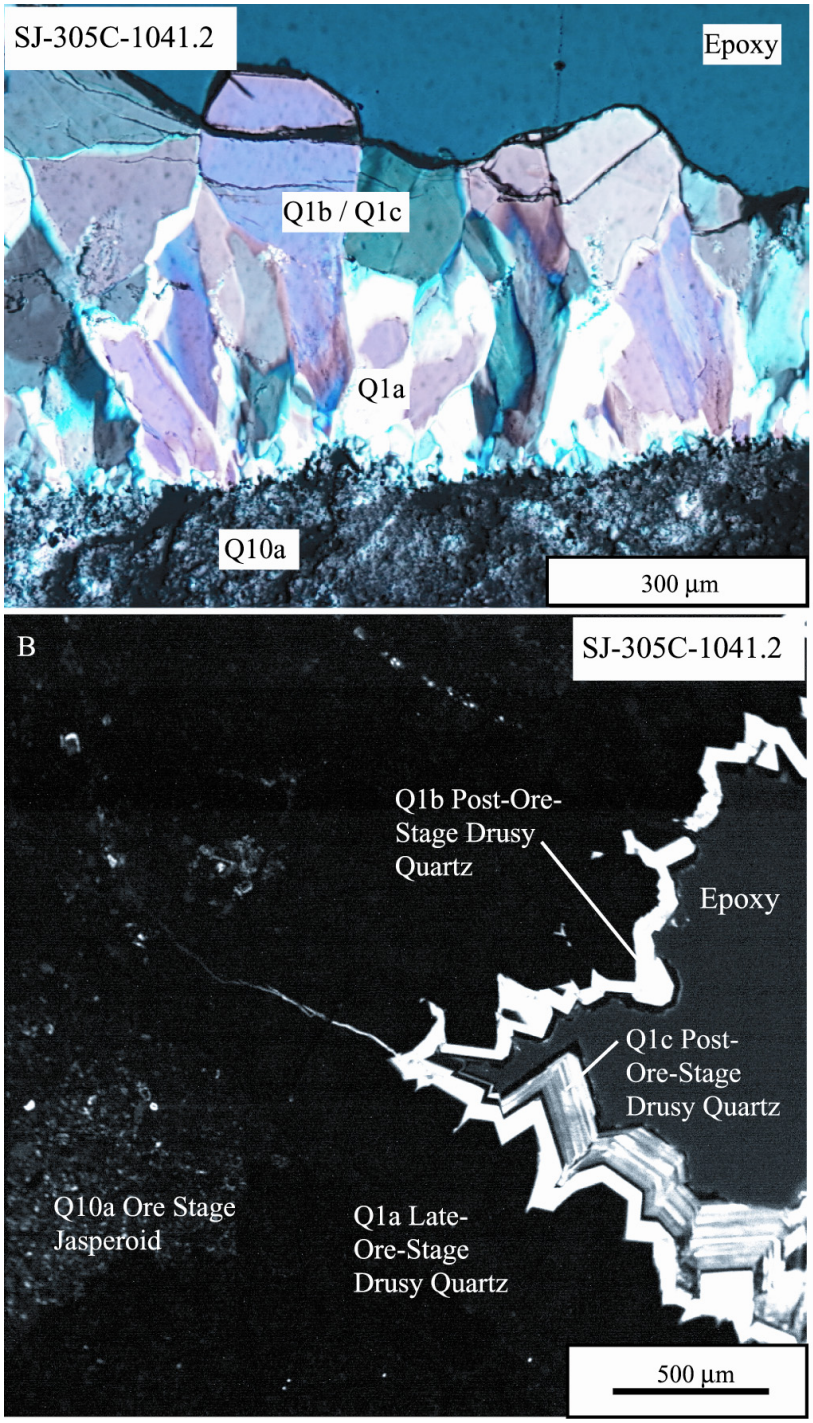

Figure 18. A) Photomicrograph of Q1 quartz types under plane polarized transmitted light. Q1 drusy quartz overgrows ore-stage jasperoid within drusy areas. Q1 quartz types coarsen outwards as crystals get younger. Q1a drusy quartz crystals display elongated crystals whereas Q1b and Q1c drusy quartz crystals are equant and only differ in luminescence. B) CL image displaying all three Q1 drusy quartz types.

calcite inclusions are present at the base of these drusy quartz crystals along the interface with drusy quartz and the ore stage jasperoid. Rare two-phase secondary fluid inclusion assemblages are present within Q1a crystals; however, these inclusions are < 2μm in diameter and too small to analyze.

Q2a drusy quartz crystals occur within individual clasts in brecciated areas and are termed intra-clast drusy quartz (Figure 19). Q2a drusy quartz crystals are defined as coarse, euhedral, elongated, interlocking crystals that range between 20 μm and 200 μm and coarsen into vugs. Q2a quartz crystals also host abundant calcite inclusions along the base of individual crystals.

Q3a drusy quartz crystals (Figure 19) occur within matrix zones of brecciated samples and are termed intra-matrix drusy quartz. These quartz crystals are also euhedral, elongated crystals that range from 100 μm to 400 μm, and also coarsen outward. The same occurrence of solid calcite inclusions seen in the two previous drusy quartz types are also identified in Q3a drusy quartz crystals.

Quartz veins constitute a second type of late-ore-stage open-space filling quartz and are termed Q5 quartz. Intra-clast (Q5) quartz veins terminate at the margin of individual breccia clasts (Figure 20). Furthermore, these quartz veins crosscut ore stage jasperoid clasts only and are overgrown by post-ore-stage drusy quartz generations. Q5 quartz veins have euhedral, elongated quartz crystals that interlock and average 10 μm in length. The crystals that comprise these quartz veins display CL-dark luminescence.

Realgar is present in samples collected from Deep Post. Realgar crystals are euhedral, range between 200 μm and 500 μm, and occupy veins that crosscut ore-stage jasperoid zones within brecciated and nonbrecciated samples (Figure 21). Realgar

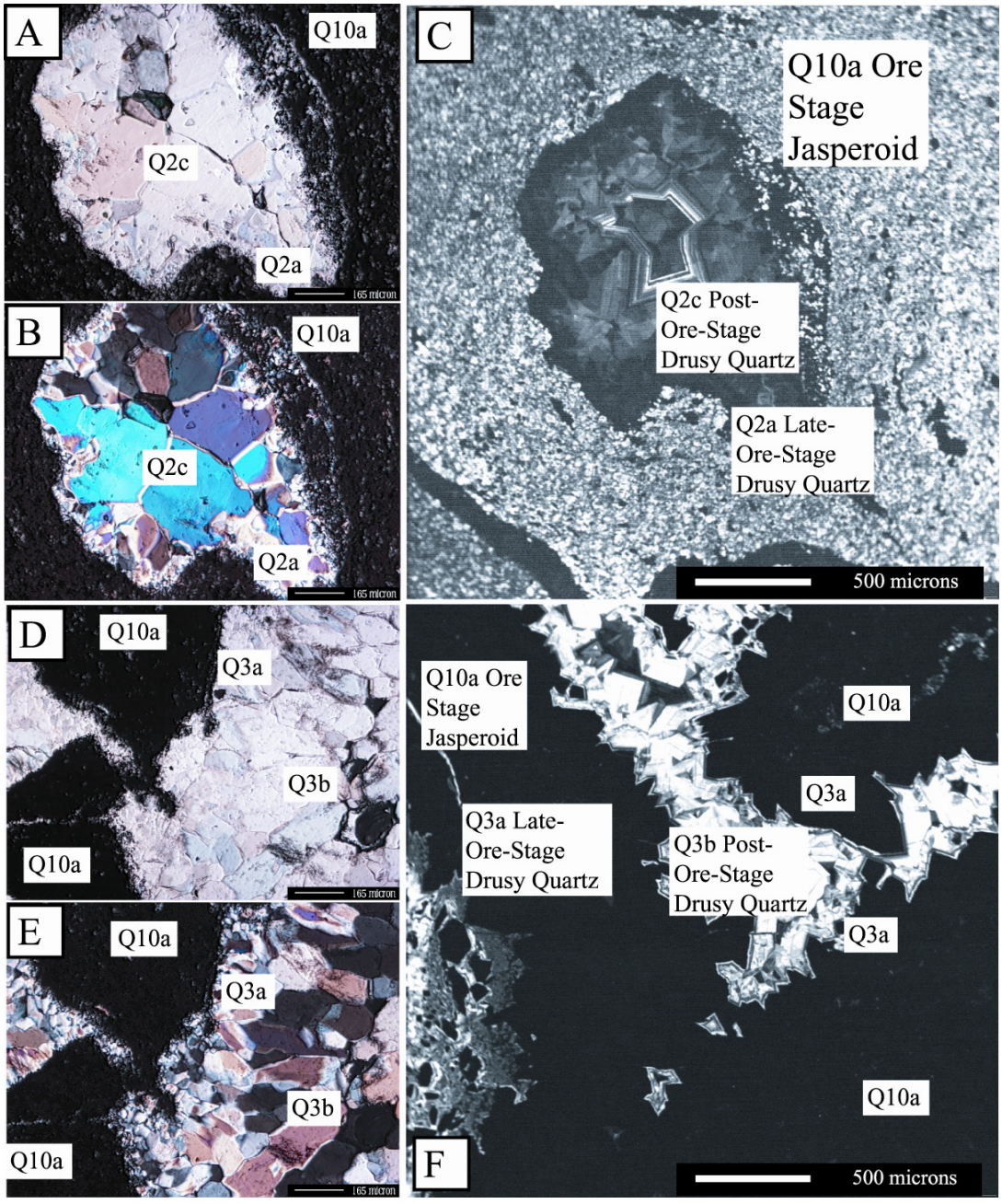

Figure 19. Q2 quartz types from North Betze Samples SJ-305C-1069.7 and SJ-305C-1041.2. A) Photomicrograph of Q2a and Q2c drusy quartz types taken under plane polarized transmitted light and under crossed-polarized transmitted light (B). C) CL image illustrating Q2a and Q2c drusy quartz. D) Photomicrograph of Q3a and Q3b drusy quartz types taken under plane polarized transmitted light and under crossed-polarized transmitted light (E). F) CL image illustrating Q3a and Q3b drusy quartz.

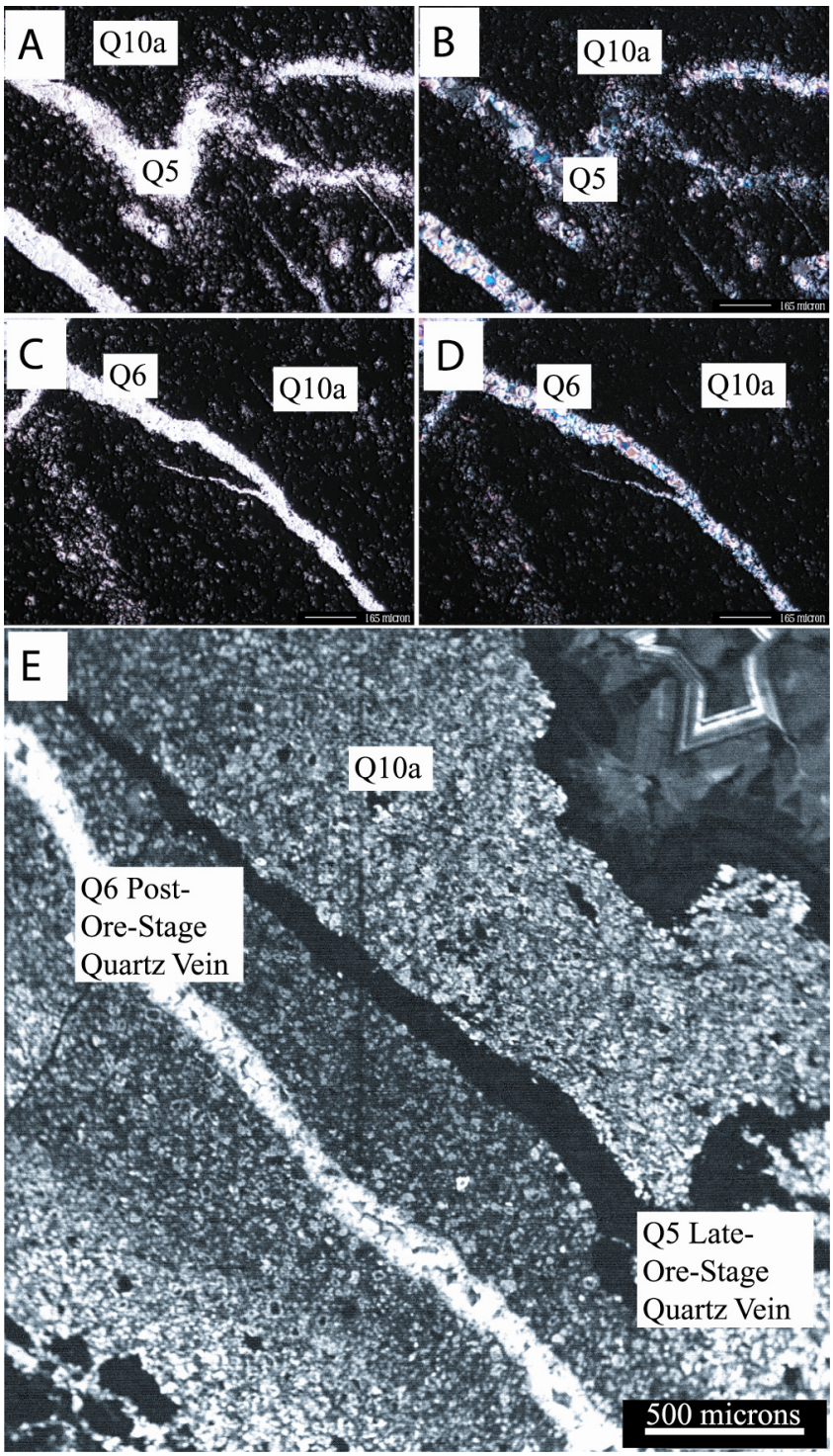

Figure 20. Q5 and Q6 quartz veins from North Betze sample SJ-305C-1069.7. Photomicrograph of Q5 quartz veins taken under plane polarized transmitted light (A) and under crossed-polarized transmitted light (B). C) Photomicrograph of Q6 quartz veins taken under plane polarized transmitted light and under crossed-polarized transmitted light (D). E) CL image illustrating the relative luminescence of Q5 and Q6 quartz veins.

veins overgrow CL-dark late-ore-stage drusy quartz along fractures in brecciated samples (Figure 21).

Discussion of Late-Ore-Stage Mineralogy

CL-dark open-space drusy quartz is determined to be late-ore-stage. Textural relationships between ore stage jasperoid clasts and late-ore-stage drusy quartz suggests that the precipitation of CL-dark drusy quartz and CL-dark vein quartz overlapped with the waning stages of ore stage jasperoid precipitation. This interpretation is based on several observations. First, CL-dark drusy quartz overgrows CL-dark jasperoid. Second, CL-dark quartz veins crosscut CL-dark jasperoid. Third, abundant solid calcite inclusions are present along the boundary between ore-stage jasperoid and the first layer of late-ore-stage drusy quartz and vein quartz. Fourth, solid calcite inclusions are not identified at the terminations of these initial late-ore-stage quartz crystals. Fifth, solid calcite inclusions are not present within subsequent CL-dark late-ore-stage quartz layers. These textures indicate that transitory calcite stability was ongoing during the initial stages of late-ore-stage quartz precipitation and ceased by the time subsequent layers of late-ore-stage, CL-dark quartz precipitated.

Late-ore-stage quartz is pervasive across all ore zones at Betze-Post. The physical similarity between all three types of late-ore-stage drusy quartz crystals supports the likelihood that they were all precipitated during the same hydrothermal event. Q1a and Q2a quartz are both CL-dark; however, they differ in geologic setting. It is possible that some features of the original host rock (i.e. fossil clasts) were leached providing open-space for euhedral interlocking CL-dark quartz (Q2a) to precipitate. CL-dark intra-matrix drusy quartz (Q3a) is likely coeval with other CL-dark quartz types based on its

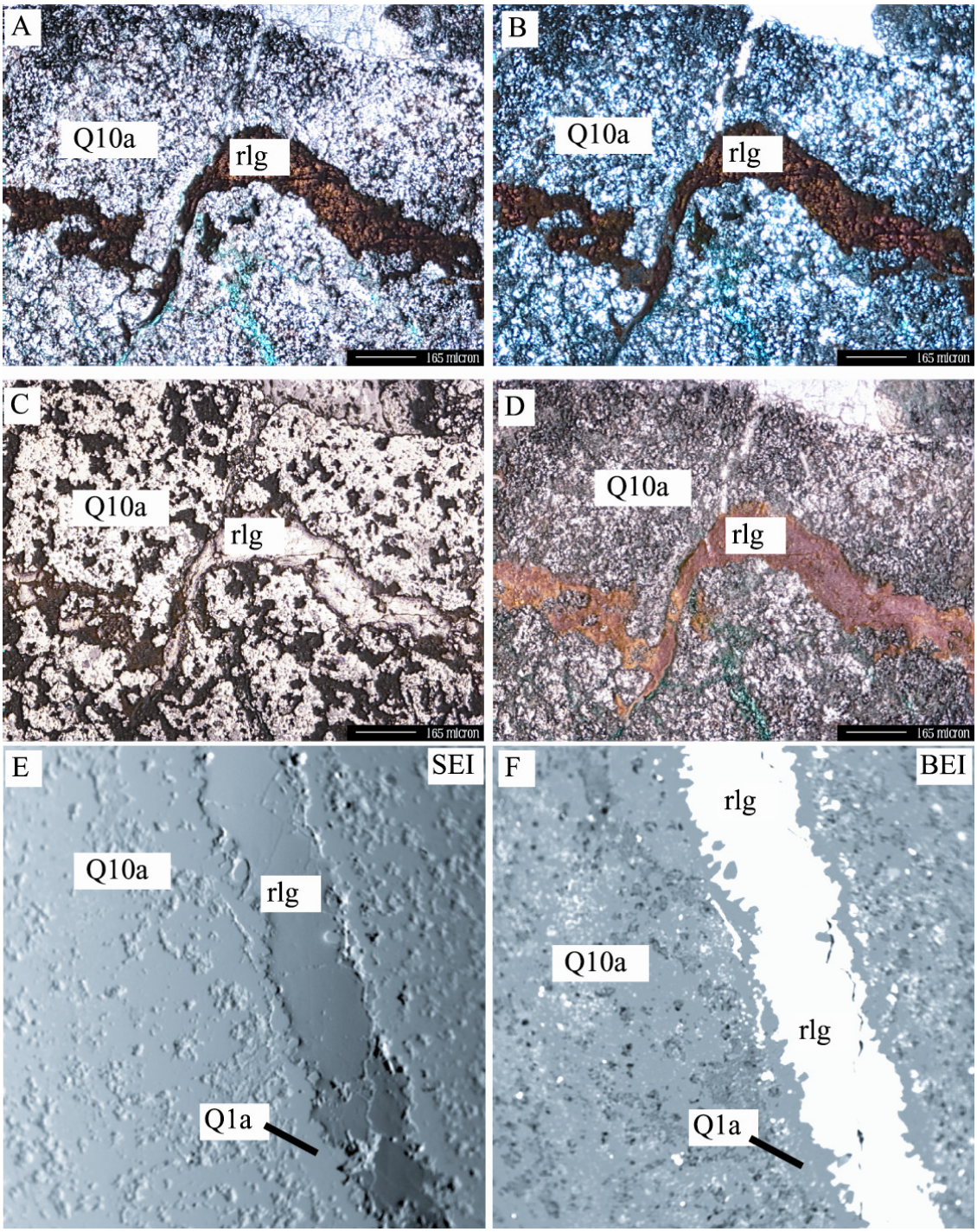

Figure 21. Late-ore-stage realgar from Deep Post sample P-175C-1312.0. A) Realgar vein under plane polarized transmitted light and under crossed-polarized transmitted light (B). C) Realgar vein under plane polarized reflected light and under crossed-polarized reflected light (D). E) Secondary electron image (SEI) illustrating realgar veins overgrowing Q1a late-ore-stage drusy quartz. F) BEI of same view.
similar physical attributes and luminescence.

CL-dark, intra-clast, quartz veins crosscut individual ore stage CL-dark jasperoid clasts but terminate at younger drusy quartz types. This observation suggests that CL-dark quartz vein precipitation was coeval with the later stages of the hydrothermal event that precipitated CL-dark jasperoid and coeval with the onset of CL-dark drusy quartz precipitation.

Realgar crystals are identified in several samples collected from the Deep Post ore zone. Realgar veins overgrow CL-dark drusy quartz types and crosscut CL-dark ore stage jasperoid zones indicating that realgar precipitated after the precipitation of late-ore-stage drusy quartz generations. It is difficult to constrain the absolute timing of realgar veins at Deep Post due to its lack of spatial association with post-ore-stage quartz types. Late-ore-stage realgar and orpiment are commonly found in Carlin-type gold systems due to the arsenic-rich nature of these systems (Cline and Hofstra, 2000); thus, it is reasonable to interpret that they are part of the late-ore stage at Betze-Post.

Post-ore Mineralization

An assemblage of minerals has been identified as post-dating the Carlin-type mineralization event. This assemblage includes several types of drusy quartz, a single type of vein quartz, pyrite, calcite, barite, and marcasite (Figure 8).

Four types of drusy quartz are identified at Betze-Post to post-date the Carlin-type mineralization event (Table 1). These drusy quartz types are primarily discerned by relative luminescence and geologic setting (Table 1). Q1b and Q1c drusy quartz crystals occur within vug settings and share the same physical properties as Q1a drusy quartz crystals with exceptions to crystal morphology and luminescence (Figure 18). Q1b drusy quartz crystals are coarser than Q1a crystals, range between 200 μm and 800 μm in

diameter, and display an equant crystal morphology. Q1b and Q1c drusy quartz types differ only in luminescence and Q1b drusy quartz crystals display CL-bright luminescence while Q1c drusy quartz crystals display CL-multiple luminescence. Textural observations show that Q1c drusy quartz overgrows Q1b drusy quartz. Neither Q1b nor Q1c drusy quartz are spatially related to Au-bearing pyrite grains.

Q2c drusy quartz crystals are localized within individual clasts in brecciated samples and are termed intra-clast drusy quartz similar to the Q2a drusy quartz crystals they overgrow (Figure 19). This drusy quartz forms very coarse equant crystals that range between 200 μm and 600 μm and displays CL-multiple luminescence. Petrographic and backscatter analysis show this drusy quartz type to have no spatial association with Au-bearing pyrite grains.

Q3b drusy quartz crystals are localized within matrix zones in brecciated samples and are termed intra-matrix drusy quartz (Figure 19). Q3b drusy quartz crystals are similar to Q3a drusy quartz with exceptions to grain morphology, size, and luminescence. Q3b drusy quartz grains are more equant than Q3a drusy quartz. Furthermore, Q3b drusy quartz crystals display CL-bright luminescence and are very coarse ranging between 100 μm and 400 μm. Q3b drusy quartz overgrows Q3a drusy quartz crystals and also has no spatial association with Au-bearing pyrite grain populations.

Q6, CL-bright, inter-clast quartz veins have euhedral interlocking quartz crystals that are medium-sized ranging between 20 μm and 200 μm (Figure 20) These quartz veins crosscut CL-dark silicified breccia clasts (Q10a) and matrix areas (Q10b) as well as CL-dark late-ore-stage drusy quartz. These quartz veins also have no spatial connection with

Au-bearing pyrite populations as revealed by petrography and backscatter electron imaging.

Post-ore-stage pyrite was not identified by this study; however, Henkelman (2004) identified a single type of post-ore-stage pyrite. This pyrite type exhibits euhedral crystals with a fair to good polish and high relief. These crystals are also typically coarse averaging 75 μm in diameter.

Post-ore calcite grains are coarse, euhedral grains that usually range between 500 μm and 1000 μm, and are localized along fractures within breccia clasts and matrix zones (Figure 22). These calcite grains display classic calcite cleavage, which displays a distinctive cross hatched appearance. Post-ore calcite grains overgrow CL-bright and CL-multiple drusy quartz types and do not display any spatial correlation with Au-bearing pyrite grains.

Barite crystals are also observed and display similar textures as observed in post-ore-stage calcite crystals. Barite crystals range between 500 μm and 1000 μm, display strong birefringence, and have perfect cleavage (Figure 23). Large two-phase fluid inclusion assemblages are identified in some grains. Barite grains also overgrow CL-bright and CL-multiple drusy quartz types and display no spatial association with Au-bearing pyrite grains.

Marcasite occurs as very coarse grains that occupy open-spaces between post-ore calcite and barite crystals. Euhedral marcasite grains are well polished and can reach up to 1500 μm (Figure 24). Marcasite grains are also localized along the margins of Q2b CL-bright drusy quartz crystals and are inter-grown within areas between post-ore calcite and barite grains.

Discussion of Post-Ore-Stage Mineralogy

Silicification events that precipitated CL-bright and CL-multiple quartz types are interpreted to post-date Carlin-type mineralization. This interpretation is based on observed overgrowth textures, luminosity, and the lack of gold-bearing pyrite grains within these quartz zones. CL-bright drusy quartz types (Q1b and Q3b) overgrow CL-dark drusy quartz indicating these quartz types precipitated after CL-dark quartz and before CL-multiple quartz types. Quartz types with CL-multiple luminosity (Q1c and Q2c) overgrow CL-bright and CL-dark quartz types. This observation suggests that CL-multiple quartz is a result of the latest silicification event at Betze-Post. CL-multiple, intra-vug drusy quartz (Q1b, Q1c), intraclast drusy quartz (Q2c), and intra-matrix drusy quartz (Q3b) overgrow all stages of silicification in the system.

CL-bright interclast quartz veins (Q6) are interpreted to be coeval with other CL-bright quartz types. This interpretation is based on similarities in luminescence with CL-bright and CL-multiple drusy quartz types and the observation that these veins completely crosscut CL-dark jasperoid clasts and transect matrix zones outside of the clasts. Petrographic and CL observations of Q6 quartz veins suggest that these veins filled fractures after brecciation and cementation.

Post-ore-stage calcite and barite crystals overgrow all stages of quartz indicating a post-ore-stage origin. Post-ore marcasite grains also overgrow the latest stages of drusy quartz. Based on these identified overgrowth and crosscutting textures between quartz and calcite, barite, and marcasite it is concluded that all four minerals represent the latest minerals in the paragenesis.

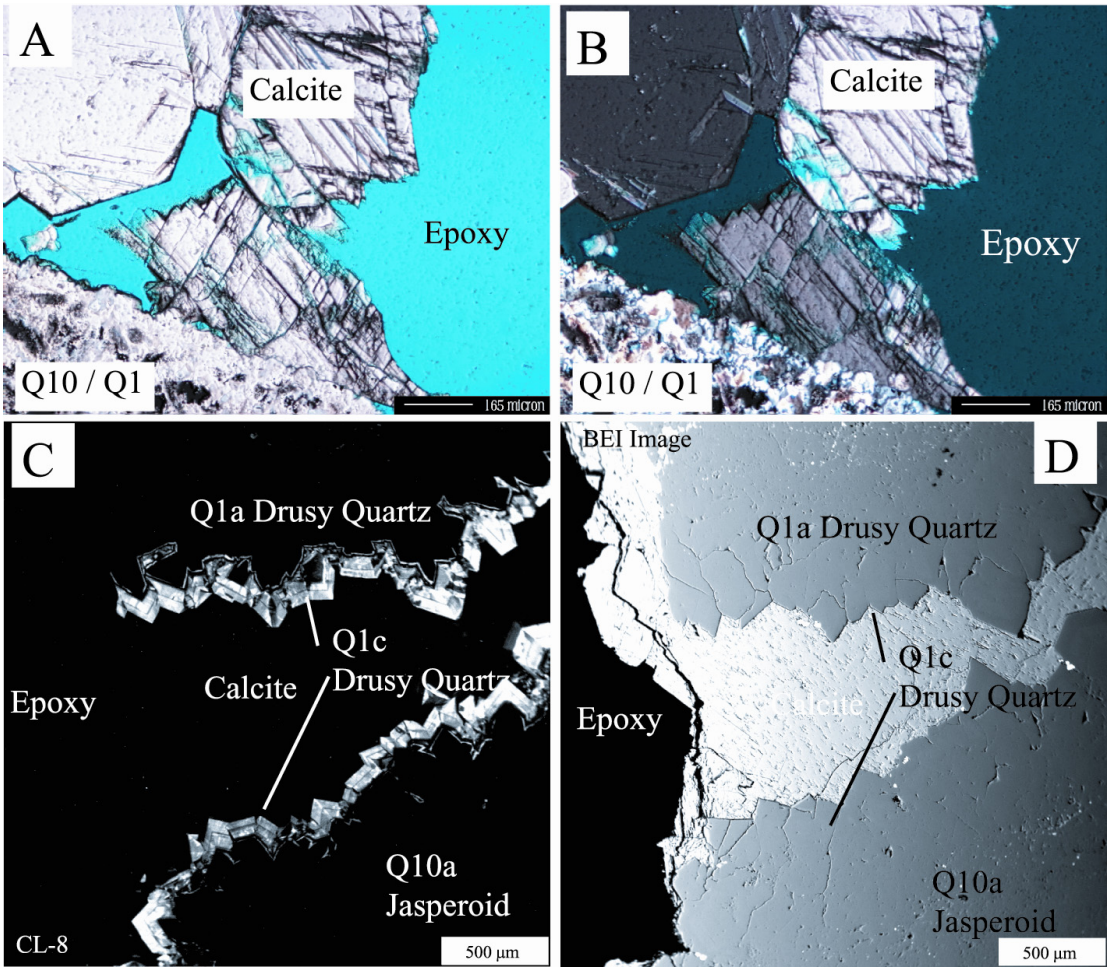

Figure 22. Post-ore-stage calcite from North Betze sample SJ-305C-1072.8. A) Photomicrograph taken under plane polarized transmitted light and under crossed-polarized transmitted light (B). C) CL image of calcite overgrowing post-ore-stage drusy quartz and backscatter electron image (BEI) of same view (D).

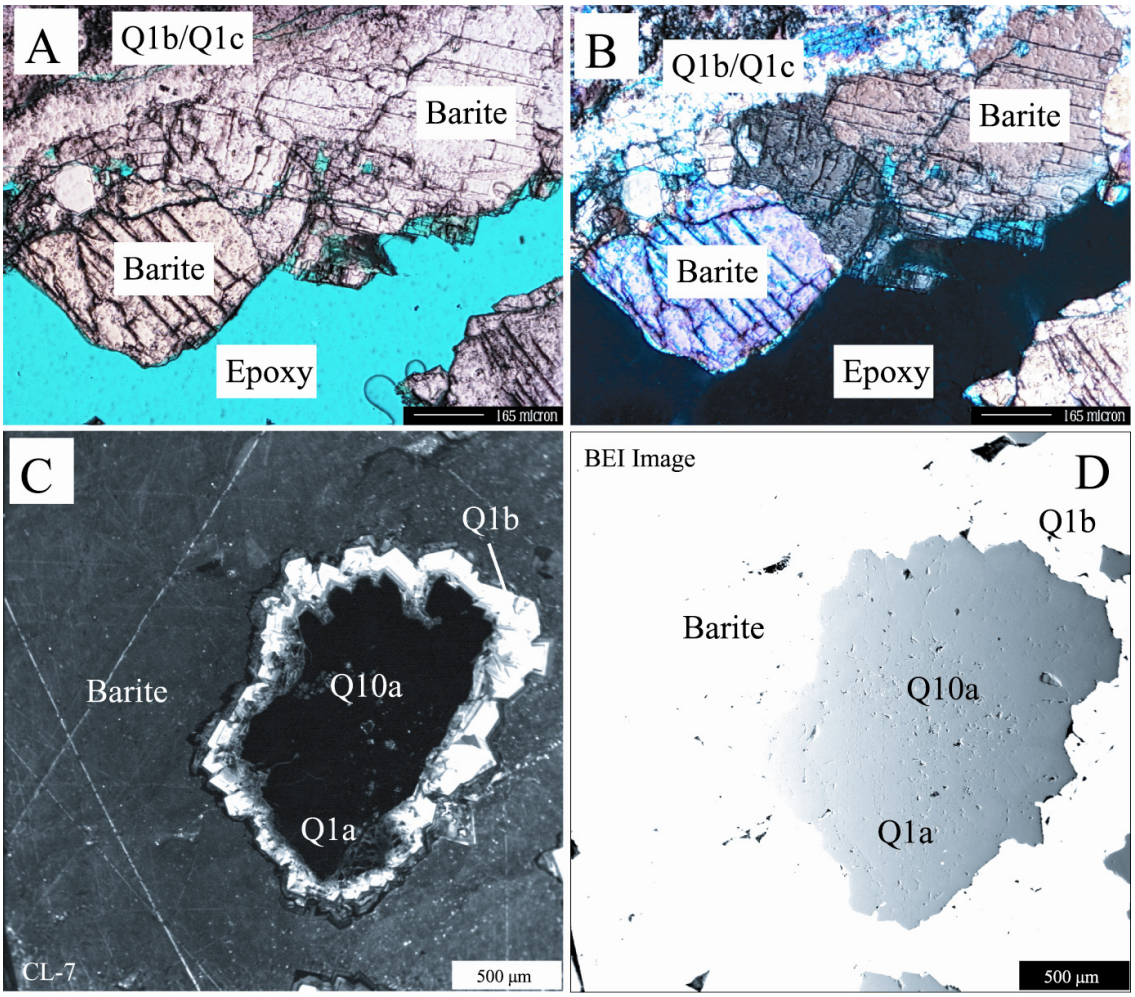

Figure 23. Post-ore-stage barite from North Betze sample SJ-305C-1072.8. A) Photomicrograph taken under plane polarized transmitted light and under crossed-polarized transmitted light (D), C) CL image of barite overgrowing post-ore-stage drusy quartz, D) Backscatter electron image (BEI) of same view.

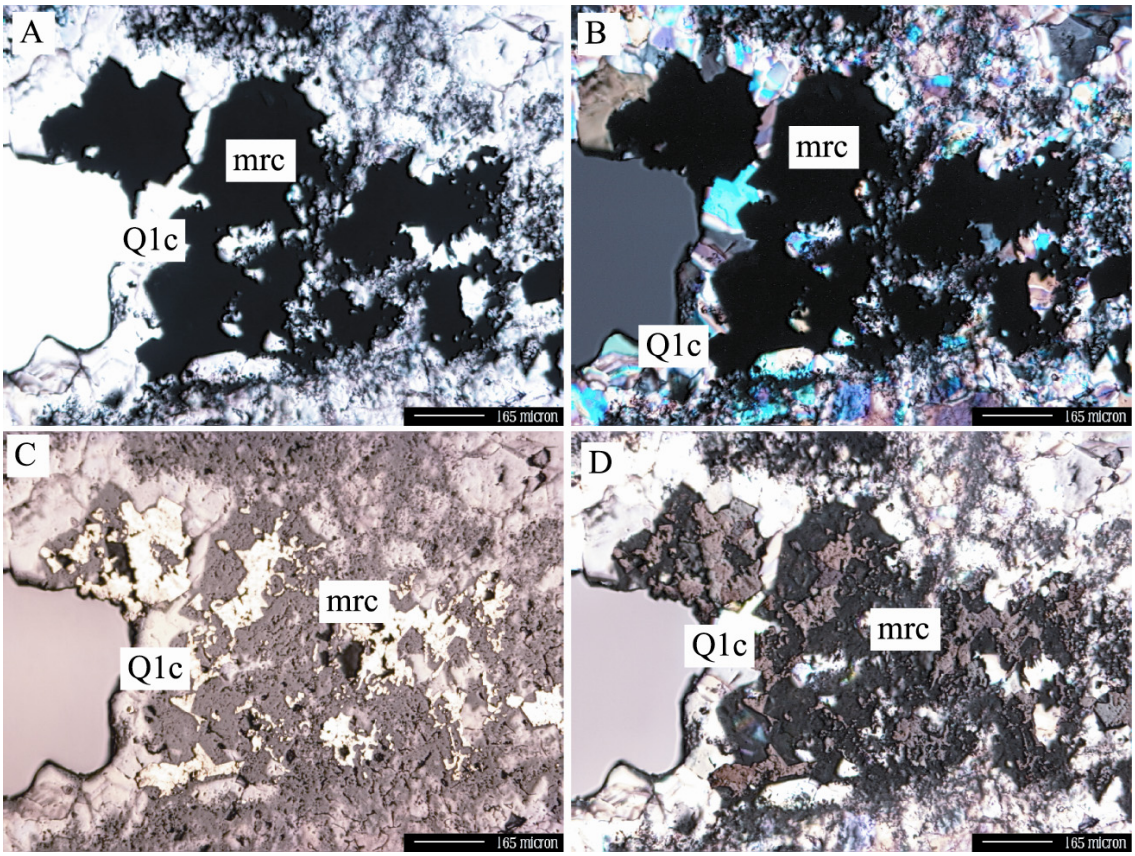

Figure 24. Post-ore-stage marcasite from North Betze sample SJ-263C-1041.5. A) Post-ore marcasite grains under plane polarized transmitted light and under crossed-polarized transmitted light (B). C) post-ore marcasite grains under plane polarized reflected light and under crossed-polarized reflected light (D) (mrc = marcasite).

Mineral Trends at Betze-Post

A variety of quartz types representing multiple mineralization events are present at Betze-Post. Based on observations made during sample collection, petrographic analysis, and cathodoluminescence imaging, distinct silicification trends are present within the different ore zones in the Betze-Post deposit. These trends represent spatial and abundance differences between quartz types within different ore zones. In addition to quartz, spatial trends were identified for accessory and opaque minerals across Betze-Post.

Narrow intervals of elevated gold spatially associated with strong silicification were identified at Deep Post; however, these zones are rare and elevated Au was commonly associated with non-silicified zones. Hand samples that were collected from Deep Post are pervasively silicified, mostly in the form of jasperoid, but also contain minor open-space quartz. Deep Post samples with silicification typically have lower Au concentrations relative to other ore zones, are not brecciated, and primarily contain fine-grained unbrecciated jasperoid (Q10d). Fine-grained, CL-dark, late-ore-stage drusy quartz (Q1) is present at Deep Post and forms a substrate to realgar veins. No CL-bright or CL-multiple, post-ore-stage drusy quartz was present in hand samples from Deep Post. Late-ore-stage realgar was only present in samples from Deep Post and its post-Au age is unconstrained due to the lack of post-ore-stage quartz. The lack of post-ore-stage quartz may be the result of post-ore-stage fluids not accessing the Deep Post ore zone.

Narrow transects of elevated gold spatially associated with strong silicification were also identified at North Post (Figure 25). Hand samples from North Post typically are pervasively replaced by jasperoid and contain minor open-space quartz. These samples

can be brecciated; however the breccias are clast supported and minor matrix zones are present. Jasperoid types at North Post include mostly fine-grained, replaced breccia clast jasperoid (Q10a) and silica replaced unbrecciated samples (Q10d) with minor occurrences of silica replaced matrix jasperoid (Q10b). North Post samples also contain fine-grained, CL-dark, late-ore-stage drusy quartz (Q1a) and fine-grained, CL-dark, late-ore-stage intra-clast drusy quartz (Q2a). Minor CL-multiple, post-ore-stage, drusy quartz is present in samples from North Post.

Betze and North Betze ore zones display abundant intervals showing strong spatial correlation between elevated Au and intense silicification with North Betze displaying the strongest correlations and most abundant silicification (Figures 26, 27, 28). Typical hand samples from Betze and North Betze are strongly silicified possessing abundant jasperoid quartz, drusy quartz, and vein quartz. All four types of jasperoid are consistently present in samples from these two ore zones and are intergrown with one another. Late-ore-stage and post-ore-stage drusy quartz (Q1), intra-clast drusy quartz (Q2), and intra-matrix drusy quartz (Q3) are pervasive across Betze and North Betze and comprise the coarsest drusy quartz collected. Intra-clast, CL-dark, late-ore-stage quartz veins (Q5) and inter-clast, CL-bright, post-ore-stage quartz veins (Q6) are more abundant at North Betze than the other four ore zones. Furthermore, drusy quartz and vein quartz from these ore zones displays the strongest luminescence in post-ore-stage quartz.

Locally, elevated concentrations of Au and silicification occur directly below igneous bodies at Betze and North Betze. These observations are consistent with lateral migration of ore fluids along permeable zones below dikes that promoted alteration, gold mineralization, and quartz precipitation at Betze and North Betze. No apparent genetic

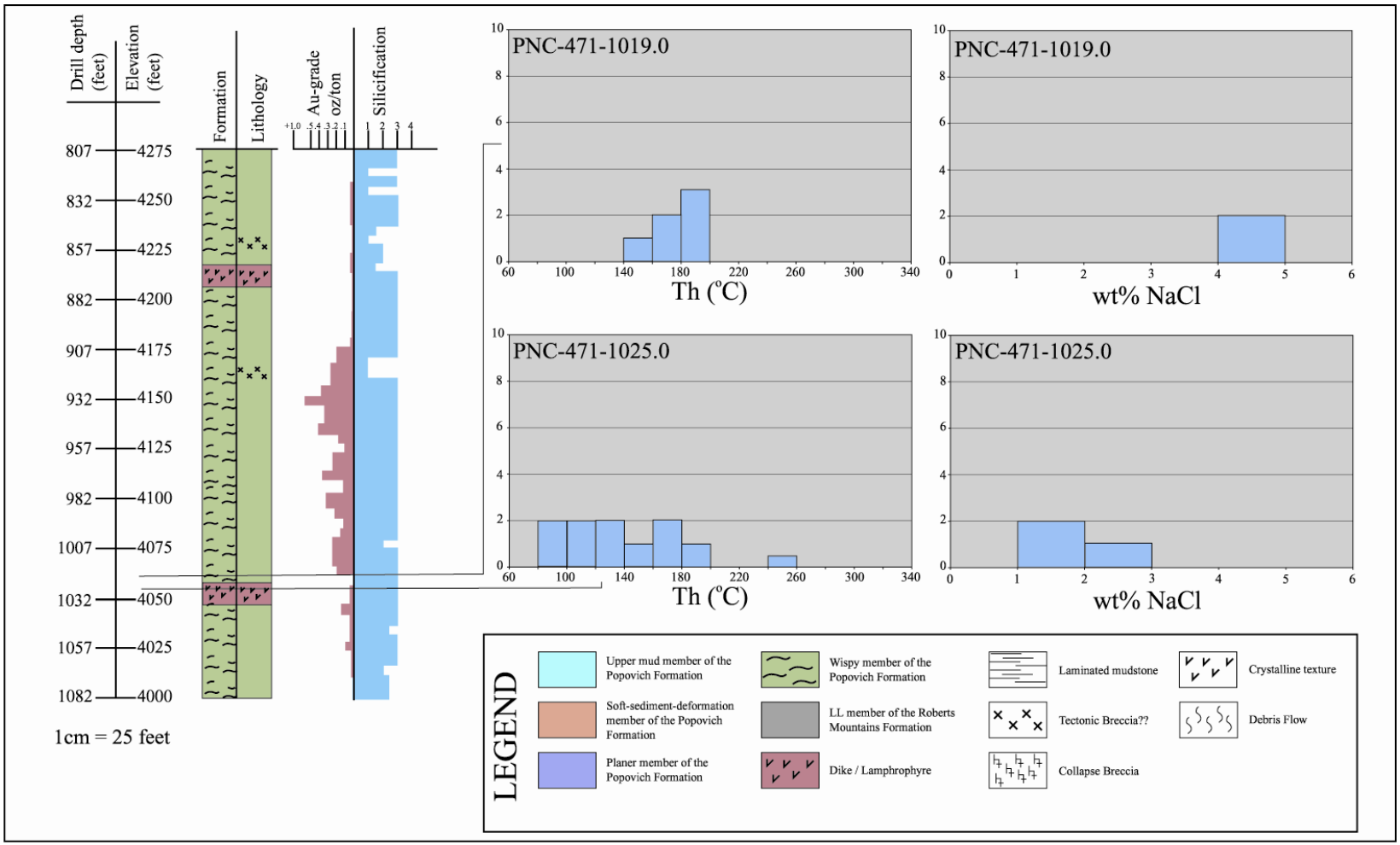

Figure 25. Geologic profile of drill hole PNC-471 at North Post with chemical analyses. Au-grade in 5 foot assays from Barrick Goldstrike. Silicification is the abundance of both replacement and open-space quartz present (a value of 1 is low indicating a sparse presence while a value of 4 is high indicating a pervasive presence).

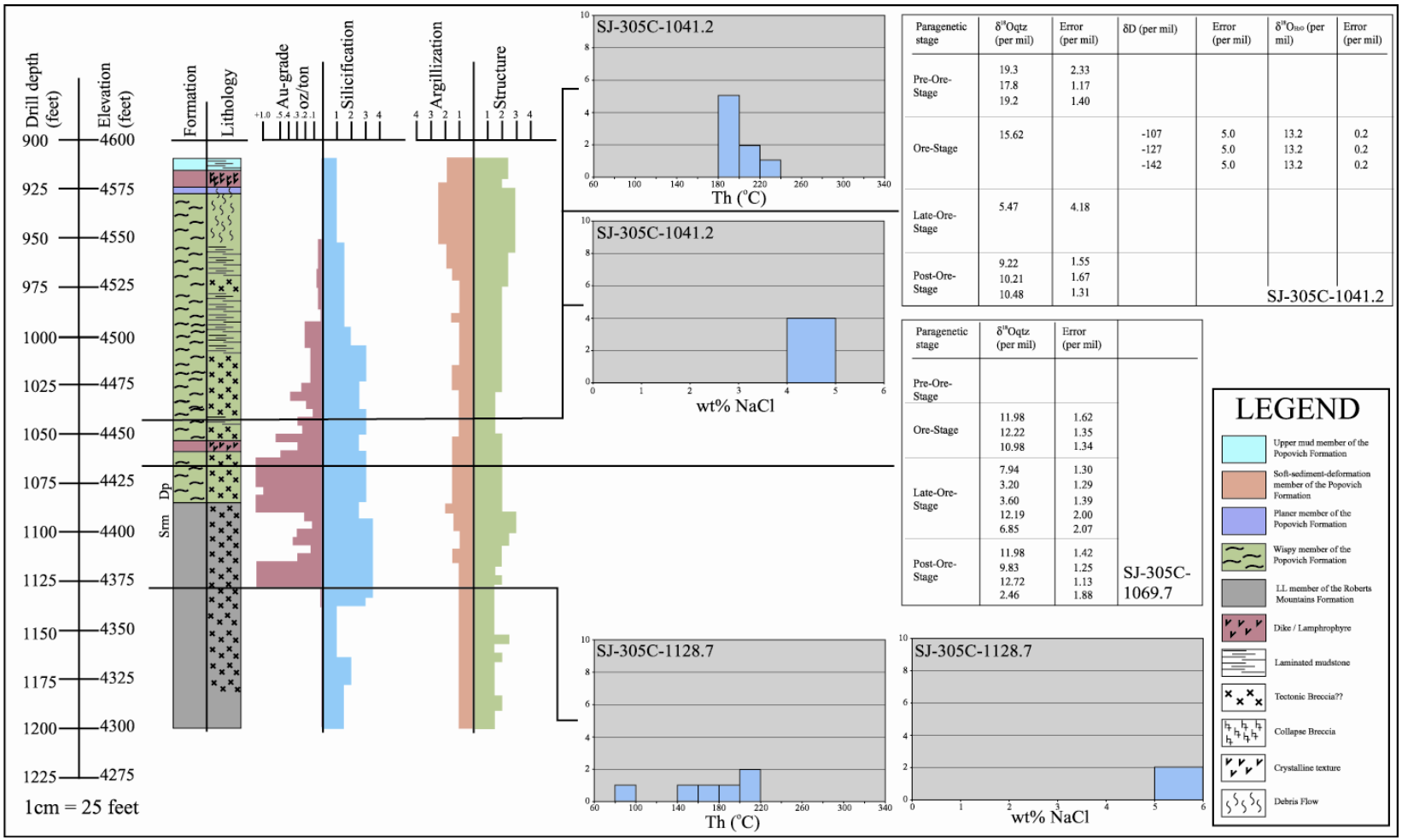

Figure 26. Geologic profile of drill hole SJ-305C at North Betze with chemical analyses. Au-grade in 5 foot assays from Barrick Goldstrike. Silicification is the abundance of both replacement and open-space quartz present, argillization is abundance of clay present, and structure indicates the degree of fracturing (a value of 1 is low indicating a sparse presence while a value of 4 is high indicating a pervasive presence).

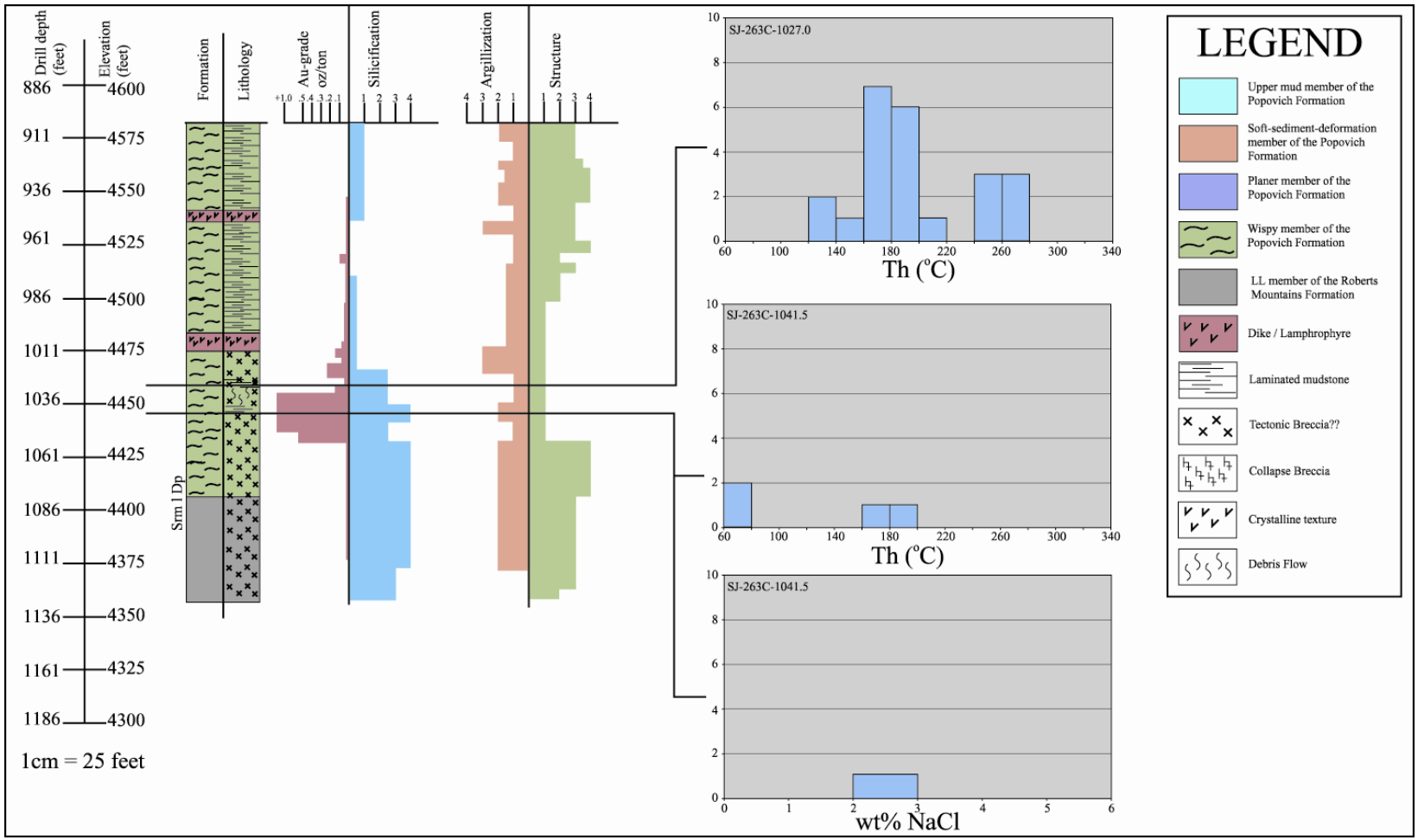

Figure 27. Geologic profile of drill hole SJ-263C at North Betze with chemical analyses. Au-grade in 5 foot assays from Barrick Goldstrike. Silicification is the abundance of both replacement and open-space quartz present, argillization is abundance of clay present, and structure indicates the degree of fracturing. (A value of 1 is low indicating a sparse presence while a value of 4 is high indicating a pervasive presence).

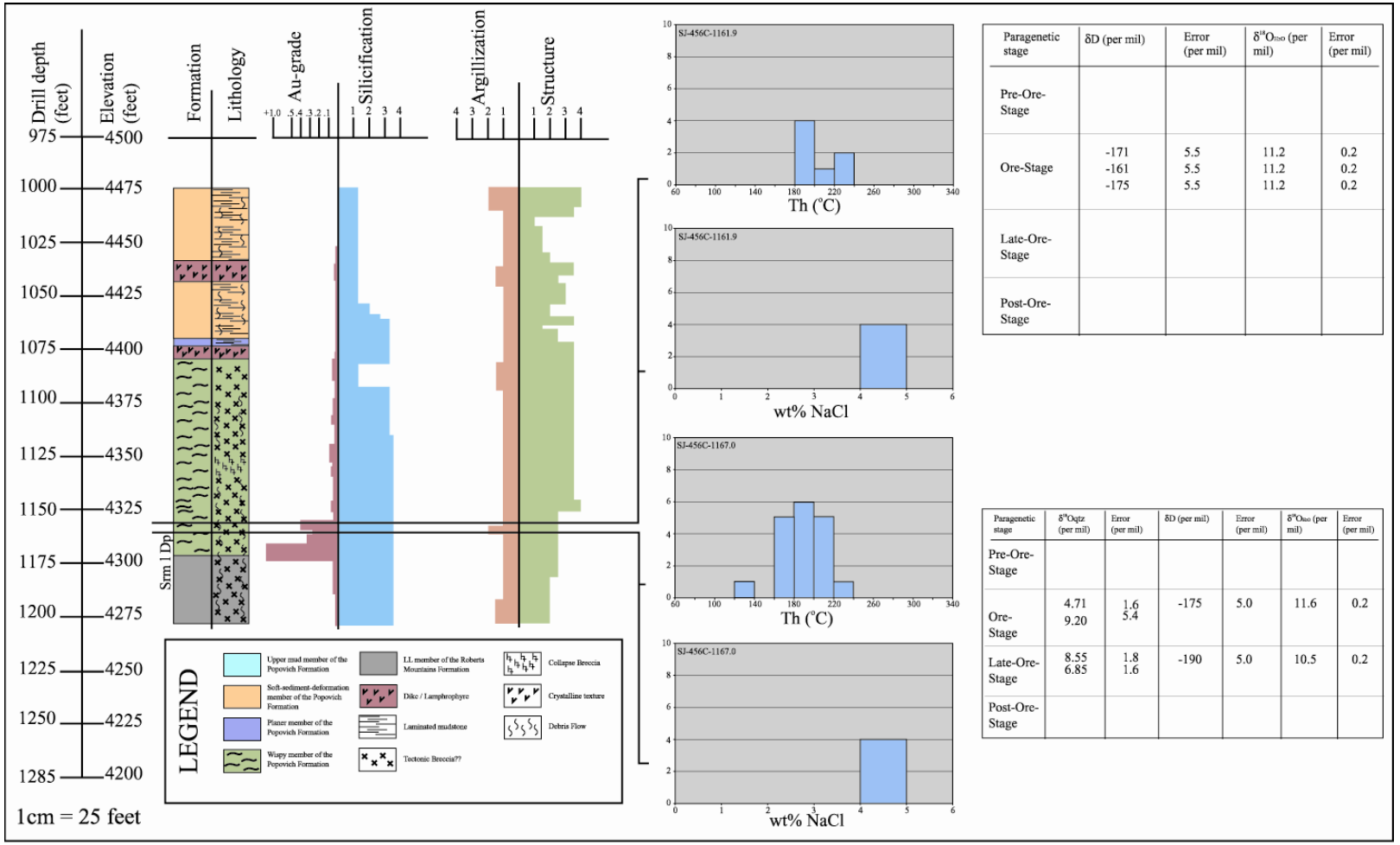

Paragenetic stage	δD (per mil)	Error (per mil)	$\delta^{18}O_{fluid}$ (per mil)	Error (per mil)
Pre-Ore-Stage				
Ore-Stage	-171 -161 -175	5.5 5.5 5.5	11.2 11.2 11.2	0.2 0.2 0.2
Late-Ore-Stage				
Post-Ore-Stage				

Paragenetic stage	$\delta^{18}O_{qtz}$ (per mil)	Error (per mil)	δD (per mil)	Error (per mil)	$\delta^{18}O_{fluid}$ (per mil)	Error (per mil)
Pre-Ore-Stage						
Ore-Stage	4.71 9.20	1.6 5.4	-175	5.0	11.6	0.2
Late-Ore-Stage	8.55 6.85	1.8 1.6	-190	5.0	10.5	0.2
Post-Ore-Stage						

Figure 28. Geologic profile of drill hole SJ-456C at North Betze with chemical analyses. Au-grade in 5 foot assays from Barrick Goldstrike. Silicification is the abundance of both replacement and open-space quartz present, argillization is abundance of clay present, and structure indicates the degree of fracturing (a value of 1 is low indicating a sparse presence while a value of 4 is high indicating a pervasive presence).

relationship between elevated Au concentration, silicification, and magmatism responsible for these cross-cutting igneous bodies is identified; thus these igneous bodies are interpreted as forming prior to ore fluid migration and Au-deposition.

High Au-grade and high silica zones at Betze and North Betze are primarily hosted within silicified brecciated areas. Replacement and open-space silica spatially and genetically related to Au is more abundant at Betze and North Betze than the other ore zones at Betze-Post. Several hypotheses may explain why Betze and North Betze possess more quartz than the other ore zones. First, the abundance of the quartz could either have been governed by abundant open space produced by hydrothermal alteration of the original host rock to form breccias, or original diagenetic breccias providing permeability and allowing fluids to migrate, alter wall-rocks, dissolve carbonate, and precipitate more quartz. Second, hotter fluids were present at Betze and North Betze and these fluids transported more silica than cooler fluids. Third, hotter fluids underwent greater cooling than cooler fluids precipitating more quartz. Fourth, greater cooling dissolved higher amounts of CO_2 at Betze and North Betze creating more porosity and permeability. Fifth, increased porosity and permeability resulted in a greater influx of meteoric water resulting in more efficient cooling of the system leading to greater precipitation of quartz at Betze and North Betze (Emsbo et al., 2003).

Screamer hosts several sample transects with elevated Au spatially associated with strong silicification (Figure 29). Hand samples from Screamer typically exhibit abundant jasperoid and moderate open-space quartz. All four jasperoid types are identified at Screamer and are intergrown with one another. Furthermore, a strong occurrence of silica replaced fossil clasts (Q10c) is present at Screamer. Screamer samples can host

coarse drusy quartz (Q1), intra-clast drusy quartz (Q2), and intra-matrix drusy quartz (Q3); however, most open space quartz is finer-grained than drusy quartz at Betze and North Betze. Post-ore-stage quartz is present at Screamer and crystals display moderately intense luminescence.

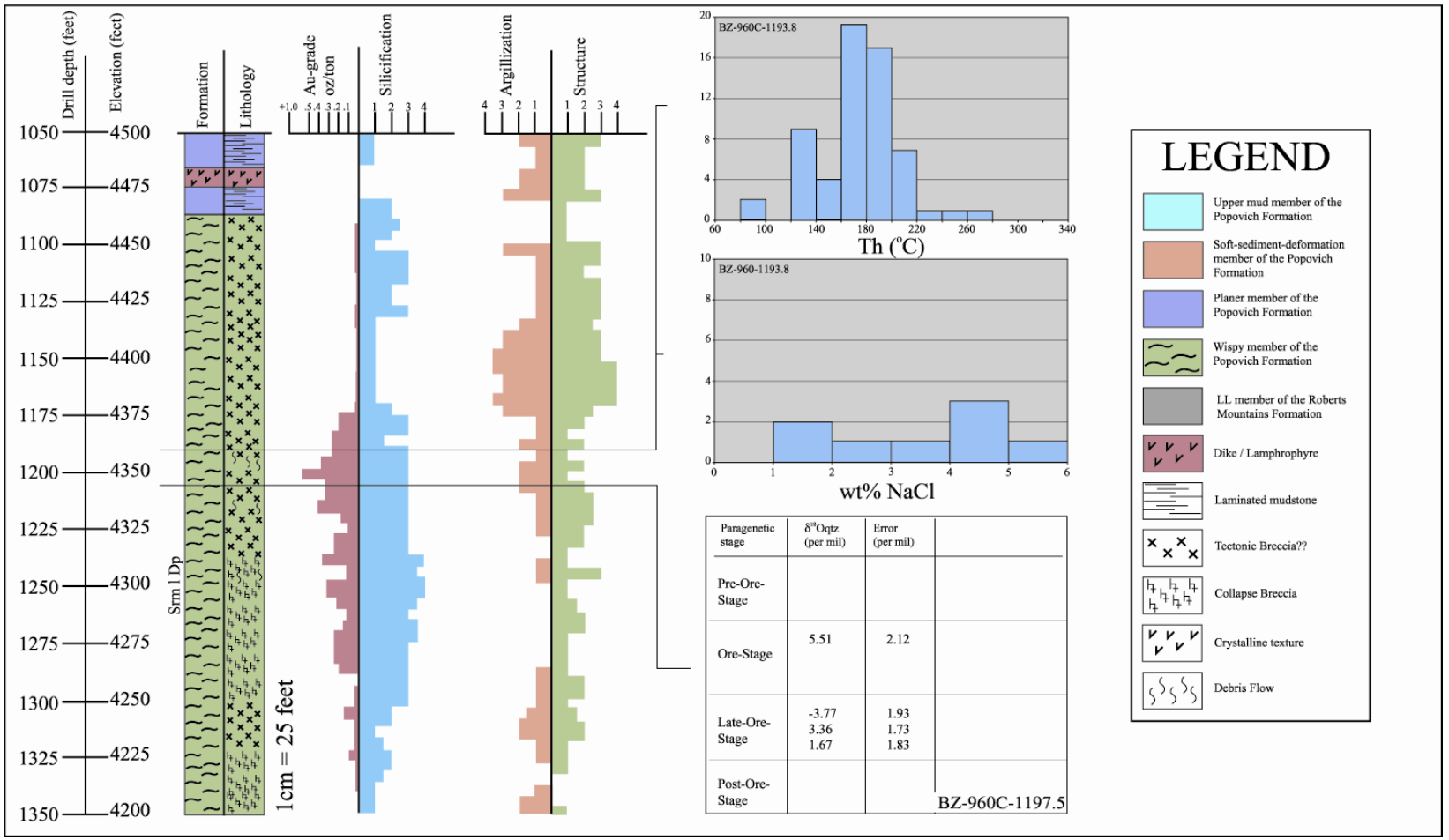

Figure 29. Geologic profile of drill hole BZ-960C at the boundary between Betze and Screamer with chemical analyses. Au-grade in 5 foot assays from Barrick Goldstrike. Silicification is the abundance of both replacement and open-space quartz present, argillization is abundance of clay present, and structure indicates the degree of fracturing (a value of 1 is low indicating a sparse presence while a value of 4 is high indicating a pervasive presence).

CHAPTER 6

GEOCHEMISTRY

Trace element concentrations were determined using electron microprobe analysis (EMPA) of individual mineral grains. EMPA was conducted on quartz and pyrite to identify distinctive chemical signatures in different generations of these minerals. Selected ore stage pyrites were analyzed using LA-ICP-MS to confirm elevated concentrations of Au and other trace elements typically associated with the Carlin-type mineralization event.

Quartz Geochemistry

Wavelength dispersive spectrometer (WDS) analysis of quartz crystals was conducted to determine whether or not chemical zoning caused luminescence. Detection limits for these analyses averaged 0.01 wt % (100 ppm). Preliminary WDS analyses of quartz collected from North Betze indicated ~0.05 wt% (500 ppm) higher Al concentrations in CL-dark ore and late-ore-stage quartz generations relative to CL-bright and CL-multiple quartz generations. These preliminary analyses also analyzed trace concentrations of As, Fe, S, Si, Ti, Sb, Au, Zn, Pb, and Mg; however, only Sb and Al were measured above detection limits. The majority of this suite of elements including Al, Fe, Ti, Zn, Pb, and Mg were selected for analyses based on their behavior as potential CL-activators in

quartz (Figure 30). Analyses were conducted on all quartz generations and included two samples from North Betze and a single sample collected from the Betze-Post pit along the Post Fault. Figure 30 displays average concentrations of these elements measured in CL-dark ore and late-ore-stage quartz versus CL-bright and CL-multiple post-ore-stage quartz. Results from analyses on all quartz generations show Al to be the most abundant trace element and to have higher concentrations in ore-stage and late-ore-stage quartz. These observations suggest that Al may have the strongest influence over the luminosity of different quartz generations. Higher Al concentrations in certain quartz generations provide higher potential for luminescence quenching. Assuming Al atoms are replacing Si and quenching the luminescence of quartz, higher Al quartz would display CL-dark luminescence.

Al concentrations average ~0.43 wt% (4300 ppm) in ore and late-ore-stage quartz generations whereas an average Al concentration of ~0.08 wt% (800 ppm) was measured in post-ore-stage quartz generations. Analyses also determined that Fe, Mg, Zn, Pb, and Ti average below 0.02 wt% (< 200 ppm) in all quartz generations. These elements may be present at levels above the detection limits of the instrument, but do not exhibit concentrations that correlate with the luminescence of different quartz generations.

To further characterize Al concentrations in different quartz generations Al element maps were generated. These maps display relative Al concentrations in a sample containing all generations of the quartz paragenesis. These maps illustrate the correlations between elevated Al and CL-dark quartz, and lower Al concentrations and CL-bright/CL-multiple quartz (Figure 31).

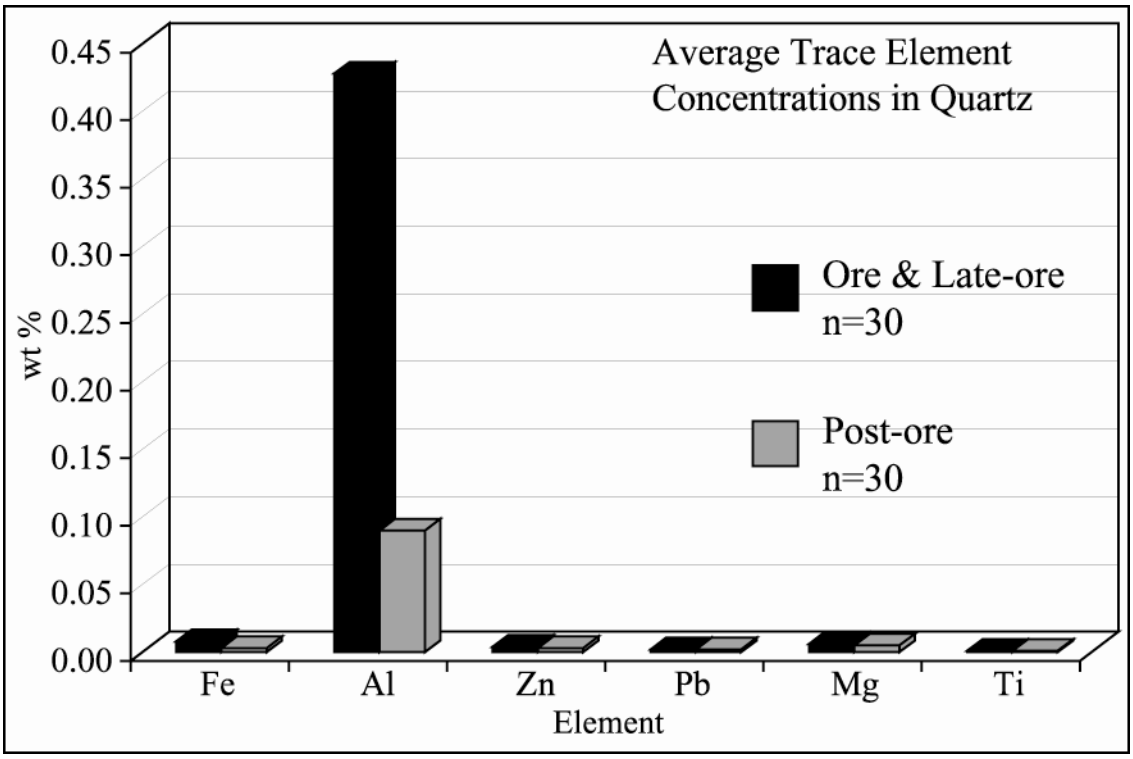

Figure 30. Average concentrations of potential CL-activator elements in quartz. Concentrations measured using Wavelength Dispersive Spectrometry (WDS) on an electron microprobe.

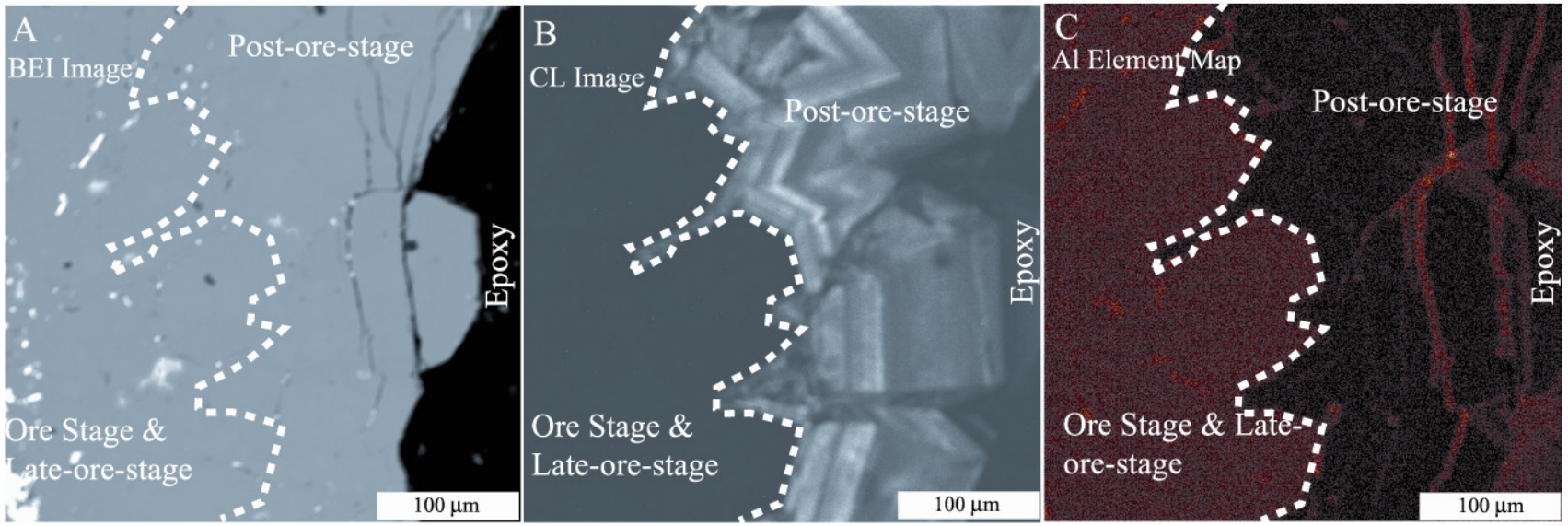

Figure 31. BEI image (A) and CL image (B) illustrating ore stage jasperoid overgrown by late-ore-stage drusy quartz overgrown by post-ore-stage drusy quartz. C) Al map illustrating relative Al concentration. Red areas indicate higher Al zones while darker areas represent lower Al zones. Note the direct correlation between CL-dark quartz and higher Al.

Pyrite Geochemistry

LA-ICP-MS was conducted on ore stage pyrite grains to confirm elevated levels of Au in these grains as well as trace concentrations of typical trace elements linked with Carlin-type gold deposition. LA-ICP-MS analysis quantified a single isotope for selected elements and a high count indicate an elevated presence of that particular element. LA-ICP-MS analysis was conducted on two different ore stage pyrite grains hosted within CL-dark ore stage jasperoid at North Betze. Analyzed grains exhibit ore stage textures that include narrow ore-stage pyrite rims overgrowing a pre-ore-stage pyrite core and a fine-grained massive pyrite rim overgrowing multiple pre-ore-stage pyrite cores. Analyses of these pyrites confirmed high Au concentrations within these grains (Figure 26). Furthermore, LA-ICP-MS analysis of these two grains identified the presence of As, Sb, Te, Al, Hg, Zn, Pb, Cu, Ag, Se, Tl, and Ca (Figure 32).

Discussion of Quartz and Pyrite Geochemistry

The variance in Al concentration in different stages of quartz identified at Betze-Post suggests that Al governs the relative luminosity between different quartz generations. Higher Al concentrations are present within ore and late-ore-stage quartz generations relative to post-ore-stage quartz generations. Higher Al in ore stage quartz indicates Al mobility during the ore stage, which is consistent with the presence of kaolinite as a common ore stage alteration mineral in Carlin-type deposits as well as the presence of trace Al in ore stage pyrite seen at the Betze-Post and Getchell deposits (C. Henkelman and J.S. Cline, Personal Communication, 2003).

LA-ICP-MS analyses of petrographically defined ore-stage pyrite grains confirmed elevated concentrations of Au in some pyrites. Furthermore, these pyrite grains are trace-element rich, which also is a defining characteristic for ore stage pyrite in Carlin-type systems.

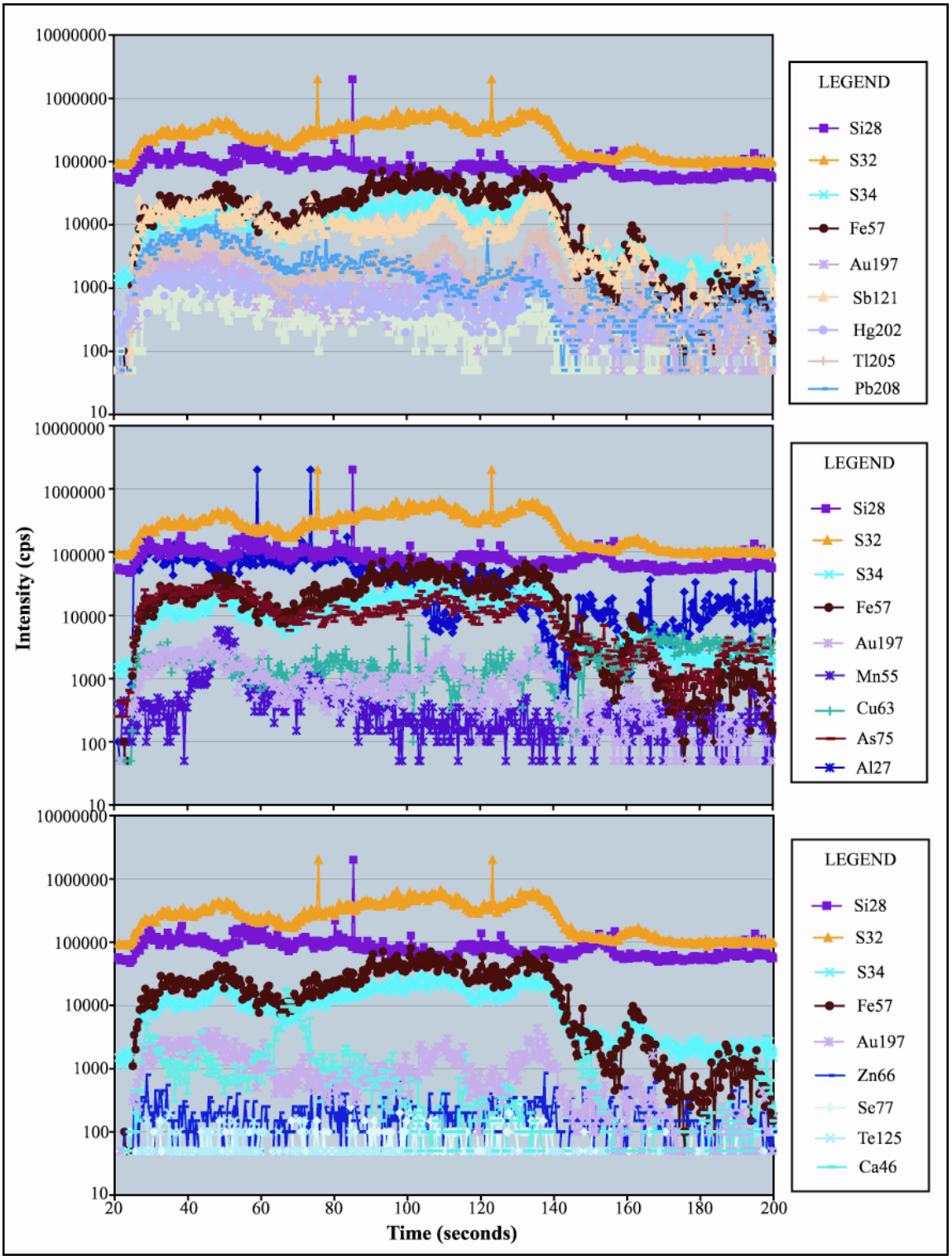

Figure 32. LA-ICP-MS data plot of analysis conducted on a single ore stage pyrite grain. Profiles illustrate the presence of distinct isotopes and indicate the relative abundance of individual isotopes.

CHAPTER 7

FLUID INCLUSION STUDY

Fluid inclusion assemblages were identified in several quartz types. Generally, assemblages contained two-phased fluid inclusions with a vapor phase volume of approximately 5 volume percent. The majority of fluid inclusions are in ore stage jasperoid quartz (Q10 quartz types); however, a small number of inclusions were identified and evaluated in pre-ore-stage quartz (Q7) and late-ore-stage, intra-vug drusy quartz (Q1a). Euhedral drusy quartz crystals and quartz veins contained sparse two-phase fluid inclusion assemblages; however, these inclusions were too small for microthermometry.

Fluid inclusion assemblages were identified and classified by their appearance at 25°C. Four types of fluid inclusions distinguished by origin were identified across the Betze-Post deposit. Primary, unknown$_A$, and secondary fluid inclusions form fluid inclusion assemblages while unknown$_S$ inclusions occur as isolated inclusions. Primary fluid inclusions occur along or within distinct growth zones in individual quartz crystals (Figure 33a). These inclusions are sparse, display consistent liquid to vapor ratios of approximately 5 volume percent, have diameters of 8 μm or less, and always occur within assemblages. Primary fluid inclusion assemblages are present in ore stage jasperoid from North Post and North Betze.

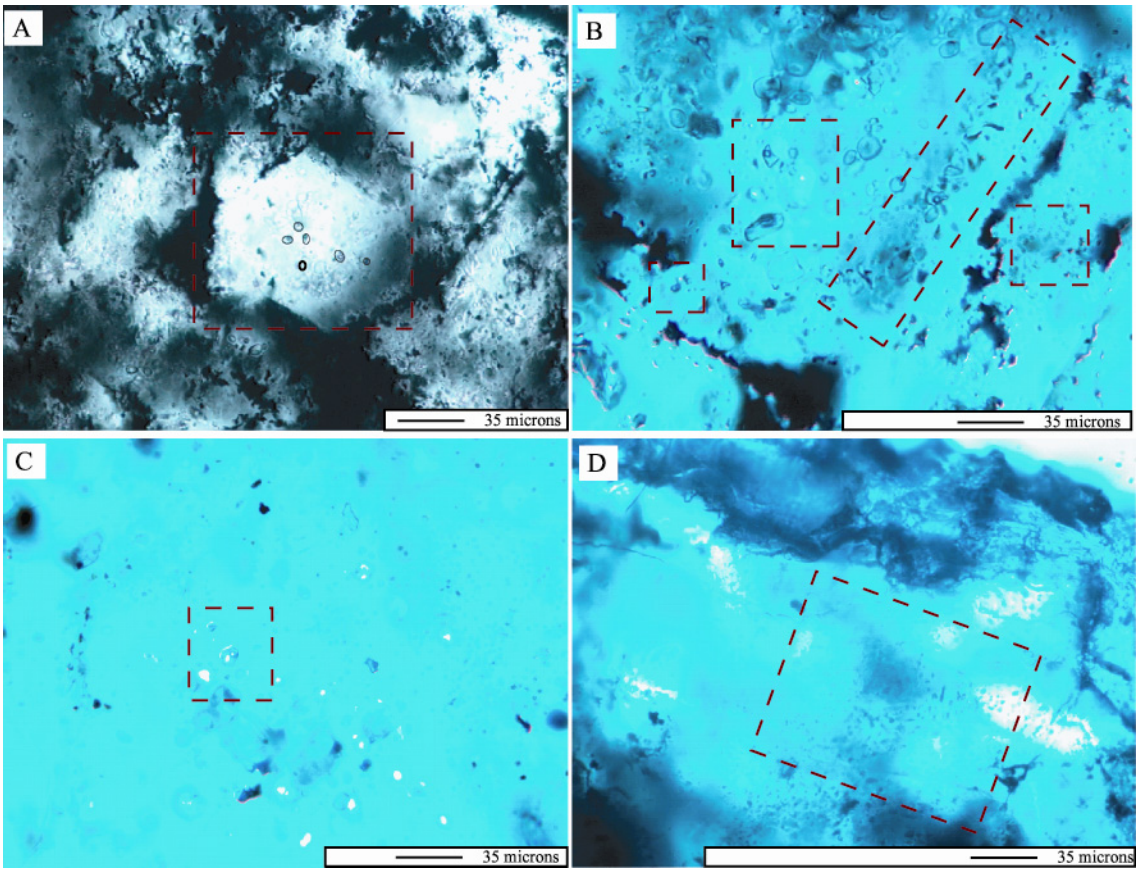

Figure 33. A) Primary fluid inclusion assemblage in ore stage jasperoid quartz. Inclusions are localized within an individual growth zone. B) $Unknown_A$ fluid inclusion assemblage in ore stage jasperoid quartz. Inclusions are distributed across individual quartz crystals. C) $Unknown_S$ fluid inclusions in ore stage jasperoid quartz. Inclusions occur as isolated inclusions within individual quartz crystals. D) Secondary fluid inclusion assemblage in ore stage jasperoid quartz. Inclusions occur along secondary fractures within different quartz crystals. Inclusion assemblages are highlighted within red dashed boxes.

Unknown$_A$ assemblages include inclusions that are not readily identifiable as primary fluid inclusions because these assemblages do not occur in clearly define growth zones. The most distinguishing feature of unknown$_A$ inclusion assemblages is their presence along multiple planes within individual crystals. Unknown$_A$ fluid inclusion assemblages occur in ore stage jasperoid from North Post, Betze, North Betze, and Screamer.

Unknown$_S$ fluid inclusions are isolated two-phase fluid inclusions that have liquid to vapor ratios similar to other fluid inclusion types and are similar in size (Figure 33c). It is difficult to constrain the origin of these inclusions because they are isolated; however, they are large enough for microthermometric analyses. Unknown$_S$ fluid inclusions were identified in ore-stage jasperoid from North Post, Betze, and North Betze.

Secondary fluid inclusion assemblages are sparse and occur along fractures in individual quartz crystals (Figure 33d). The majority of these inclusions is less than 3µm in diameter, too small for microthermometric analyses; however, microthermometry was conducted on several inclusions. Secondary fluid inclusion assemblages were identified in late-ore-stage, intra-vug drusy quartz (Q1a) from North Betze and pre-ore-stage quartz (Q7) from North Betze and Screamer.

Microthermometric Data

Microthermometry was conducted on all four groups of fluid inclusions identified in quartz, and all two-phase fluid inclusions homogenized to vapor. Microthermometric analysis was conducted on 10 samples from 7 drill holes located at North Post, Betze, North Betze, and Screamer.

Homogenization temperatures of 34 primary fluid inclusions range between 135°C and 275°C with a mode of 160°C to 220°C. Homogenization temperatures of 108 $unknown_A$ fluid inclusions range between 75°C and 275°C with a mode of 160°C to 200°C (Figure 34a). Homogenization temperatures of 5 $unknown_S$ fluid inclusions range between 85°C and 295°C with a mode of 180°C to 200°C, while 4 secondary fluid inclusions yield homogenization temperatures between 195°C and 275°C (Figure 34a).

Calculated salinities (wt% NaCl equivalent) range between 3.87 wt% and 5.30 wt% based on analysis of 12 primary inclusions, between 1.74 wt% and 5.41wt% based on analysis of 22 $unknown_A$ inclusions, and between 4.18 wt% and 4.80 wt% based on analysis of 4 secondary inclusions (Figure 34b). A single ice melting temperature measured on an $unknown_S$ inclusion yields a calculated salinity of 4.34 wt% NaCl equivalent (Figure 34b).

Homogenization and ice melting temperatures were also evaluated according to ore zones within the Betze-Post deposit (Figures 34c, 34d). Homogenization temperatures and ice melting temperatures were obtained from ore stage quartz collected from North Betze, Betze, North Post, and Screamer. No fluid inclusions were identified in ore stage quartz from Deep Post. The abundance of nonbrecciated ore-stage jasperoid (Q10d) at Deep Post and the finer-grained nature of this jasperoid type may be responsible for the lack of visible ore-stage fluid inclusions.

Homogenization temperatures of inclusions in quartz from North Betze range between 135°C and 275°C with a mode of 160°C to 220°C for 32 primary inclusions, 75°C and 265°C with a mode of 160°C to 220°C for 23 $unknown_A$ inclusions, and 105°C and 255°C with a mode of 160°C to 220°C for 15 secondary inclusions. Two $unknown_S$

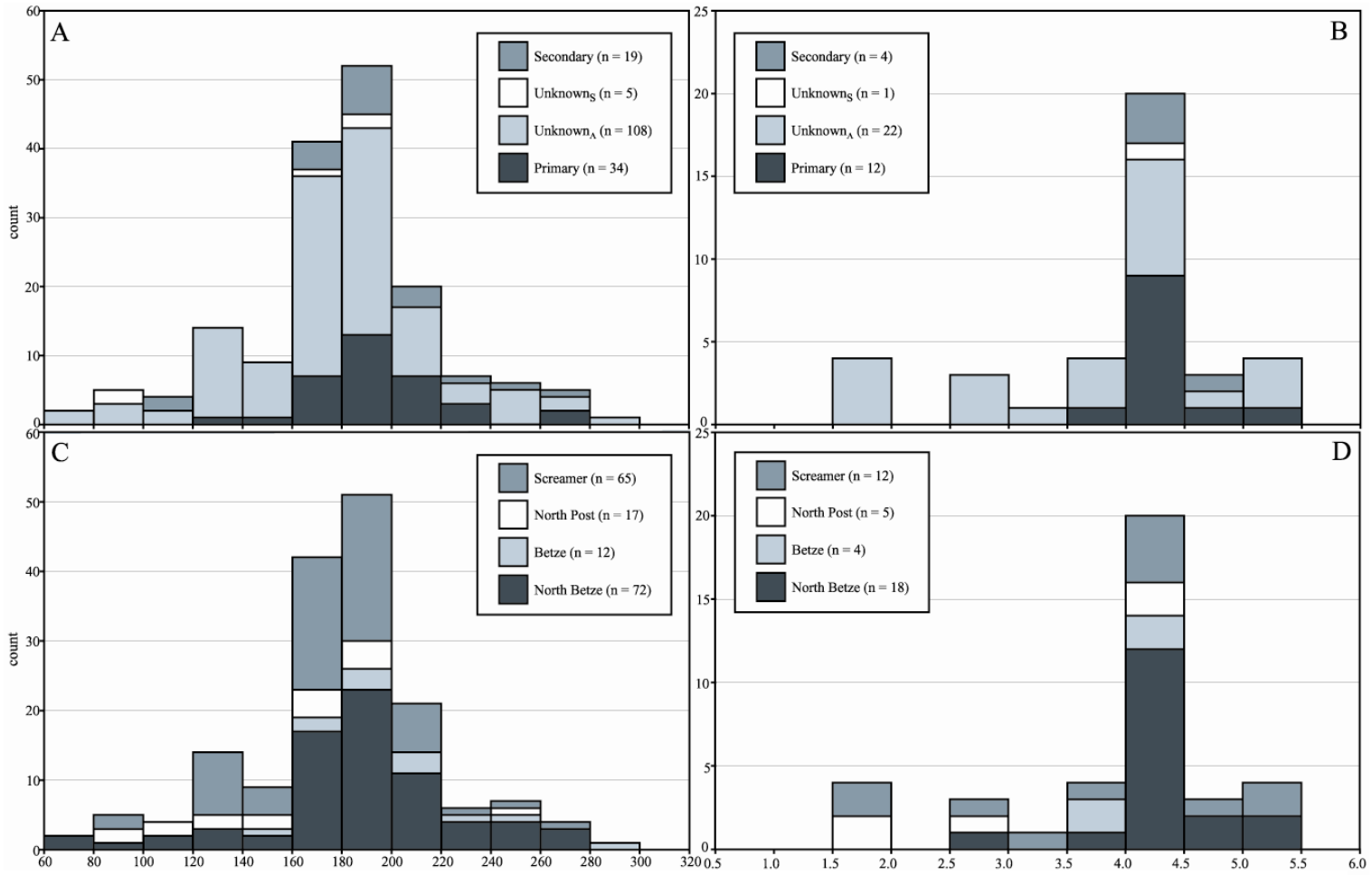

Figure 34. Microthermometric data collected from ore stage fluid inclusions at Betze-Post. A) Homogenization temperatures measured in different fluid inclusion assemblages at Betze-Post. B) Salinities measured in fluid inclusion assemblages. C) Homogenization temperatures measured in ore stage fluid inclusions across different ore zones. D) Salinities measured in ore stage fluid inclusions across different ore zones.

inclusions at North Betze have homogenization temperatures of 175°C and 195°C (Figure 34c). Several fluid inclusions in quartz from North Betze homogenize at temperatures greater than the mode for other Betze-Post ore zones. Inclusion salinities (wt% NaCl equivalent) range between 3.87 wt% and 5.30 wt% for primary inclusions, 2.90 wt% and 5.40 wt% for $unknown_A$ inclusions, and 4.18 wt% and 4.80 wt% for secondary inclusions (Figure 34d).

Homogenization temperatures of inclusions in quartz from Betze range between 155°C and 285°C with a mode 160°C to 220°C for 11 $unknown_A$ inclusions while a homogenization temperature of 195°C was measured in a single $unknown_S$ inclusion (Figure 34c). Inclusion salinities (wt% NaCl equivalent) range between 3.87 wt% and 4.03 wt% for $unknown_A$ inclusions with a single salinity of 4.34 wt% measured in an individual $unknown_S$ inclusion (Figure 34d).

Two primary fluid inclusions in ore stage quartz from North Post have homogenization temperatures of 155°C and 175°C while the analysis of 13 $unknown_A$ inclusions in ore stage quartz from North Post have homogenization temperatures between 115°C and 245°C with a mode of 160°C to 200°C. Finally, two $unknown_S$ fluid inclusions from North Post have homogenization temperatures of 85°C (Figure 34c). Salinities of inclusions in quartz from North Post (wt% NaCl equivalent) range between 1.74 wt% and 4.34 wt% for $unknown_A$ inclusions (Figure 34d).

Homogenization temperatures of inclusions in quartz from Screamer range between 85°C and 265°C with a mode of 140°C to 220°C for 61 $unknown_A$ inclusions and 165°C and 205°C for four secondary inclusions (Figure 34c). Salinities of inclusions in quartz

from Screamer (wt% NaCl equivalent) range between 1.74 wt% and 5.41 wt% for $unknown_A$ inclusions (Figure 34d).

Discussion of Microthermometry Data

Analyzed ore-stage fluid inclusions from all ore zones show consistent ranges of salinities and homogenization temperatures (Fig 25 – 29) across the Betze-Post deposit. This consistency suggests that all evaluated ore-stage fluid inclusions at Betze-Post were trapped during the same hydrothermal event. The similarities between homogenization temperatures measured in secondary fluid inclusions in pre-ore-stage quartz (Q7) and primary and $unknown_A$ fluid inclusions in ore-stage jasperoid (Q10 quartz types) suggest that the two groups of inclusions probably trapped the same hydrothermal fluid.

Even with the consistency of microthermometric data, subtle variations in homogenization temperature exist across Betze-Post. A considerable number of fluid inclusions (15) in ore stage quartz at North Betze have homogenization temperatures higher than 220°C, the upper end of the temperature mode for the Betze-Post deposit (Figure 34). Betze, North Betze, and Screamer have a small number of inclusions in ore stage quartz with homogenization temperatures above 220°C. A small number of higher homogenization temperatures for inclusions commonly indicates that a few inclusions leaked, and vapor bubbles expanded. However, a larger number of inclusions with elevated homogenization temperatures in ore stage quartz at North Betze could indicate that North Betze is located above a feeder for the Betze-Post deposit and recorded hotter ore fluids relative to North Post, Betze, and Screamer.

According to the spatial relationships between homogenization temperature, salinity, Au-grade, and degree of silicification illustrated by figures 25 through 29, little fluctuation in homogenization temperature and salinity occurs across zones with differing Au-grade. Consistent homogenization temperatures and salinities were also measured across zones with differing degrees of silicification. Furthermore, analyzed inclusions that are proximal to cross-cutting igneous dikes do not show a distinct difference in homogenization temperature or salinity relative to inclusions not proximal to these bodies (Figures 25, 26). The lack of homogenization or salinity fluctuation in the vicinity of these dikes may suggest no relationship to the Carlin hydrothermal event at Betze-Post. These observations also support the possibility that all of the analyzed inclusions were trapped during the same hydrothermal event and that the ore fluid at Betze-Post maintained a relatively constant temperature and salinity.

The microthermometric data collected at Betze-Post show consistencies with microthermometry data sets collected from other Carlin-type gold deposits of Nevada (Figure 35). Betze-Post homogenization temperatures and salinities are similar to data measured at Getchell (Cline and Hofstra, 2000), Meikle (Lamb, 1995), Jerritt Canyon (Hofstra, 1994), Turquoise Ridge (Shigehiro, 1999), and Carlin (Radtke, 1980; Kuehn, 1989).

As fluid inclusion data for Betze-Post are very similar to data for other Carlin-type gold deposits, it is likely that the fluids are chemically similar, and ore fluids are aqueous, and most likely contained 2 to 4 mole% CO_2. A single-phase fluid with 2 to 4 mole% CO_2 and temperatures between 160°C and 220°C is stable at minimum pressures of approximately 330 to 650 bars (See Figure 22, Hofstra and Cline, 2000). Pressures of

330 to 650 bars indicate formation at minimum depths of 1.2 to 2.4 km assuming lithostatic pressures (Hofstra and Cline, 2000). At these conditions a temperature correction of 20°C is indicated resulting in a trapping temperature range of 180°C to 240°C for inclusion fluids in ore stage quartz at Betze-Post.

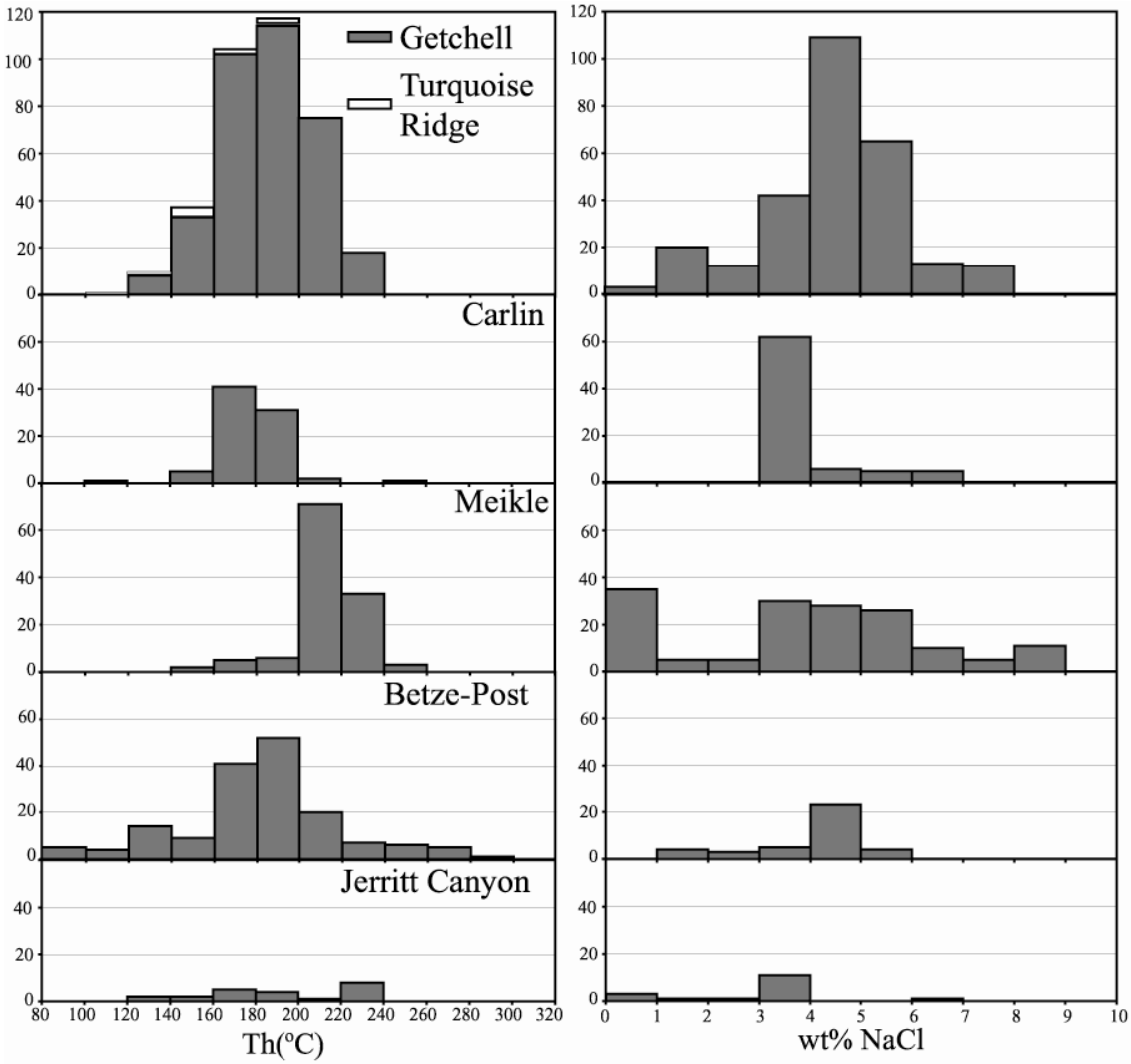

Figure 35. Summary of fluid inclusion homogenization temperatures (Th) and salinities (wt% NaCl equivalent) for Carlin-type gold deposits. Data from Hofstra, 1994 (Jerritt Canyon), Lamb, 1995 (Meikle), Radtke, 1980 and Kuehn, 1989 (Carlin), Cline and Hofstra, 2000 (Getchell), and Shigehiro, 1999 (Turquoise Ridge).

CHAPTER 8

STABLE ISOTOPE STUDY

Stable isotopes have become an integral part of ore deposit research. The study of light stable isotopes can provide information about the diverse origins of ore fluids, temperatures of mineralization, and physiochemical conditions of mineral deposition. Oxygen and hydrogen isotopic signatures were measured on quartz and fluid inclusions in quartz, respectively. Oxygen isotopes of quartz were measured using both in situ secondary ion mass spectrometry (SIMS) and conventional bulk analyses. This study marks the first in which an in-situ technique measured oxygen isotopes in quartz associated with Carlin-type gold mineralization.

$\delta^{18}O_{QTZ}$ and δD_{H2O} Signatures

The goals for conducting in-situ SIMS oxygen isotope analysis of quartz were three fold. First, different generations of quartz may have unique $\delta^{18}O$ values that can be used as a fingerprint for distinguishing quartz grains and refining the quartz paragenesis. Second, previous oxygen isotope studies of quartz in Carlin-type gold deposits have used bulk analyses, which may not provide an accurate signature of the Carlin event. Third, $\delta^{18}O$ values combined with δD values can indicate sources for fluids that precipitated different generations of quartz, and which transported and precipitated gold.

To identify sources and exchange histories of water in hydrothermal fluids trapped in inclusions, the hydrogen isotope value of inclusions fluids (δD_{H2O}) and the oxygen isotope value of its quartz host ($\delta^{18}O_{QTZ}$) were determined. δD_{H2O} analyses were conducted on inclusion fluids in quartz samples collected from North Betze drill holes and along the Post Fault in the Betze-Post open pit. Separates from three samples of ore stage jasperoid from North Betze were analyzed and a total of seven δD_{H2O} and $\delta^{18}O_{QTZ}$ measurements were conducted. A fourth sample containing a mixture of ore stage jasperoid and late-ore-stage drusy quartz from North Betze was also analyzed. All of these samples were from zones of high Au, high silica, low argillization, and little fracturing within the host rock (Figures 26 & 28). Four splits of a single sample of post-ore-stage drusy quartz collected along the Post Fault in the Betze-Post open pit were also analyzed.

In-situ $\delta^{18}O$ values were obtained from quartz in 16 samples from 9 drill holes (Table 2). Analysis points were selected based on petrographic characteristics and CL-zoning (Figure 36). Pre-ore quartz has $\delta^{18}O$ values between 17.76‰ and 19.26‰ based on 3 analyses at North Betze. CL-dark ore stage quartz has $\delta^{18}O$ values between -0.19‰ and 25.30‰ based on 30 analyses. CL-dark late-ore-stage quartz has $\delta^{18}O$ values between 1.67‰ and 14.48‰ based on 17 analyses. CL-bright and CL-multiple post-ore-stage quartz has $\delta^{18}O$ values between -21.60‰ and 12.72‰ based on 23 analyses (Table 2) (Figure 37).

Analyses conducted on quartz from Deep Post were from zones with high Au, moderate silicification, low argillization, and low fracturing. Six analyses on ore stage

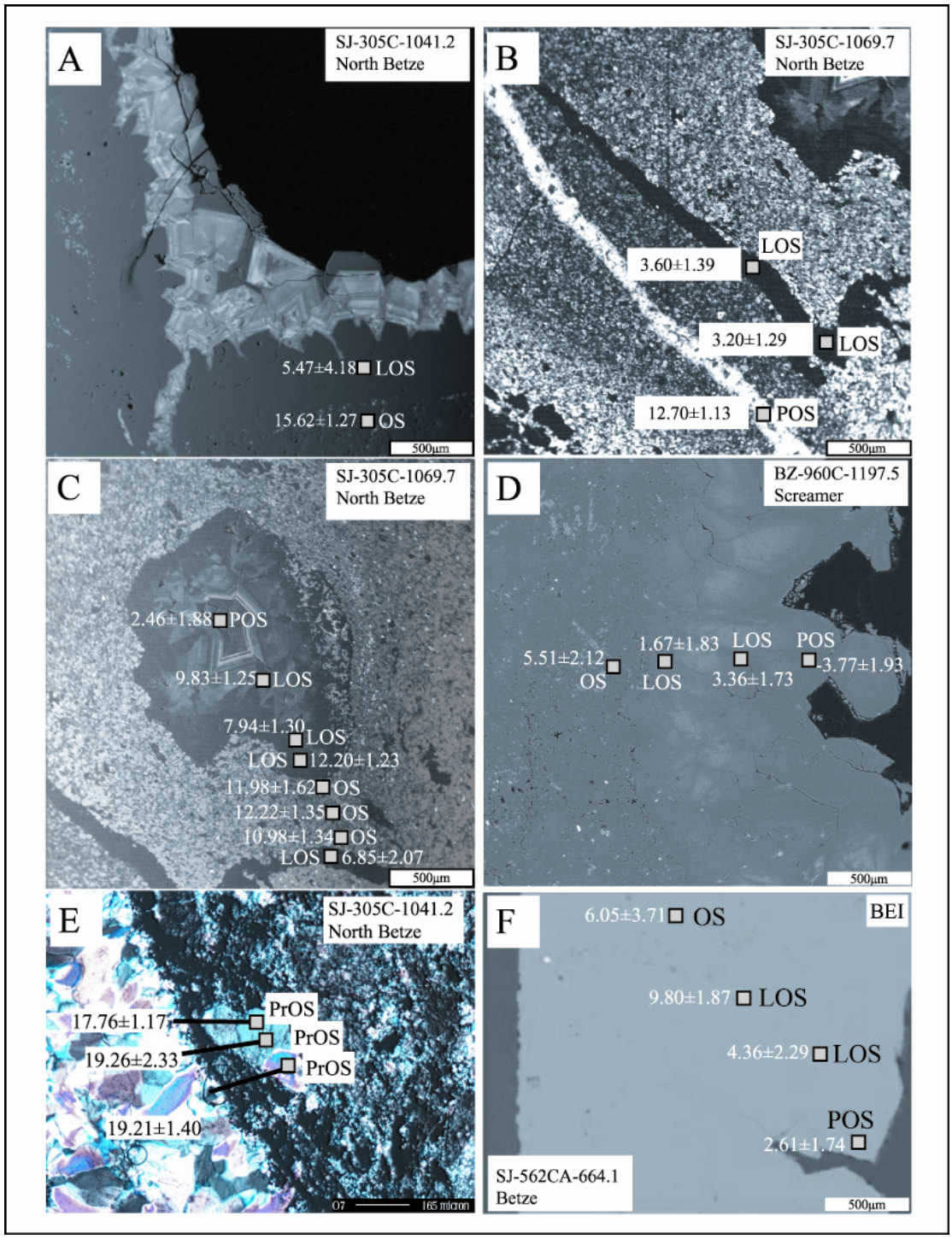

Figure 36. Locations of in situ SIMS $\delta^{18}O$ analyses conducted on quartz. Analyses were conducted on pre-ore-stage (PrOS) inherited quartz (E), ore stage (OS) jasperoid (A, C, D, and F), late-ore-stage (LOS) drusy quartz (A, C, D and F), late-ore-stage quartz veins (B and C), and post-ore-stage (POS) drusy quartz (B, C, D, and F). Each point lists the $\delta^{18}O$ value along with the measured error.

Table 2. SIMS $\delta^{18}O$ values measured in pre-ore, ore stage, late-ore-stage, and post-ore-stage quartz. Per mil values relative to Vienna standard mean ocean water (VSMOW)

Sample	Ore zone	Mineral	$\delta^{18}O_{QTZ}$ (‰)*	Error (‰)	$\delta^{18}O_{H2O}$[1] (‰)
Pre-ore-stage					
SJ-305C-1041.2	North Betze	quartz	19.26	2.33	
SJ-305C-1041.2	North Betze	quartz	17.74	1.17	
SJ-305C-1041.2	North Betze	quartz	19.21	1.40	
Ore Stage					
RM97-2C-633.0	Deep Post	jasperoid	24.11	1.38	12.11
RM97-2C-633.0	Deep Post	jasperoid	2.26	1.36	-9.74
P-175C-1245.0	Deep Post	jasperoid	23.96	1.33	11.96
P-175C-1245.0	Deep Post	jasperoid	24.01	1.13	12.01
RM97-2C-488.0	Deep Post	jasperoid	25.30	1.56	13.30
RM97-9C-315.6	Deep Post	jasperoid	20.90	1.28	8.90
SJ-562CA-664.1	Betze	jasperoid	9.80	1.87	-2.20
SJ-562CA-664.1	Betze	jasperoid	6.05	3.71	-5.95
SJ-305C-1041.2	North Betze	jasperoid	15.62	1.27	3.62
SJ-305C-1069.7	North Betze	jasperoid	11.98	1.62	-0.02
SJ-305C-1069.7	North Betze	jasperoid	12.22	1.35	0.22
SJ-305C-1069.7	North Betze	jasperoid	10.98	1.34	-1.02
SJ-457C-1052.5	North Betze	jasperoid	3.80	1.23	-8.20
SJ-457C-1052.5	North Betze	jasperoid	13.27	1.17	1.27
SJ-457C-1052.5	North Betze	jasperoid	15.92	1.35	3.92
SJ-457C-1052.5	North Betze	jasperoid	2.55	1.54	-9.45
SJ-457C-1052.5	North Betze	jasperoid	-0.19	1.45	-12.19
SJ-456C-1167.0	North Betze	jasperoid	4.71	1.66	-7.29
SJ-456C-1167.0	North Betze	jasperoid	9.20	5.46	-2.80
SJ-263C-1042.1	North Betze	jasperoid	18.97	3.18	6.97
SJ-457C-1052.0	North Betze	jasperoid	23.71	1.39	11.71
SJ-457C-1052.0	North Betze	jasperoid	4.21	1.42	-7.79
SJ-457C-1052.0	North Betze	jasperoid	8.05	1.36	-3.95
SJ-457C-1052.0	North Betze	jasperoid	8.70	1.56	-3.30
SJ-263C-1051.0	North Betze	jasperoid	13.09	1.51	1.09
SJ-457C-1026.0	North Betze	jasperoid	8.85	1.11	-3.15
SJ-457C-1026.0	North Betze	jasperoid	10.79	3.01	-1.21
BZ-960C-1197.5	Screamer	jasperoid	5.51	2.12	-6.49
BZ-915C-1073.1	Screamer	jasperoid	24.56	1.85	12.56
BZ-915C-1073.1	Screamer	jasperoid	9.15	1.13	-2.85

* Measured $\delta^{18}O$ signature of quartz using in-situ secondary ion mass spectrometry (SIMS) analysis.

[1] Calculated $\delta^{18}O$ signature of ore stage fluids in equilibrium with quartz (Matsuhisa et. al., 1979) at 200°C, from fluid inclusion temperatures.

Table 2. Continued.

Sample	Ore zone	Mineral	$\delta^{18}O_{QTZ}$ (‰)*	Error (‰)	$\delta^{18}O_{H2O}$ [1] (‰)
Late-ore-stage					
P-175C-1312.0	Deep Post	drusy quartz	14.48	1.62	2.48
P-175C-1312.0	Deep Post	drusy quartz	6.20	2.02	-5.80
SJ-562CA-664.1	Betze	drusy quartz	4.36	2.29	-7.64
SJ-305C-1041.2	North Betze	drusy quartz	5.47	4.18	-6.53
SJ-305C-1069.7	North Betze	drusy quartz	7.94	1.30	-4.06
SJ-305C-1069.7	North Betze	drusy quartz	3.20	1.29	-8.80
SJ-305C-1069.7	North Betze	drusy quartz	3.60	1.39	-8.40
SJ-305C-1069.7	North Betze	drusy quartz	12.19	2.00	0.19
SJ-305C-1069.7	North Betze	drusy quartz	6.85	2.07	-5.15
SJ-305C-1069.7	North Betze	drusy quartz	11.98	1.42	-0.02
SJ-305C-1069.7	North Betze	drusy quartz	9.83	1.25	-2.17
SJ-456C-1167.0	North Betze	drusy quartz	8.55	1.86	-3.45
SJ-456C-1167.0	North Betze	drusy quartz	6.85	1.62	-5.15
SJ-457C-1101.8	North Betze	drusy quartz	12.09	2.32	0.09
SJ-457C-1101.8	North Betze	drusy quartz	12.14	2.05	0.14
BZ-960C-1197.5	Screamer	drusy quartz	3.36	1.73	-8.64
BZ-960C-1197.5	Screamer	drusy quartz	1.67	1.83	-10.33
Post-ore-stage					
SJ-475C-150.0	Betze	drusy quartz	3.21	1.61	
SJ-475C-150.0	Betze	drusy quartz	-0.03	2.07	
SJ-475C-150.0	Betze	drusy quartz	3.01	2.13	
SJ-475C-150.0	Betze	drusy quartz	1.17	1.93	
SJ-475C-150.0	Betze	drusy quartz	-0.83	2.52	
SJ-475C-150.0	Betze	drusy quartz	1.77	2.00	
SJ-475C-150.0	Betze	drusy quartz	2.76	2.15	
SJ-475C-150.0	Betze	drusy quartz	-0.08	2.02	
SJ-475C-150.0	Betze	drusy quartz	0.22	1.83	
SJ-475C-150.0	Betze	drusy quartz	1.67	2.52	
SJ-475C-150.0	Betze	drusy quartz	1.82	1.82	
SJ-475C-150.0	Betze	drusy quartz	5.16	2.34	
SJ-475C-150.0	Betze	drusy quartz	5.96	1.73	
SJ-475C-150.0	Betze	drusy quartz	6.01	1.75	
SJ-562CA-664.1	Betze	drusy quartz	2.61	1.74	
SJ-305C-1041.2	North Betze	drusy quartz	9.22	1.55	
SJ-305C-1041.2	North Betze	drusy quartz	10.21	1.67	
SJ-305C-1041.2	North Betze	drusy quartz	10.48	1.31	
SJ-305C-1069.7	North Betze	drusy quartz	12.72	1.13	
SJ-305C-1069.7	North Betze	drusy quartz	2.46	1.88	
BZ-960C-1197.5	Screamer	drusy quartz	-3.77	1.93	

* Measured $\delta^{18}O$ signature of quartz using in-situ secondary ion mass spectrometry (SIMS) analysis.

[1] Calculated $\delta^{18}O$ signature of ore stage fluids in equilibrium with quartz (Matsuhisa et. al., 1979) at 200°C, from fluid inclusion temperatures.

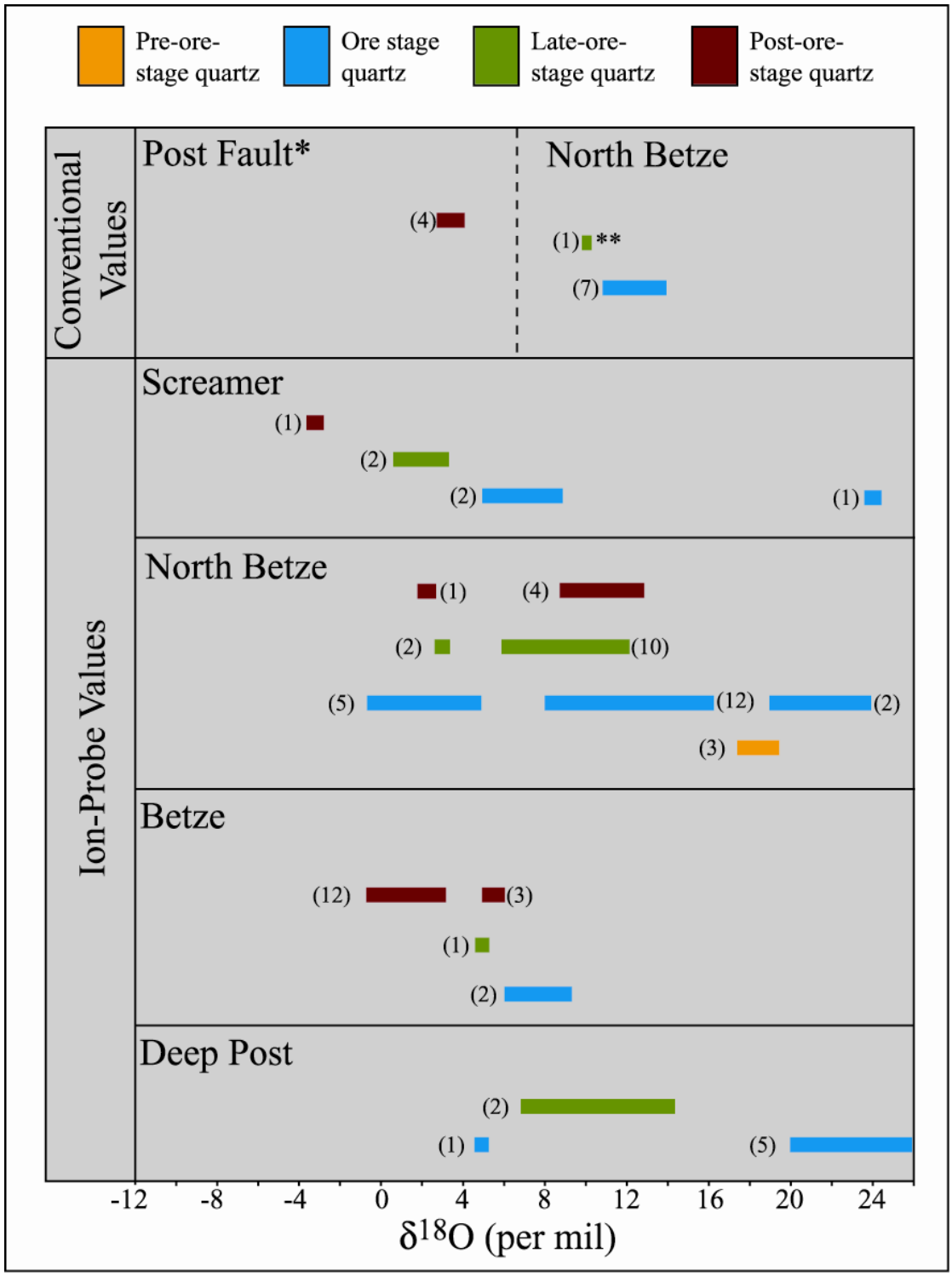

Figure 37. $\delta^{18}O$ values measured in quartz at Betze-Post using SIMS and conventional methods. Bars indicate range of values; (12) indicates number of analyses. Values in per mil relative to Vienna standard mean ocean water (VSMOW). * Sample collected from the Betze-Post open pit along the Post Fault. ** Sample contains mixture of ore stage jasperoid and late-ore-stage drusy quartz.

jasperoid quantified $\delta^{18}O$ values between 2.26‰ and 25.30‰, and two analyses of late-ore-stage drusy quartz have $\delta^{18}O$ values of 6.20‰ and 14.48‰ (Table 2) (Figure 37). Pre-ore-stage and post-ore-stage quartz generations were not identified at Deep Post.

Analyses conducted on quartz from the Betze ore zones analyzed zones with high Au, high silica, low argillization, and moderate to high fracturing. Two analyses on ore-stage quartz at Betze have $\delta^{18}O$ values of 6.05‰ and 9.80‰, a single analysis of late-ore-stage drusy quartz has an $\delta^{18}O$ value of 4.36‰, and 14 analyses of post-ore-stage drusy quartz have $\delta^{18}O$ values between -0.83‰ and 6.01‰ (Table 2) (Figure 37).

The majority of analyses from North Betze were localized within zones of high Au, high silica, low argillization, and little fracturing within the host rock (Figures 26 & 28). Pre-ore-stage quartz from North Betze has $\delta^{18}O$ values between 17.76‰ and 19.26‰, while 19 analyses of ore-stage jasperoid have $\delta^{18}O$ values between -0.19‰ to 23.71‰. Twelve analyses of late-ore-stage quartz have $\delta^{18}O$ values between 3.20‰ and 12.19‰, and 5 analyses of post-ore-stage quartz from North Betze have $\delta^{18}O$ values between 2.46‰ and 15.92‰ (Table 2) (Figure 37).

Analyses at Screamer were localized within a high Au ore zone with high silica, low argillization, and moderate fracturing within the host rock (Figure 29). Three analyses conducted on ore stage jasperoid from Screamer have $\delta^{18}O$ values of 5.51‰, 9.15‰, and 24.56‰, two analyses of late-ore-stage quartz have $\delta^{18}O$ values of 1.67‰ and 3.36‰, and a single analysis of post-ore-stage quartz at Screamer has a $\delta^{18}O$ value of -3.77‰ (Table 2) (Figure 37).

The $\delta^{18}O$ signature of H_2O in ore stage fluids, interpreted to be in equilibrium with quartz, was calculated (Matsuhisa et al., 1979) based on fluid inclusion data. Using a

temperature of 200°C, a fractionation factor of 12‰ was calculated. The calculation indicates that H_2O in ore stage fluids had $\delta^{18}O$ values between -12.19‰ and 13.30‰ (Tables 2 & 3) (Figure 38).

Table 3 lists the δD_{H2O} and $\delta^{18}O_{QTZ}$ values measured in each sample of quartz analyzed. The bulk inclusion fluid in ore stage jasperoid yields δD_{H2O} signatures between -175‰ and -107‰ with an average error of ±5‰. The quartz hosts for these fluid inclusions have $\delta^{18}O_{QTZ}$ values between 11.20‰ and 13.80‰ with an average error of ±0.2‰ based on seven analyses. The bulk inclusion fluid from the mixture of ore-stage jasperoid and late-ore-stage drusy quartz has a δD_{H2O} value of -190 ±5‰ and the quartz that hosts these fluid inclusions has $\delta^{18}O_{QTZ}$ value of 10.50‰ ±0.20‰. Finally, the bulk inclusion fluid in post-ore-stage drusy quartz has δD_{H2O} values between -184‰ and -163‰ with an average error of ±5‰ and the quartz host for these inclusions has $\delta^{18}O_{QTZ}$ values between 3.40‰ and 4.80‰ with an average error of ±0.20‰.

Discussion of Ion-probe and Conventional $\delta^{18}O$ Data

The SIMS $\delta^{18}O$ values determined for quartz have a large range for each quartz stage excepting pre-ore-stage quartz. Pre-ore-stage quartz has values within a tight range that is high relative to other stages of quartz; however, only three analyses were conducted.

Oxygen isotope results exhibit a subtle decrease in $\delta^{18}O$ values at each ore zone with time, and an overall decrease from east to west across the Betze-Post deposit (Figures 37 and 39). The majority of $\delta^{18}O$ values of ore stage quartz range from 5.00‰ to 26.00‰,

Table 3. Measured δD values of bulk inclusion fluids in quartz and $\delta^{18}O$ values of quartz containing the inclusions.

Sample	Ore zone	Mineral	δD_{H2O} (‰)**	Error (‰)	$\delta^{18}O_{H2O}$ (‰)***	Error (‰)
Ore stage						
SJ-456C-1167.0	North Betze	jasperoid	-175	5	11.6	0.2
SJ-305C-1041.2	North Betze	jasperoid	-107	5	13.8	0.2
SJ-305C-1041.2	North Betze	jasperoid	-127	5	13.8	0.2
SJ-305C-1041.2	North Betze	jasperoid	-142	5	13.8	0.2
SJ-456C-1161.9	North Betze	jasperoid	-171	5	11.2	0.2
SJ-456C-1161.9	North Betze	jasperoid	-161	5	11.2	0.2
SJ-456C-1161.9	North Betze	jasperoid	-175	5	11.2	0.2
Late-ore-stage						
SJ-456C-1167.0	North Betze	jsp/drusy quartz	-190	5	10.5	0.2
Post-ore-stage						
Pit S1-120	North Betze	drusy quartz	-183	5	4.8	0.2
Pit S1-120	North Betze	drusy quartz	-184	5	4.8	0.2
Pit S1-120	North Betze	drusy quartz	-163	5	3.4	0.2
Pit S1-120	North Betze	drusy quartz	-174	5	3.4	0.2

** Measured delta D signature of inclusion fluids using mass spectrometry

*** Measured $\delta^{18}O$ signature of bulk quartz using conventional methods by Clayton and Mayeda (1963)

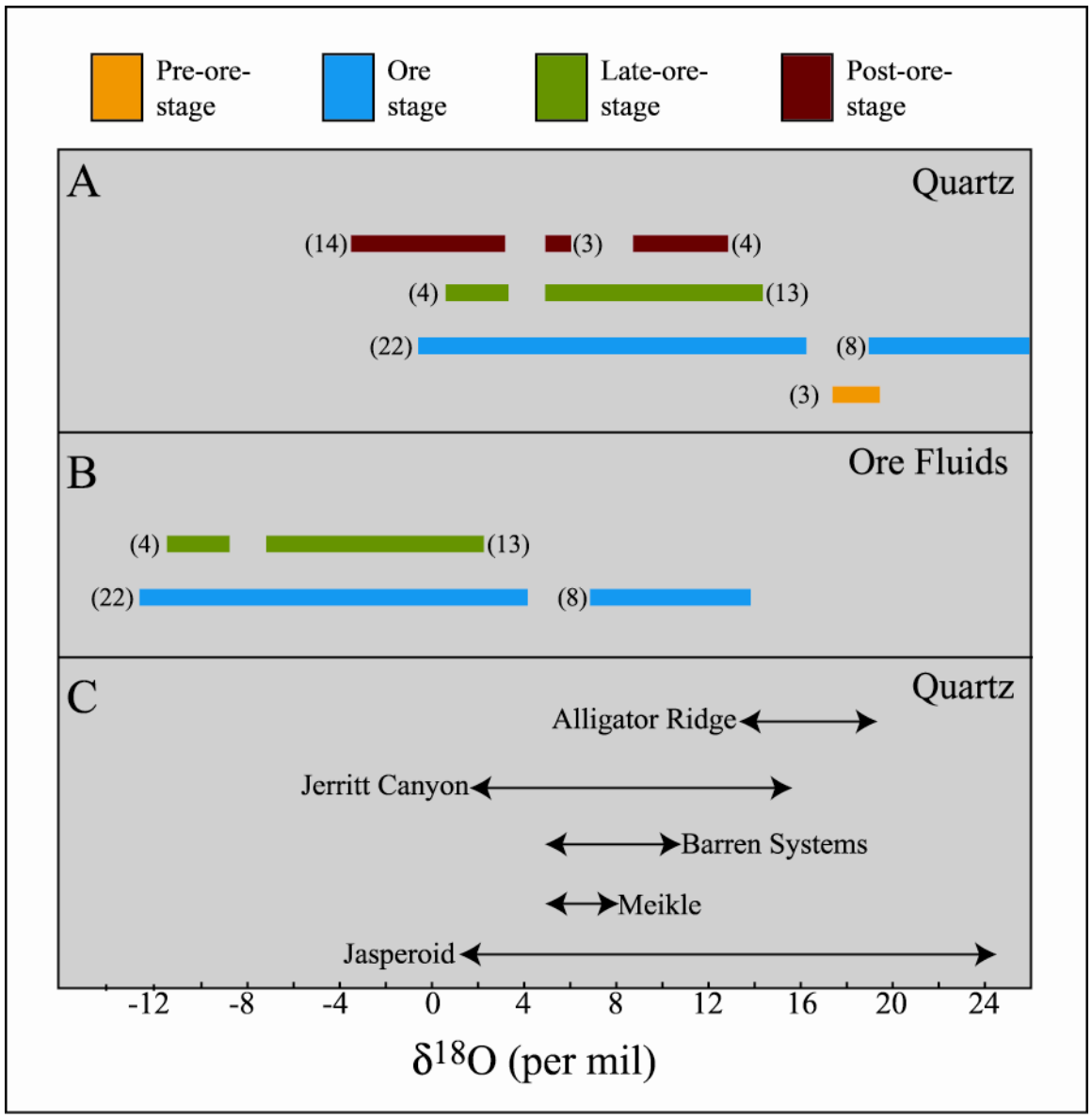

Figure 38. $\delta^{18}O$ values in quartz and in ore fluids in equilibrium with quartz. A) In situ SIMS $\delta^{18}O$ values of quartz from multiple stages. Values in per mil relative to Vienna standard mean ocean water (VSMOW). B) Calculated $\delta^{18}O$ values of ore stage fluids in equilibrium with ore-stage quartz. Calculated using fractionation factor of 12‰ based on fractionation at 200°C (Matsuhisa et al., 1979) from measured fluid inclusion homogenization temperatures. C) $\delta^{18}O$ ranges of quartz at other Carlin-type deposits determined using conventional methods. Sources of data: Holland et al. (1988), Ilchik (1990), Hofstra (1994), Hofstra et al. (1999), and Emsbo (1999).

while the majority of $\delta^{18}O$ values of late-ore-stage quartz range between 0.00‰ and 15.00‰ (Table 2). Post-ore-stage quartz exhibits a continued decrease in $\delta^{18}O$ signatures with most values ranging between -1.00‰ and 6.00‰ (Table 2).

A decrease in isotopic signatures from ore stage quartz to post-ore-stage quartz has been identified within individual ore zones at Betze-Post (Figures 36 and 37). In samples from North Betze, ore stage quartz has higher $\delta^{18}O$ values than late-ore-stage quartz, which has $\delta^{18}O$ values higher than post-ore-stage quartz (figure 36). Similar $\delta^{18}O$ trends are identified in samples SJ-562CA-664.1 from Betze and BZ-960C-1197.5 from Screamer (Figure 36).

Excepting one outlier analysis, Deep Post, which is located along the Post Fault at the eastern edge of the system, exhibits the highest range of $\delta^{18}O$ values measured in ore (20.90‰ – 25.30‰) and late-ore-stage quartz (6.20‰ – 14.48‰) (Table 2, Figure 37). Betze and North Betze, located along the JB Series Faults at the center of the Betze-Post deposit, exhibit a small number of $\delta^{18}O$ values similar to values at Deep Post; however, most of the $\delta^{18}O$ values from ore (5.00‰ – 15.92‰) and late-ore-stage quartz (5.47‰ – 12.19‰) fall within an intermediate $\delta^{18}O$ range (Table 2, Figure 37). Most delta ^{18}O values of ore (5.51‰ – 9.15‰) and late-ore stage quartz (1.67‰ – 3.36‰) at Screamer, located proximal to the Shalosky Fault along the western edge of the system, include the lowest $\delta^{18}O$ values measured at Betze-Post (Table 2, Figure 37).

Delta ^{18}O signatures collected from quartz using conventional methods also demonstrate a decrease from ore stage quartz to post-ore-stage quartz. Ore stage quartz has $\delta^{18}O$ values between 11.2‰ and 13.8‰, a mixture of ore stage quartz and late-ore-stage quartz has a $\delta^{18}O$ value of 10.5‰, and post-ore-stage quartz has $\delta^{18}O$ values from

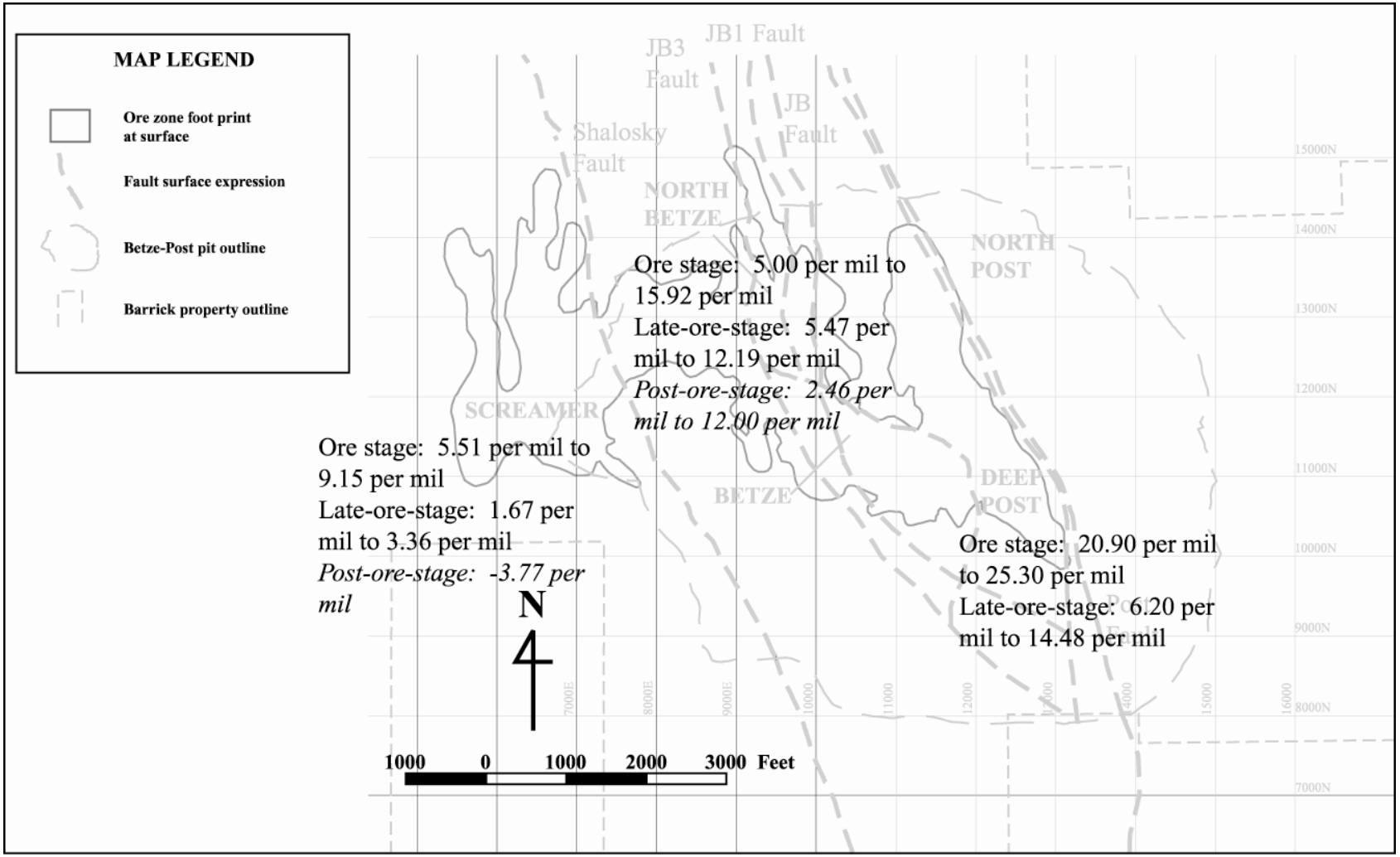

Figure 39. Spatial $\delta^{18}O$ trend for ore, late-ore, and post-ore quartz across the Betze-Post deposit. Most $\delta^{18}O$ values decrease from east to west suggesting that dilution of the ore fluid by an unevolved meteoric fluid increased from east to west.

3.4‰ to 4.8‰ (Table 3). These results are consistent with results determined by SIMS analysis.

The range of in-situ ion probe $\delta^{18}O$ values of ore stage quartz from Betze-Post show similarities to $\delta^{18}O$ values of ore stage quartz using conventional methods from other Carlin-type deposits (Figure 38a and 38c). Betze-Post shows a similar but wider range of $\delta^{18}O$ signatures than the $\delta^{18}O$ ranges for ore stage quartz at Alligator Ridge, Jerritt Canyon, and Meikle (Figure 38). The similarity between in-situ isotope values and values derived from bulk analyses of quartz indicates that the $\delta^{18}O$ values of ore-stage quartz in Carlin-type deposits do have a large range; however, isotopic signatures show spatial relationships, probably reflecting increasing fluid/rock reaction along differing fluid pathways and with distance from structures. Consequently, $\delta^{18}O$ analysis of quartz may be used as a tool to characterize different ore zones in Carlin-type gold deposits, and provide insight into fluid migration across Carlin-type systems with space and time.

The large range of $\delta^{18}O$ values determined for ore-stage and late-ore-stage quartz at Betze-Post and possible outlier analyses for some ore zones is difficult to explain. Possible causes may include the analysis of foreign material in individual quartz crystals, varying degrees of fluid/rock exchange, temperature variations, fluid salinity, fluid boiling, and/or lack of paragenetic control.

The isotopic signature of ore stage jasperoid quartz could be contaminated by inherited materials commonly identified in jasperoid. Inherited sources of oxygen that may be present in jasperoid include calcite and dolomite. These minerals consist largely of oxygen and may contribute to the $\delta^{18}O$ values of ore stage jasperoid. Even with the spatial resolution of the in situ SIMS technique (~15 μm), fine grains of calcite and/or

dolomite may be analyzed along with quartz producing a mixed $\delta^{18}O$ value. Fine-grained solid calcite inclusions are commonly present in all jasperoid types at Betze-Post; however, dolomite was not present in ore stage jasperoid and was only identified as being overgrown by late-ore-stage drusy quartz types. Furthermore, solid calcite inclusions are very fine-grained and were not likely present in enough mass to significantly contribute to the $\delta^{18}O$ values of ore stage jasperoid.

Fluid/rock exchange can produce a large range in $\delta^{18}O$ signatures. Factors that affect the isotopic exchange between ore fluids and the host rock through which it travels include relative abundance of fluid versus rock and the composition of the country rock. In fluid-buffered systems, a high fluid/rock ratio allows the isotopic signature of the fluid to dominate the isotopic signature of minerals precipitated from that fluid. In rock-buffered systems, high rock/fluid ratios allow the isotopic signature of the rock to dominate the isotopic signature of minerals precipitated from a fluid. The wide range in $\delta^{18}O$ values of quartz at Betze-Post may reflect differing fluid/rock ratios and variations in fluid flux with time across the deposit.

The carbonate host rock in Carlin-type deposits contains oxygen that is liberated when the limestone is decarbonatized and may contribute to the oxygen isotopic composition of minerals precipitating from fluids that pass through these rocks. Typically carbonate rocks possess high $\delta^{18}O$ values relative to $\delta^{18}O$ values for igneous and metamorphic rocks (Hoefs, 1997). Reaction between ore fluids and limestone, resulting in the liberation of oxygen from limestone may contribute to the higher $\delta^{18}O$ values measured in ore stage quartz.

The influence of fluid temperature, salinity, and fluid boiling at Betze-Post is most likely small compared to that of fluid/rock exchange or variance caused by fluid migration. The fractionation of oxygen isotopes is inversely related to temperature and greater fractionation will occur at lower temperature (Hoefs, 1997). The presence of ionic salts in a solution changes the local structure of water around dissolved ions, thus altering the isotopic ratios (Hoefs, 1997). However, fluid inclusion microthermometry clearly indicates that temperature and salinity of the ore fluid remained relatively constant across all ore zones and petrographic and fluid inclusion analysis has not identified any textural evidence for boiling in ore stage quartz.

Paragenetic uncertainty and $\delta^{18}O$ fluctuation introduced by the various factors described may have produced outliers within the collected $\delta^{18}O$ data. By removing these outliers, distinct spatial and temporal trends were identified across Betze-Post and distinguish different ore zones (Table 2, Figure 37). These trends appear to reflect a decreasing oxygen isotopic signature in the ore fluid both with time, and in space from east to west across the deposit.

Discussion of δD_{H2O} Values of Inclusion Fluids

The δD_{H2O} signatures measured in ore stage fluid inclusions at North Betze and along the Post Fault are low and mostly lower than late Eocene meteoric waters (i.e. -120‰ - -160‰) (A. Hofstra, personal communication, 2004). The ratio of hydrogen from fluid inclusion water versus hydrogen from occult sites in samples, proportions of hydrogen from these sites, presence of fluid inclusions generated by the recrystallization of an opalline silica precursor, presence of intercrystalline organic matter or glue, or presence

of OH^- bearing clay minerals could all contribute to the low δD values obtained from ore stage inclusion fluids at Betze-Post.

Jasperoid typically contains hydrogen from several sources including fluid inclusion H_2O, gases such as CH_4 and H_2S, OH^- sites in quartz, or inclusions of H-bearing organic matter (Faure, 2003) and the proportions of hydrogen from these sites will regulate the δD signature of a fluid. Abundant gases (CH_4, H_2S) are probably not present within the sampled inclusion fluids since fluid inclusion microthermometry did not identify significant gases. Furthermore, samples were baked over night to remove intercrystalline water before measuring for δD_{H2O} values decreasing the influence of other H-bearing sites in the jasperoid. Petrographic and cathodoluminescence analyses of samples submitted for δD analysis showed no textural evidence of an opalline silica precursor. Clay minerals are OH-bearing minerals and generally have lower δD values than fluid inclusion water, but no clay minerals were identified in analyzed material, and clays probably cannot account for the lower δD values measured in ore stage inclusion fluids. As δD samples were collected from the original hand sample from which the doubly polished thick section was made and were not impregnated with epoxy, organic matter and glue did not contaminate the analyzed samples.

Although there is no obvious reason for the low δD analyses, the results for all samples except samples SJ-305C-1041.2 are problematic. These analyses may reflect additional hydrogen contributed by sites other than fluid inclusions in the jasperoid. Because the error in these analyses cannot be quantified, it is difficult to interpret the results. The values of most analyses below Tertiary meteoric water, and analyses of sample SJ-456C-1167.0 that are consistent with meteoric water, may indicate that

inclusion fluids have a meteoric origin. However, this interpretation should be applied with caution.

Isotopic Constraints on Fluid Evolution

Based on modeling of the measured $\delta^{18}O$ and δD_{H2O} values from quartz and ore fluids, respectively, two end member fluids are inferred. These end members include a fluid with a relatively low $\delta^{18}O$ value of approximately -14‰ and a fluid with a relatively high $\delta^{18}O$ value of approximately 14‰.

Extensive oxygen isotopic exchange between deeply circulating meteoric water and country rock with high $\delta^{18}O$ values could account for the high end of the $\delta^{18}O$ range determined for ore fluids (Rye et al., 1974; Radtke et al., 1980). Carbonate rocks, similar to rocks in the northern Carlin trend, typically have $\delta^{18}O$ values that range between 8‰ and 40‰. High $\delta^{18}O$ values in quartz must have resulted as fluids experienced extensive fluid/rock exchange as fluids migrated within relatively high $\delta^{18}O$ country rocks. Alternatively, unevolved meteoric fluids typically have low $\delta^{18}O$ values and likely comprise the lower $\delta^{18}O$ fluid end member. Quartz with low $\delta^{18}O$ isotopic signatures likely precipitated from ore fluids that were increasingly diluted by unevolved meteoric water. The increasing dilution of the ore fluid toward the west and with time could account for the spatial $\delta^{18}O$ trend that distinguishes the different ore zones at Betze-Post.

As identified by SIMS, large ranges of $\delta^{18}O$ values are documented over small distances in ore stage jasperoid. The presence of these small intervals further confirms that dilution of the ore fluid by shallow meteoric fluids with time took place during the ore stage and continued into the late-ore and post-ore stages at Betze-Post.

The ore fluids may have accessed the site of gold deposition along three families of NW- to SE-trending faults that cross-cut the Betze-Post deposit and include from east to west the Post Fault (Deep Post and North Post), JB Series Faults (Betze and North Betze), and the Shalosky Fault (Screamer). Ore fluids migrating upwards along these structures from depth were increasingly diluted to varying degrees by unevolved meteoric fluids, producing the range of isotopic signatures observed across the Betze-Post deposit.

A plot of $\delta^{18}O$ versus δD signatures aids in interpreting the possible source for fluids that precipitated different quartz generations at Betze-Post (Figure 40). Ore stage fluid inclusion data plot along and below a fluid/rock fractionation curve while late-ore-stage and post-ore-stage fluid inclusion data extend toward the meteoric water line (Figure 40). The actual δD values of fluid inclusion water in ore stage jasperoid samples maybe significantly higher than the shown depending on the proportion of hydrogen derived from fluid inclusion water and additional hydrogen-bearing sites in the analyzed quartz. Three splits of sample SJ-305C-1041.2 have ore stage δD values from -142‰ to -107‰. One of these analyses is outside the range determined for Tertiary meteoric water and extends towards the magmatic and metamorphic water boxes (Figure 40).

Two possible scenarios that have been proposed for other Carlin-type gold deposits and which may have occurred at Betze-Post include mixing between an evolved meteoric ore fluid and an unevolved meteoric fluid, and mixing between a deep magmatic/metamorphic ore fluid and an evolved meteoric fluid. δD signatures measured in fluid inclusions from ore stage jasperoid in this study, though difficult to interpret because of low δD values, suggest that the ore fluids have an evolved meteoric source. Evaluation of $\delta^{18}O$ and δD data from Betze-Post suggests that mixing between a highly

exchanged meteoric fluid and a less evolved meteoric ore fluid produced the high range of $\delta^{18}O$ values similar to that observed at other deposits (Holland et al., 1988; Illchik, 1990; Kuehn and Rose, 1992; Hofstra, 1994; Hofstra and Rye, 1998; Hofstra et al., 1999; and Emsbo et al., 2003) (Figure 38). While results most strongly support mixing of two distinct meteoric fluids, δD values from sample SJ-305C-1041.2 might suggest the presence of a deep magmatic or metamorphic component in the ore fluid.

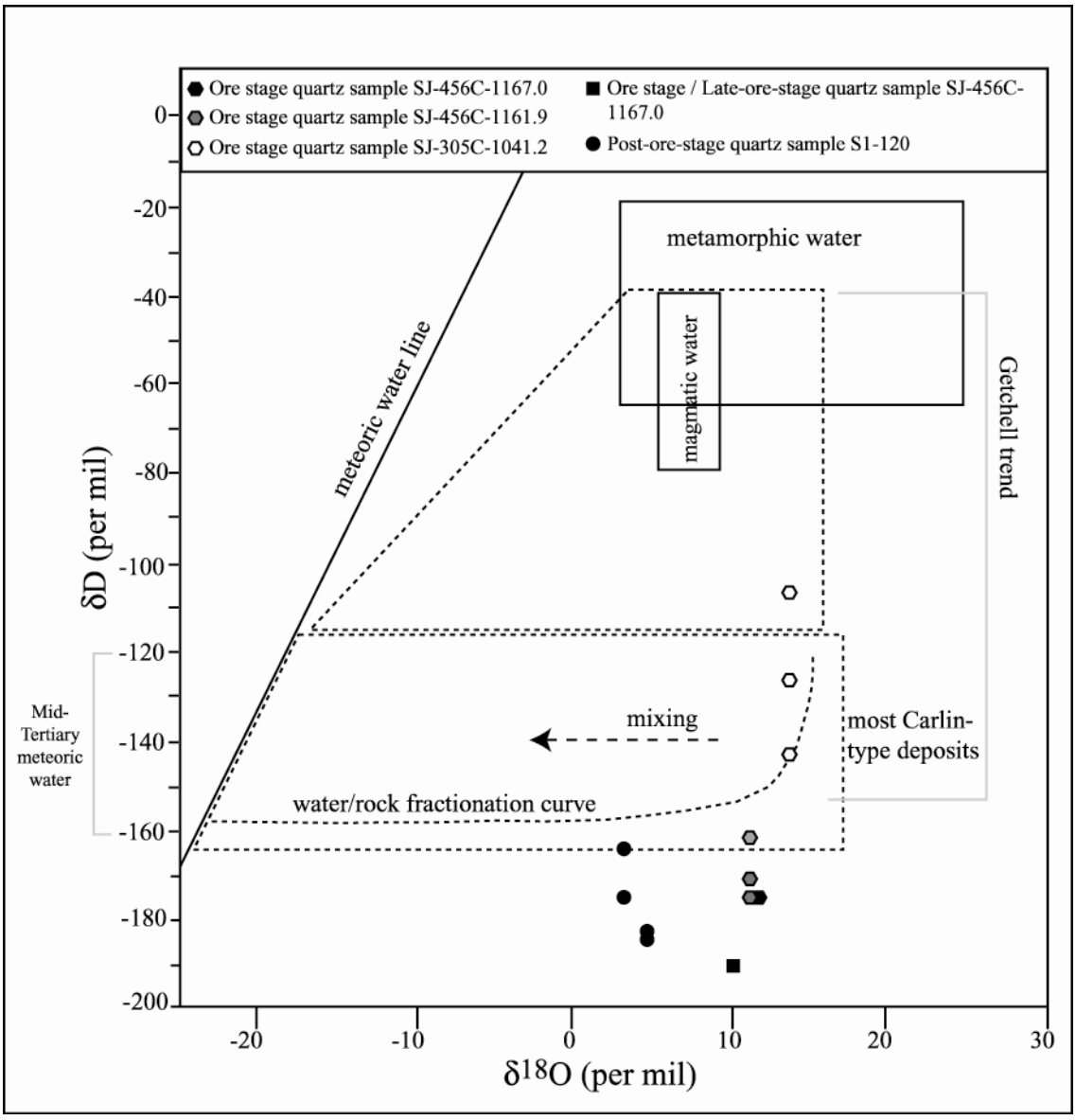

Figure 40. Hydrogen and oxygen isotope plot showing values determined for inclusion fluids in ore stage, late-ore-stage, and post-ore-stage quartz (Modified from Hofstra and Cline, 2000).

CHAPTER 9

DISCUSSION AND CONCLUSIONS

Ore Fluid Characteristics

Ore stage silicification at Betze-Post is manifested as both replacement jasperoid and open-space drusy and vein quartz. The precipitation of these two quartz habits during the main- and late-ore stages of the Carlin event indicates that ore deposition was accompanied by fluid/rock reaction as well as fluid cooling in localized zones.

Ore fluid temperatures and salinities remained constant across Betze-Post with the exception that fluid temperatures at North Betze extended approximately 60° higher than in other ore zones (Figure 34). Salinities show no significant fluctuation across different ore zones. Measured temperatures and salinities at Betze-Post are consistent with temperatures and salinities measured at Getchell (Cline and Hofstra, 2000), Carlin (Radtke, 1980; Kuehn, 1989), Meikle (Lamb, 1995), and Jerritt Canyon (Hofstra, 1994). It is therefore reasonable to conclude that ore fluids at Betze-Post have a composition similar to ore fluids at other Carlin-type gold deposits, which contain minor CO_2 and H_2S (which contributed to apparent salinity), and salinities between 2 and 3 wt% NaCl equivalent.

Stable isotope ratios of quartz suggest that an evolved meteoric ore fluid was increasingly diluted by meteoric water of the same temperature and salinity as gold

deposition occurred at Betze-Post. δD and $\delta^{18}O$ values in ore fluids and quartz suggest that ore fluids were progressively diluted as ore fluids accessed the western part of the deposit, and with time from the ore stage to the late-ore-stage.

Betze-Post Genetic Model

Oxygen and hydrogen isotope ratios of ore stage inclusion fluids indicate that evolved hydrothermal fluids, undergoing different degrees of mixing with unevolved meteoric water and fluid/rock exchange, are responsible for Au deposition at Betze-Post. Fluid inclusion data indicate that the two fluids had similar temperatures and salinities. Similar mixing models involving meteoric fluids have been proposed at Jerritt Canyon (Hofstra et al., 1987; Northrop et al., 1987) and Carlin (Rose and Kuehn, 1987; Kuehn and Rose, 1992; Kuehn and Rose, 1995). According to these models, ascending hydrothermal fluids were swamped by ambient ground water either along system margins, within structures, or during late-system collapse of the hydrothermal system. At the Betze-Post deposit, meteoric dilution increased to the west and over time, as the ore system evolved to the late-ore-stage. Late-ore-stage drusy quartz and vein quartz precipitated and precipitation of ore-bearing pyrite ceased. Finally, the hydrothermal system collapsed, allowing cool, oxygenated meteoric waters to flood and completely dilute the system. Post-ore-stage drusy quartz, vein quartz, calcite, and barite may have precipitated at this time or long after the hydrothermal system ceased.

Ore fluids at Carlin-type gold deposits are interpreted to have migrated upward along high-angle normal faults to sites of Au deposition. These high-angle fluid conduits have been interpreted to extend to mid-crustal levels below the brittle-ductile transition

(Tosdal et al., 2000; Grauch et al., 2003).

The formation of the Betze-Post Carlin-type gold deposit likely involved Au-rich fluids migrating upwards along the Post Fault. The high $\delta^{18}O$ signature identified at Deep Post support the interpretation that the Post Fault is a major ore fluid conduit. Two models illustrate potential end-member pathways for fluid migration across the Betze-Post deposit (Figure 41). Both models include the generation of a hydrothermal plume that expanded outward from the primary fluid conduit during the prograde stages of the hydrothermal event and contracted inward as the hydrothermal system waned and finally collapsed. In both models, highly evolved ore fluids initially displaced the unevolved meteoric groundwater and fluid mixing occurred along the expanding margin of the plume. Eventually, as the ore system waned, the hydrothermal plume collapsed, and local unevolved meteoric water flooded the system and diluted ore fluids.

In the first model (Figure 41a), an evolved ore fluid migrated upwards along the Post Fault. The ore fluids were then diverted into the Wispy unit and ore fluids migrated laterally toward Betze and North Betze, and finally Screamer. As the fluid migrated laterally, reaction between ore fluids and host rocks induced precipitation of gold in trace element-rich pyrite. In this model, the ore fluid underwent increased fluid/rock reaction as it migrated to the west producing lower $\delta^{18}O$ values in ore-stage quartz to the west. As the hydrothermal plume began to contract, the ore fluid was displaced by unevolved meteoric water, initially along the western edge of the system (Screamer). This model may explain the lowest $\delta^{18}O$ values in post-ore-stage quartz at Screamer.

The second model also begins with an evolved ore fluid at Deep Post migrating upwards along the Post Fault; however, in this model fluids migrate upward from depth

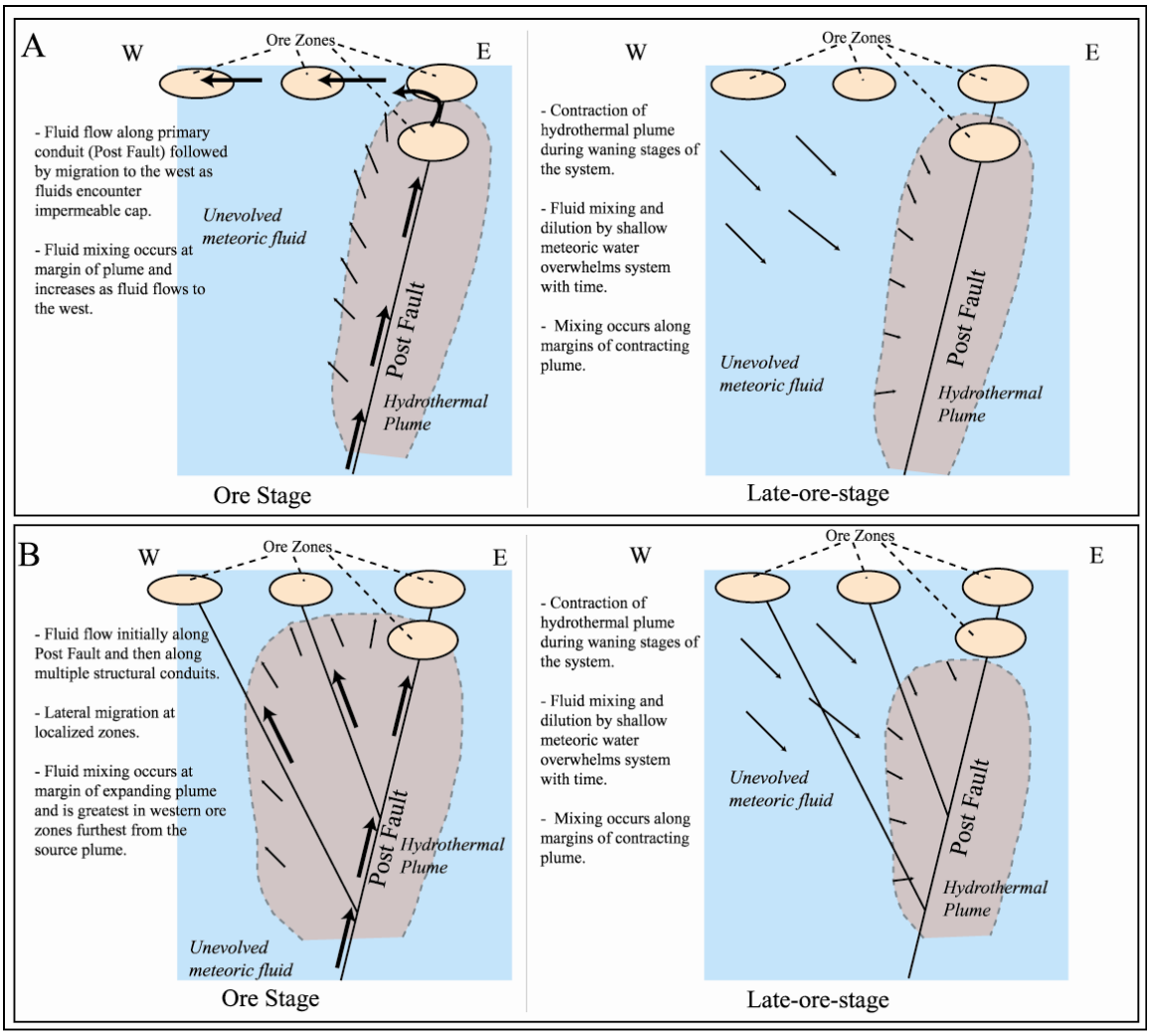

Figure 41. Schematic hydrothermal models illustrating fluid flow and gold deposition at the Betze-Post deposit. A) Fluid flow primarily along the Post Fault followed by lateral migration of the ore fluid induced by permeability and stratigraphic control. B) Ore fluid flow initially along the Post Fault and subsequently along multiple structural conduits. Lateral migration occurs locally within different ore zones. In both models, the hydrothermal plume contracts during the late-ore stage resulting in fluid mixing with unevolved meteoric fluids. Models not to scale.

along the JB Series Faults into the Betze and North Betze ore zones and along the Shalosky Fault into the Screamer ore zone (Figure 41b). Along each of these fluid conduits, localized aquitards and favorable stratigraphy would have forced ore fluids to migrate laterally along the Wispy unit at each ore zone resulting in the reaction between the ore fluid and host rocks and the precipitation of gold in trace element-rich pyrite. In this scenario ore fluids would have migrated along separate pathways and different distances to the various ore zones with greatest distance to the Screamer ore zone. Consequently, the fluids would have undergone increased fluid mixing with increased flow to the west. Similar to $\delta^{18}O$ trends identified at Betze-Post.

In both models, ore fluids migrated upward and reached impermeable aquitards, including intrusive bodies as observed in several sample transects, an impermeable fault planes, or less permeable lithologies. The fluids infiltrated stratigraphically favorable zones, reacted with and decarbonatized carbonate host rocks, increased porosity, and induced the precipitation of Au and As-rich pyrite.

This study does not distinguish which of the proposed pathways ore fluids followed. Results from this study did identify the most evolved ore fluids at the Deep Post ore zone. These fluids rose along the Post Fault and were diluted as they migrated to the west, and with time. Although this study has not identified specific fluid flow pathways across the Betze-Post deposit, this study demonstrates that ion-probe oxygen isotope analyses conducted on samples collected along potential fluid pathways and rigorously examined in paragenetic studies could successfully distinguish ore fluid pathways across a large ore system.

The initial goals of this study included the identification of vectors to ore,

interpretation of ore fluid migration across the deposit, and identification of sources for ore fluids at Betze-Post. This study shows that ion-probe oxygen isotope analyses can provide insight into the chemistry of different fluids in Carlin-type deposits as well as contributing to the identification of different quartz generations in these types of deposits. This technique, accompanied by strong paragenetic control, can provide a vector to ore stage quartz. Finally, δD signatures of ore stage inclusion fluids do not clearly identify the sources for ore fluids at Betze-Post. Though most analyses have unexplainable low values, the δD values may indicate a meteoric fluid source for ore fluids; however, single δD analysis, from North Betze, may indicate a deep magmatic or metamorphic component in the ore fluid. Additional δD analysis of ore stage inclusion fluids is encouraged to further constrain the sources of ore fluids at Betze-Post.

APPENDIX I

SAMPLES COLLECTED FROM BETZE-POST

331 core and hand samples were collected from the Betze-Post deposit. Samples were collected from drill core that crosscut all five ore zones within the Betze-Post system. A total of 15 drill holes and several areas within the open pit were sampled. Sampling focused on ore zones that exhibited a strong correlation between Au grade and silicification. Samples were collected at various elevations within the open pit and within individual drill holes.

Appendix 1. Samples collected from Betze-Post ore zones keyed according to conducted analyses.

#	Ore Zone	Drill Hole	Footage	Au-grade*	X (Easting)	Y (Northing)	Z (Elevation)**
1	Deep Post	P-175C	1212.0	1.038	12665.38	10957.91	4454.06
2	Deep Post	P-175C[4]	1245.0	0.948	12665.38	10957.91	na
3	Deep Post	P-175C	1253.0	0.948	12664.99	10962.36	4413.30
4	Deep Post	P-175C	1263.8	2.467	12664.88	10963.53	4402.57
5	Deep Post	P-175C	1266.1	0.202	12664.86	10963.78	4400.28
6	Deep Post	P-175C	1273.0	0.570	12664.80	10964.53	4393.42
7	Deep Post	P-175C	1289.0	0.430	12664.64	10966.27	4377.52
8	Deep Post	P-175C[S,1,4]	1312.0	1.301	12666.39	10947.19	4354.68
9	Deep Post	P-175C	1313.8	1.301	12666.38	10947.41	4352.90
10	Deep Post	P-175C	1318.8	0.790	12666.36	10948.01	4347.94
11	Deep Post	P-175C	1331.8	0.842	12666.31	10949.56	4335.05
12	Deep Post	P-175C	1357.6	0.366	12666.20	10952.65	4309.47
13	Deep Post	P-175C	1540.0	0.208	12666.70	10918.80	4128.00
14	Deep Post	RM97-2C	401.6	0.000	12676.93	10733.55	4205.91
15	Deep Post	RM97-2C	418.6	0.000	12677.48	10736.29	4189.15
16	Deep Post	RM97-2C	462.4	0.924	12678.94	10743.34	4145.94
17	Deep Post	RM97-2C	470.8	0.924	12679.22	10744.69	4137.66
18	Deep Post	RM97-2C	476.3	0.924	12679.41	10745.57	4132.23
19	Deep Post	RM97-2C	483.0	0.847	12679.63	10746.63	4125.62
20	Deep Post	RM97-2C	486.4	0.847	12679.75	10747.17	4122.26
21	Deep Post	RM97-2C[4]	488.0	0.847	12679.75	10747.17	4121.26
22	Deep Post	RM97-2C	492.8	0.847	12679.97	10748.17	4115.95
23	Deep Post	RM97-2C	514.5	0.523	12680.71	10751.59	4094.53
24	Deep Post	RM97-2C	538.6	0.432	12681.50	10755.35	4070.74
25	Deep Post	RM97-2C	599.0	0.303	12683.49	10764.72	4011.10
26	Deep Post	RM97-2C[4]	633.0	0.936	12683.49	10764.72	3969.25
27	Deep Post	RM97-2C[S,1]	638.3	0.936	12684.90	10770.72	3972.29
28	Deep Post	RM97-2C	1068.4	0.008	12698.84	10839.62	3548.01
29	Deep Post	RM97-9C	168.0	2.270	12638.86	10905.99	4311.83
30	Deep Post	RM97-9C	209.0	0.642	12639.63	10906.53	4270.84
31	Deep Post	RM97-9C	241.0	0.162	12640.16	10906.97	4238.85
32	Deep Post	RM97-9C	315.3	0.348	12640.83	10907.76	4164.55
33	Deep Post	RM97-9C	315.5	0.348	12640.83	10907.77	4164.35
34	Deep Post	RM97-9C[S,1]	315.6	0.348	12640.83	10907.77	4164.25
35	Deep Post	RM97-9C	363.1	0.173	12641.07	10908.21	4116.75
36	Deep Post	RM97-9C	390.8	0.208	12641.14	10908.46	4089.05

[S] Doubly polished thick section prepared

* Au assay based on measured Au concentration for five foot interval of core.

** Calculated elevation.

[1] CL and BEI imaging

[2] WDS trace element analyses

[3] Microthermometry

[4] SIMS $\delta^{18}O$ analysis

[5] δD and $\delta^{18}O$ analysis

Appendix 1. Samples collected from Betze-Post ore zones keyed according to conducted analyses.

#	Ore Zone	Drill Hole	Footage	Au-grade*	X (Easting)	Y (Northing)	Z (Elevation)**
37	Deep Post	RM97-9C	507.0	0.135	12641.85	10909.27	3972.85
38	Deep Post	RM97-9C	527.2	0.152	12642.04	10909.35	3952.65
39	Deep Post	RM97-9C	746.0	0.000	12643.28	10911.28	3733.85
40	North Post	BPC-13C	466.8	0.035	11141.75	13008.74	4653.54
41	North Post	BPC-13C	497.6	0.272	11141.74	13009.53	4622.74
42	North Post	BPC-13C	551.5	0.186	11141.45	13010.75	4568.86
43	North Post	BPC-13C[S]	594.0	0.099	11141.00	13011.44	4526.37
44	North Post	BPC-13C	631.3	0.047	11140.54	13027.20	4489.08
45	North Post	BPC-13C	665.8	0.058	11140.36	13012.26	4474.58
46	North Post	BPC-13C	691.8	0.033	11139.82	13013.04	4428.59
47	North Post	BPC-13C	697.4	0.075	11139.78	13013.15	4422.99
48	North Post	BPC-13C[S]	733.8	0.104	11139.48	13013.88	4386.60
49	North Post	BPC-13C	737.7	0.077	11139.45	13013.97	3586.82
50	North Post	BPC-13C	743.4	0.058	11139.40	13014.09	4377.01
51	North Post	BPC-13C	747.7	0.241	11139.37	13014.19	4372.71
52	North Post	BPC-13C	759.5	0.311	11139.27	13014.45	4360.91
53	North Post	BPC-13C[S,1]	760.0	0.311	11139.27	13014.46	4360.41
54	North Post	BPC-13C	766.4	0.020	11139.19	13014.58	4354.01
55	North Post	BPC-13C	769.8	0.020	11139.15	13014.64	4350.61
56	North Post	BPC-13C	770.5	0.014	11139.14	13014.66	4349.91
57	North Post	BPC-13C	775.0	0.021	11139.08	13014.74	4345.41
58	North Post	BPC-13C[S]	777.5	0.021	11139.05	13014.79	4342.91
59	North Post	BPC-13C[S]	785.5	0.021	11138.95	13014.94	4334.92
60	North Post	BPC-13C	795.1	0.006	11138.83	13015.12	4325.32
61	North Post	BPC-13C	1032.3	0.007	11136.40	13019.20	4088.10
62	North Post	PN-561C	1270.0	0.032	10541.68	14148.27	4229.07
63	North Post	PN-561C	1296.5	0.230	10540.29	14148.45	4202.61
64	North Post	PN-561C	1300.9	0.248	10545.28	14147.54	4198.21
65	North Post	PN-561C	1303.5	0.176	10545.15	14147.50	4195.61
66	North Post	PN-561C	1342.4	0.564	10543.17	14146.89	4156.77
67	North Post	PN-561C	1343.0	0.564	10543.14	14146.88	4156.17
68	North Post	PN-561C	1348.0	1.016	10542.88	14146.80	4151.18
69	North Post	PN-561C	1357.2	0.683	10547.53	14146.64	4141.99
70	North Post	PN-561C	1357.6	0.683	10547.51	14146.63	4141.59
71	North Post	PN-561C	1364.3	0.125	10547.19	14146.52	4134.90
72	North Post	PN-561C	1379.5	0.079	10546.46	14146.24	4119.72

[S] Doubly polished thick section prepared

* Au assay based on measured Au concentration for five foot interval of core.

** Calculated elevation.

[1] CL and BEI imaging

[2] WDS trace element analyses

[3] Microthermometry

[4] SIMS $\delta^{18}O$ analysis

[5] δD and $\delta^{18}O$ analysis

Appendix 1. Samples collected from Betze-Post ore zones keyed according to conducted analyses.

#	Ore Zone	Drill Hole	Footage	Au-grade*	X (Easting)	Y (Northing)	Z (Elevation)**
73	North Post	PN-561C	1462.0	0.005	10552.02	14144.67	4037.32
74	North Post	PN-561C	1684.5	0.000	10559.88	14140.72	3848.49
75	North Post	PN-471C	930.9	0.049	12256.89	11825.94	4151.00
76	North Post	PN-471C	943.0	0.026	12256.96	11826.57	4138.92
77	North Post	PN-471C	944.5	0.026	12256.97	11826.65	4137.42
78	North Post	PN-471C	1005.8	0.176	12257.34	11829.86	4076.21
79	North Post	PN-471C	1008.6	0.056	12257.35	11830.00	4073.42
80	North Post	PN-471C	1010.1	0.066	12257.36	11830.08	4071.92
81	North Post	PN-471C[S,1]	1013.0	0.066	12257.38	11830.23	4069.02
82	North Post	PN-471C	1015.5	0.104	12257.39	11830.37	4066.53
83	North Post	PN-471C	1016.0	0.104	12257.40	11830.39	4066.03
84	North Post	PN-471C	1018.3	0.104	12257.41	11830.51	4063.73
85	North Post	PN-471C[S,1,3]	1019.0	0.104	12257.42	11830.55	4063.03
86	North Post	PN-471C[S,1,3]	1025.0	0.399	12257.45	11830.86	4057.04
87	North Post	PN-471C	1037.0	0.006	12257.52	11831.49	4045.06
88	North Post	PN-471C	1055.5	0.058	12257.63	11832.46	4026.59
89	North Post	PN-471C	1082.0	0.006	12257.79	11833.85	4000.12
90	North Post	PN-471C	1154.5	0.001	12260.17	11837.64	3927.73
91	Betze	SJ-473C	702.0	0.321	9588.94	12115.43	4576.80
92	Betze	SJ-473C	708.2	0.141	9592.37	12115.61	4571.64
93	Betze	SJ-473C	720.5	0.271	9599.17	12115.96	4561.40
94	Betze	SJ-473C	733.5	0.329	9606.33	12116.22	4550.56
95	Betze	SJ-473C	741.8	0.022	9610.91	12116.39	4543.64
96	Betze	SJ-473C	743.0	0.022	9611.57	12116.41	4542.64
97	Betze	SJ-473C	745.5	0.034	9612.95	12116.46	4540.55
98	Betze	SJ-473C[S,1,3]	781.5	0.291	9632.80	12115.51	4510.53
99	Betze	SJ-473C[S,1]	784.0	0.291	9634.18	12115.55	4508.45
100	Betze	SJ-473C	785.8	0.276	9635.18	12115.58	4506.95
101	Betze	SJ-473C	786.6	0.276	9635.62	12115.60	4506.28
102	Betze	SJ-473C	789.0	0.276	9636.94	12115.64	4504.28
103	Betze	SJ-473C	804.5	0.065	9645.50	12114.55	4491.36
104	Betze	SJ-473C	811.0	0.169	9649.09	12114.65	4485.95
105	Betze	SJ-473C	818.0	0.121	9652.96	12114.75	4480.13
106	Betze	SJ-473C	818.8	0.121	9653.40	12114.77	4479.46
107	Betze	SJ-473C	827.0	0.282	9657.93	12114.89	4472.63
108	Betze	SJ-473C	836.5	0.444	9663.18	12115.04	4464.72

[S] Doubly polished thick section prepared

* Au assay based on measured Au concentration for five foot interval of core.

** Calculated elevation.

[1] CL and BEI imaging

[2] WDS trace element analyses

[3] Microthermometry

[4] SIMS $\delta^{18}O$ analysis

[5] δD and $\delta^{18}O$ analysis

Appendix 1. Samples collected from Betze-Post ore zones keyed according to conducted analyses.

#	Ore Zone	Drill Hole	Footage	Au-grade*	X (Easting)	Y (Northing)	Z (Elevation)**
109	Betze	SJ-473C	1008.6	0.000	9665.11	12113.87	4462.01
110	Betze	SJ-475C	15.7	0.131	9959.01	11914.77	4827.33
111	Betze	SJ-475C[S,1,3]	17.6	0.131	9958.93	11914.10	4825.56
112	Betze	SJ-475C	82.7	0.174	9956.81	11890.84	4764.79
113	Betze	SJ-475C	93.9	0.041	9956.50	11886.85	4754.33
114	Betze	SJ-475C	118.0	0.192	9955.24	11872.75	4717.15
115	Betze	SJ-475C	132.3	0.154	9955.41	11873.16	4718.47
116	Betze	SJ-475C	135.4	0.079	9955.32	11872.05	4715.58
117	Betze	SJ-475C[S,1]	138.5	0.079	9955.23	11870.94	4712.68
118	Betze	SJ-475C	142.8	0.012	9955.10	11869.40	4708.67
119	Betze	SJ-475C	149.0	0.007	9954.91	11867.19	4702.89
120	Betze	SJ-475C[S,1,4]	150.0	0.019	9954.88	11866.83	4701.95
121	Betze	SJ-475C	181.3	0.081	9953.94	11855.69	4672.72
122	Betze	SJ-475C	182.3	0.081	9953.91	11855.33	4671.79
123	Betze	SJ-475C	187.2	0.076	9953.76	11853.59	4667.21
124	Betze	SJ-475C	891.0	0.025	9923.32	11619.45	4007.45
125	Betze	SJ-562CA	557.4	0.005	9124.97	11816.21	4691.41
126	Betze	SJ-562CA	561.4	0.015	9130.00	11790.00	4722.96
127	Betze	SJ-562CA	563.2	0.015	9129.26	11789.57	4721.38
128	Betze	SJ-562CA[S,1]	570.0	0.017	9126.45	11787.94	4715.40
129	Betze	SJ-562CA	593.3	0.001	9116.81	11782.36	4694.94
130	Betze	SJ-562CA	607.8	0.819	9117.79	11753.36	4717.32
131	Betze	SJ-562CA	616.2	0.849	9114.35	11751.36	4709.92
132	Betze	SJ-562CA	628.0	0.158	9109.52	11748.56	4699.53
133	Betze	SJ-562CA	634.2	0.213	9106.98	11747.09	4694.07
134	Betze	SJ-562CA	637.0	0.067	9105.83	11746.42	4691.60
135	Betze	SJ-562CA[S,1]	639.3	0.067	9104.89	11745.88	4689.58
136	Betze	SJ-562CA	641.0	0.036	9111.08	11719.74	4723.31
137	Betze	SJ-562CA	644.7	0.021	9109.57	11718.86	4720.05
138	Betze	SJ-562CA[S,1]	647.6	0.021	9108.39	11718.17	4717.49
139	Betze	SJ-562CA	650.2	0.031	9107.33	11717.55	4715.20
140	Betze	SJ-562CA	657.8	0.048	9104.23	11715.74	4708.51
141	Betze	SJ-562CA	660.8	0.128	9103.00	11715.02	4705.86
142	Betze	SJ-562CA[S,1,4]	664.1	0.128	9101.66	11714.24	4702.95
143	Betze	SJ-562CA	667.0	0.043	9100.47	11713.55	4700.40
144	Betze	SJ-562CA	674.5	0.092	9097.41	11711.76	4693.79

[S] Doubly polished thick section prepared

* Au assay based on measured Au concentration for five foot interval of core.

** Calculated elevation.

[1] CL and BEI imaging

[2] WDS trace element analyses

[3] Microthermometry

[4] SIMS $\delta^{18}O$ analysis

[5] δD and $\delta^{18}O$ analysis

Appendix 1. Samples collected from Betze-Post ore zones keyed according to conducted analyses.

#	Ore Zone	Drill Hole	Footage	Au-grade*	X (Easting)	Y (Northing)	Z (Elevation)**
145	Betze	SJ-562CA	689.3	0.165	9098.17	11682.48	4716.00
146	Betze	SJ-562CA	692.8	0.127	9096.75	11681.64	4712.92
147	Betze	SJ-562CA	772.8	0.164	9077.58	11611.10	4712.85
148	Betze	SJ-562CA	779.0	0.225	9075.13	11609.63	4707.35
149	Betze	SJ-562CA	789.8	0.388	9070.85	11607.06	4697.76
150	Betze	SJ-562CA	796.8	0.211	9068.09	11605.40	4691.55
151	Betze	SJ-562CA	951.1	0.001	8869.50	12043.40	3895.80
152	North Betze	SJ-263C	955.0	0.027	9724.47	13326.92	4531.56
153	North Betze	SJ-263C	955.3	0.027	9724.47	13326.92	4531.56
154	North Betze	SJ-263C	1011.5	0.233	9725.33	13303.09	4475.14
155	North Betze	SJ-263C	1013.5	0.233	9725.35	13302.98	4473.14
156	North Betze	SJ-263C	1017.6	0.040	9725.39	13302.77	4469.05
157	North Betze	SJ-263C[S,1]	1022.0	0.164	9725.43	13302.54	4464.66
158	North Betze	SJ-263C[S,1,3]	1027.0	2.119	9725.48	13302.28	4459.66
159	North Betze	SJ-263C	1028.0	2.119	9725.49	13302.23	4458.66
160	North Betze	SJ-263C[S,1,2]	1035.0	5.120	9725.56	13301.88	4451.67
161	North Betze	SJ-263C	1037.2	5.120	9725.58	13301.77	4449.47
162	North Betze	SJ-263C[S,1,3]	1041.5	3.301	9725.62	13301.56	4445.18
163	North Betze	SJ-263C[4]	1042.1	3.301	9725.62	13301.56	4445.18
164	North Betze	SJ-263C	1048.1	0.572	9725.68	13301.23	4438.59
165	North Betze	SJ-263C[S,1]	1050.0	0.572	9725.70	13301.13	4436.69
166	North Betze	SJ-263C[4]	1051.0	0.572	9725.70	13301.13	4436.69
167	North Betze	SJ-263C	1053.5	0.024	9725.73	13300.96	4433.19
168	North Betze	SJ-263C	1054.0	0.024	9725.73	13300.93	4432.69
169	North Betze	SJ-263C	1056.2	0.018	9725.75	13300.82	4430.50
170	North Betze	SJ-263C[S,1]	1063.2	0.010	9725.80	13300.46	4423.51
171	North Betze	SJ-263C	1077.7	0.018	9725.91	13299.76	4409.02
172	North Betze	SJ-263C	1087.0	0.918	9725.98	13299.30	4399.73
173	North Betze	SJ-263C	1455.0	0.001	9729.00	13290.10	4032.10
174	North Betze	SJ-305C	911.3	0.001	9704.55	13211.07	4586.25
175	North Betze	SJ-305C	960.0	0.070	9705.75	13211.57	4537.61
176	North Betze	SJ-305C	985.0	0.212	9757.38	13211.81	4512.65
177	North Betze	SJ-305C	995.5	0.212	9757.92	13211.90	4502.16
178	North Betze	SJ-305C	997.5	0.161	9758.02	13211.92	4500.17
179	North Betze	SJ-305C	1014.5	0.123	9758.89	13212.06	4483.19

[S] Doubly polished thick section prepared

* Au assay based on measured Au concentration for five foot interval of core.

** Calculated elevation.

[1] CL and BEI imaging

[2] WDS trace element analyses

[3] Microthermometry

[4] SIMS $\delta^{18}O$ analysis

[5] δD and $\delta^{18}O$ analysis

Appendix 1. Samples collected from Betze-Post ore zones keyed according to conducted analyses.

#	Ore Zone	Drill Hole	Footage	Au-grade*	X (Easting)	Y (Northing)	Z (Elevation)**
180	North Betze	SJ-305C	1022.0	0.378	9759.28	13212.12	4475.70
181	North Betze	SJ-305C	1035.5	0.307	9759.97	13212.24	4462.21
182	North Betze	SJ-305C	1038.0	0.307	9760.10	13212.26	4459.72
183	North Betze	SJ-305C	1039.2	0.307	9760.16	13212.27	4457.52
184	North Betze	SJ-305C[S,1,2,3,4,5]	1041.2	0.260	9760.27	13212.29	4455.52
185	North Betze	SJ-305C	1048.5	0.571	9760.64	13212.35	4448.23
186	North Betze	SJ-305C	1049.5	0.571	9760.69	13212.36	4447.23
187	North Betze	SJ-305C	1051.5	0.284	9760.80	13212.38	4446.23
188	North Betze	SJ-305C	1057.8	0.499	9761.11	13212.45	4439.94
189	North Betze	SJ-305C	1064.0	3.934	9761.43	13212.52	4433.75
190	North Betze	SJ-305C	1068.0	4.301	9761.63	13212.56	4429.76
191	North Betze	SJ-305C[S,1,4]	1069.7	4.301	9761.71	13212.58	4428.06
192	North Betze	SJ-305C[S,1]	1072.8	0.918	9761.87	13212.62	4424.97
193	North Betze	SJ-305C	1081.5	3.073	9762.30	13212.71	4416.28
194	North Betze	SJ-305C	1095.5	0.279	9762.98	13212.87	4402.29
195	North Betze	SJ-305C	1097.0	0.279	9763.10	13212.89	4400.80
196	North Betze	SJ-305C	1111.0	0.295	9763.75	13213.03	4386.81
197	North Betze	SJ-305C	1119.5	1.760	9764.17	13213.12	4378.32
198	North Betze	SJ-305C	1124.5	1.479	9764.42	13213.17	4373.33
199	North Betze	SJ-305C[S,1,3]	1128.5	3.330	9764.62	13213.20	4369.13
200	North Betze	SJ-305C	1169.2	0.012	9766.63	13213.57	4328.69
201	North Betze	SJ-305C	1198.0	0.003	9767.95	13213.86	4299.92
202	North Betze	SJ-305C	1398.0	0.001	9772.70	13214.85	4192.83
203	North Betze	SJ-456C	1034.2	0.001	9606.91	13631.59	4185.39
204	North Betze	SJ-456C	1071.0	0.031	9609.72	13674.25	4411.73
205	North Betze	SJ-456C	1080.5	0.028	9610.44	13672.50	4402.43
206	North Betze	SJ-456C	1087.0	0.011	9610.93	13671.30	4396.06
207	North Betze	SJ-456C	1090.4	0.053	9611.19	13670.67	4392.73
208	North Betze	SJ-456C	1090.8	0.053	9611.22	13670.60	4392.33
209	North Betze	SJ-456C[S,1]	1102.0	0.045	9612.07	13668.53	4381.36
210	North Betze	SJ-456C	1104.2	0.045	9612.24	13668.12	4379.20
211	North Betze	SJ-456C	1127.2	0.050	9613.99	13663.87	4356.67
212	North Betze	SJ-456C	1139.0	0.039	9614.89	13661.70	4345.11
213	North Betze	SJ-456C[S,1,3,5]	1161.9	0.355	9616.63	13657.47	4322.67
214	North Betze	SJ-456C	1166.5	2.058	9616.98	13656.62	4318.16
215	North Betze	SJ-456C[S,1,3,4,5]	1167.0	2.058	9617.02	13656.52	4317.67

[S] Doubly polished thick section prepared

* Au assay based on measured Au concentration for five foot interval of core.

** Calculated elevation.

[1] CL and BEI imaging

[2] WDS trace element analyses

[3] Microthermometry

[4] SIMS $\delta^{18}O$ analysis

[5] δD and $\delta^{18}O$ analysis

Appendix 1. Samples collected from Betze-Post ore zones keyed according to conducted analyses.

#	Ore Zone	Drill Hole	Footage	Au-grade*	X (Easting)	Y (Northing)	Z (Elevation)**
216	North Betze	SJ-456C	1169.8	2.058	9617.23	13656.01	4314.93
217	North Betze	SJ-456C	1177.3	0.164	9617.80	13654.62	4307.58
218	North Betze	SJ-456C	1179.5	0.164	9617.97	13654.22	4305.42
219	North Betze	SJ-456C	1180.2	0.062	9618.02	13654.09	4304.74
220	North Betze	SJ-456C[S,1]	1199.5	0.035	9619.49	13650.52	4285.82
221	North Betze	SJ-456C	1302.0	0.005	9627.28	13631.59	4185.39
222	North Betze	SJ-457C	897.0	0.021	9664.03	13593.31	4502.02
223	North Betze	SJ-457C	914.5	0.026	9663.66	13594.26	4484.55
224	North Betze	SJ-457C	927.0	0.021	9663.42	13594.93	4472.07
225	North Betze	SJ-457C[S,1]	974.2	0.099	9662.58	13597.43	4424.94
226	North Betze	SJ-457C[S,1]	990.0	0.151	9662.33	13598.26	4409.17
227	North Betze	SJ-457C	992.0	0.151	9662.30	13598.36	4407.17
228	North Betze	SJ-457C	997.0	0.118	9662.22	13598.62	4402.18
229	North Betze	SJ-457C	1010.0	0.471	9662.03	13599.31	4389.20
230	North Betze	SJ-457C	1023.0	0.797	9661.85	13599.99	4376.21
231	North Betze	SJ-457C[S,1]	1024.5	0.797	9661.83	13600.07	4374.72
232	North Betze	SJ-457C	1025.0	3.501	9661.82	13600.10	4374.22
233	North Betze	SJ-457C[4]	1026.0	3.501	9661.82	13600.10	4374.22
234	North Betze	SJ-457C[S,1]	1028.5	3.501	9661.77	13600.28	4370.72
235	North Betze	SJ-457C	1043.0	0.225	9661.57	13601.05	4356.24
236	North Betze	SJ-457C[4]	1052.0	1.040	9661.57	13601.05	4355.24
237	North Betze	SJ-457C[4]	1052.5	1.040	9661.57	13601.05	4355.74
238	North Betze	SJ-457C[S,1]	1052.8	1.040	9661.44	13601.57	4346.46
239	North Betze	SJ-457C	1070.0	0.023	9661.21	13602.47	4329.29
240	North Betze	SJ-457C	1072.0	0.023	9661.19	13602.58	4327.29
241	North Betze	SJ-457C	1073.5	0.048	9661.17	13602.66	4325.79
242	North Betze	SJ-457C[S,1]	1101.8	0.007	9660.79	13604.13	4297.53
243	North Betze	SJ-457C	1168.0	0.002	9659.92	13607.55	4231.43
244	Screamer	BZ-960C	1103.2	0.021	7401.04	11225.29	4441.33
245	Screamer	BZ-960C	1112.4	0.028	7402.48	11227.91	4432.63
246	Screamer	BZ-960C	1165.0	0.198	7410.96	11242.79	4382.90
247	Screamer	BZ-960C	1166.0	0.198	7411.12	11243.07	4381.95
248	Screamer	BZ-960C	1171.2	0.196	7411.99	11244.53	4377.04
249	Screamer	BZ-960C	1172.2	0.196	7412.15	11244.81	4376.09

[S] Doubly polished thick section prepared

* Au assay based on measured Au concentration for five foot interval of core.

** Calculated elevation.

[1] CL and BEI imaging

[2] WDS trace element analyses

[3] Microthermometry

[4] SIMS $\delta^{18}O$ analysis

[5] δD and $\delta^{18}O$ analysis

Appendix 1. Samples collected from Betze-Post ore zones keyed according to conducted analyses.

#	Ore Zone	Drill Hole	Footage	Au-grade*	X (Easting)	Y (Northing)	Z (Elevation)**
250	Screamer	BZ-960C[S]	1173.0	0.196	7412.28	11245.04	4375.34
251	Screamer	BZ-960C	1183.5	0.290	7414.03	11248.00	4365.41
252	Screamer	BZ-960C	1188.5	0.369	7414.85	11249.40	4360.69
253	Screamer	BZ-960C	1192.0	0.755	7415.43	11250.39	4357.38
254	Screamer	BZ-960C	1192.5	0.755	7415.52	11250.53	4356.91
255	Screamer	BZ-960C[S,1,3]	1193.8	0.755	7415.73	11250.89	4355.68
256	Screamer	BZ-960C	1194.0	0.755	7415.77	11250.95	4355.49
257	Screamer	BZ-960C	1197.0	0.368	7416.26	11251.80	4352.66
258	Screamer	BZ-960C	1197.2	0.368	7416.30	11251.85	4352.47
259	Screamer	BZ-960C[S,1,4]	1197.5	0.368	7416.35	11251.94	4352.18
260	Screamer	BZ-960C	1214.0	0.189	7419.14	11256.56	4336.59
261	Screamer	BZ-960C	1218.4	0.103	7419.89	11257.79	4332.43
262	Screamer	BZ-960C	1222.0	0.255	7420.50	11258.79	4329.03
263	Screamer	BZ-960C	1224.6	0.255	7420.94	11259.52	4326.57
264	Screamer	BZ-960C	1228.7	0.295	7421.64	11260.67	4322.70
265	Screamer	BZ-960C	1235.7	0.127	7422.83	11262.63	4316.08
266	Screamer	BZ-960C	1242.6	0.322	7424.02	11264.56	4309.57
267	Screamer	BZ-960C	1243.0	0.322	7424.09	11264.68	4309.19
268	Screamer	BZ-960C[S,1]	1247.0	0.366	7424.79	11265.81	4305.42
269	Screamer	BZ-960C	1264.5	0.174	7427.88	11270.75	4288.92
270	Screamer	BZ-960C	1275.5	0.263	7429.82	11273.86	4278.54
271	Screamer	BZ-960C	1277.5	0.263	7430.17	11274.42	4276.66
272	Screamer	BZ-960C	1405.0	0.000	7447.49	11301.63	4184.90
273	Screamer	BZ-915C[4]	1073.1	na	na	na	na
274	Screamer	SJ-552C[S,1]	1030.5	0.133	7203.64	12292.78	4496.51
275	Screamer	SJ-552C[S,1]	1054.5	0.597	7199.52	12288.09	4473.51
276	Screamer	SJ-552C	1106.0	0.148	7190.78	12277.97	4423.77
277	Screamer	SJ-552C	1121.0	0.559	7188.27	12274.99	4409.28
278	Screamer	SJ-552C	1139.8	0.518	7185.18	12271.28	4391.12
279	Screamer	SJ-552C	1154.0	0.867	7182.85	12268.48	4377.40
280	Screamer	SJ-552C[S,1]	1167.7	0.730	7180.87	12265.51	4364.17
281	Screamer	SJ-552C	1168.6	0.730	7180.75	12265.31	4363.31
282	Screamer	SJ-552C	1172.8	0.107	7180.21	12264.34	4359.26
283	Screamer	SJ-552C[S,1]	1184.0	0.017	7178.76	12261.76	4348.46

[S] Doubly polished thick section prepared

* Au assay based on measured Au concentration for five foot interval of core.

** Calculated elevation.

[1] CL and BEI imaging

[2] WDS trace element analyses

[3] Microthermometry

[4] SIMS $\delta^{18}O$ analysis

[5] δD and $\delta^{18}O$ analysis

Appendix 1. Samples collected from Betze-Post ore zones keyed according to conducted analyses.

#	Ore Zone	Drill Hole	Footage	Au-grade*	X (Easting)	Y (Northing)	Z (Elevation)**
284	Screamer	SJ-552C	1191.5	0.012	7177.79	12260.03	4341.22
285	Screamer	SJ-552C	1191.8	0.012	7177.75	12259.96	4340.93
286	Screamer	SJ-552C	1195.8	0.015	7177.24	12259.04	4337.08
287	Screamer	SJ-552C	1196.0	0.015	7177.21	12258.99	4336.88
288	Screamer	SJ-552C[S,1]	1201.2	0.005	7176.54	12257.79	4331.87
289	Screamer	SJ-552C	1320.0	0.013	7161.00	12230.40	4217.90
290	Screamer	RM01-3C	859.8	0.051	7310.41	11848.98	4379.89
291	Screamer	RM01-3C	870.0	0.024	7310.68	11848.90	4369.70
292	Screamer	RM01-3C	870.5	0.071	7310.69	11848.90	4369.20
293	Screamer	RM01-3C	871.9	0.071	7310.73	11848.89	4367.80
294	Screamer	RM01-3C	875.0	0.054	7310.81	11848.87	4364.70
295	Screamer	RM01-3C	885.0	0.036	7308.72	11848.81	4354.70
296	Screamer	RM01-3C	888.5	0.037	7308.62	11848.80	4351.20
297	Screamer	RM01-3C	890.0	0.041	7308.58	11848.80	4349.71
298	Screamer	RM01-3C	897.3	0.036	7308.37	11848.77	4342.41
299	Screamer	RM01-3C	903.8	0.081	7308.18	11848.75	4335.91
300	Screamer	RM01-3C	908.4	0.073	7308.05	11848.74	4331.31
301	Screamer	RM01-3C	917.3	0.087	7307.80	11848.71	4322.42
302	Screamer	RM01-3C	921.5	0.064	7307.67	11848.70	4318.22
303	Screamer	RM01-3C	921.7	0.064	7307.67	11848.70	4318.02
304	Screamer	RM01-3C	923.5	0.064	7307.61	11848.70	4316.22
305	Screamer	RM01-3C	940.0	0.085	7307.11	11848.69	4299.73
306	Screamer	RM01-3C[S,1]	966.5	0.307	7306.30	11848.68	4273.24
307	Screamer	RM01-3C	997.8	0.432	7305.31	11848.71	4241.96
308	Screamer	RM01-3C	998.0	0.432	7305.30	11848.71	4241.76
309	Screamer	RM01-3C	1008.2	0.318	7304.98	11848.72	4231.56
310	S1-1	Pit Sample[S,1]		0.083	11780.00	12540.00	4400.00
311	S1-120	Pit Sample[S,1,2]			11780.00	12540.00	4400.00
312	S1-91	Pit Sample[S,1]			11780.00	12540.00	4400.00
313	S1-2	Pit Sample		0.020	11780.00	12540.00	4400.00
314	S2-1	Pit Sample		0.004	11050.00	12780.00	4400.00
315	S3-1	Pit Sample[S,1]		0.115	10660.00	12570.00	4400.00
316	S4	Pit Sample			10250.00	11480.00	4380.00
317	S5-1	Pit Sample		0.226	9330.00	11995.00	4280.00
318	S5-2	Pit Sample		0.033	9330.00	11995.00	4280.00

[S] Doubly polished thick section prepared

* Au assay based on measured Au concentration for five foot interval of core.

** Calculated elevation.

[1] CL and BEI imaging

[2] WDS trace element analyses

[3] Microthermometry

[4] SIMS $\delta^{18}O$ analysis

[5] δD and $\delta^{18}O$ analysis

Appendix 1. Samples collected from Betze-Post ore zones keyed according to conducted analyses.

#	Ore Zone	Drill Hole	Footage	Au-grade*	X (Easting)	Y (Northing)	Z (Elevation)**
319	S6-2	Pit Sample		0.101	9410.00	12540.00	4280.00
320	S7-2	Pit Sample[S,1]		0.126	12600.00	11600.00	4360.00
321	S7-B	Pit Sample[S,1]			12600.00	11600.00	4360.00
322	S8-1	Pit Sample		0.038	10890.00	13050.00	5120.00
323	S9-2	Pit Sample[S,1]		0.004	11300.00	14180.00	5160.00
324	S10-1	Pit Sample		0.003	10140.00	13930.00	5120.00
325	S11-1	Pit Sample[S,1]		0.005	8200.00	10550.00	5120.00
326	GP-S1	Pit Sample[S,1]		0.111	11275.00	13095.00	4560.00
327	GP-S2	Pit Sample[S,1]		0.023	11480.00	13015.00	4480.00
328	GP-S3	Pit Sample		0.011	11210.00	12480.00	4440.00
329	GP-S4	Pit Sample		0.007	11939.58	11708.52	4360.00
330	GP-14	Pit Sample[S,1]			10602.50	12466.70	4440.00
331	GP-UN	Pit Sample		0.065			

[S] Doubly polished thick section prepared

* Au assay based on measured Au concentration for five foot interval of core.

** Calculated elevation.

[1] CL and BEI imaging

[2] WDS trace element analyses

[3] Microthermometry

[4] SIMS $\delta^{18}O$ analysis

[5] δD and $\delta^{18}O$ analysis

APPENDIX II

ELECTRON MICROPROBE DATA FROM QUARTZ

EMPA analyses were conducted on quartz from all stages of the paragenesis. Wavelength dispersive spectrometry (WDS) Analysis was conducted to quantify concentrations of common elements that can be incorporated into quartz during initial precipitation.

The goals in conducting WDS analyses on quartz are two-fold. First, by identifying unique chemical signatures in different quartz generations, the quartz paragenesis can be further refined and a possible vector to ore could be developed. Second, by conducting EMPA analysis on quartz samples with different luminescence, the trace element cause for each quartz type's luminescence can be determined.

Analysis was conducted for a suite of 12 elements. These elements include Si, Fe, S, Al, As, Zn, Pb, Au, Ti, Ag, Mg, and Sb. These elements were quantified because they are either commonly associated with the Carlin-type suite or found as elevated levels in ore-bearing sulfides or they commonly replace Si in quartz during precipitation.

Appendix 2. Wavelength dispersive spectrometry data collected from ore stage and late-ore-stage quartz generations.

"---" Below detection limits

Sample	Ore zone	CL	Si	Fe	S	Al	As	Zn	Pb	Au	Ti	Ag	Mg	Sb	Total
Pit S1-120	Pit sample	CL-dark	98.666	---	---	0.134	---	---	---	---	---	---	---	0.010	98.814
Pit S1-120	Pit sample	CL-dark	97.245	---	---	0.575	---	---	---	---	0.003	0.003	---	0.016	97.845
Pit S1-120	Pit sample	CL-dark	98.334	---	0.007	---	---	0.003	---	---	---	---	---	0.007	98.351
Pit S1-120	Pit sample	CL-dark	98.488	---	---	0.009	---	0.004	---	---	---	---	---	0.014	98.517
Pit S1-120	Pit sample	CL-dark	98.060	---	0.006	0.013	---	---	---	---	---	---	---	0.026	98.112
Pit S1-120	Pit sample	CL-dark	98.978	---	0.011	---	---	---	---	---	---	0.003	0.006	0.009	99.012
Pit S1-120	Pit sample	CL-dark	99.455	0.004	0.005	0.446	---	---	---	---	---	---	---	0.007	99.918
Pit S1-120	Pit sample	CL-dark	98.821	0.005	---	0.198	---	---	---	---	---	0.003	---	0.022	99.050
Pit S1-120	Pit sample	CL-dark	98.619	---	---	0.067	---	---	---	---	---	---	0.006	0.111	98.804
Pit S1-120	Pit sample	CL-dark	98.750	---	---	0.382	---	0.008	---	---	---	---	---	0.068	99.208
Pit S1-120	Pit sample	CL-dark	99.834	---	---	---	---	---	---	---	---	---	---	0.056	99.894
Pit S1-120	Pit sample	CL-dark	100.013	0.009	0.006	---	---	0.007	0.008	---	---	0.003	---	0.043	100.092
SJ-263C-1035.0	North Betze	CL-dark	97.750	0.039	---	0.090	---	---	---	---	---	0.013	0.007	0.082	97.984
SJ-263C-1035.0	North Betze	CL-dark	98.941	0.118	0.012	0.939	---	0.015	---	---	---	---	0.024	---	100.052
SJ-263C-1035.0	North Betze	CL-dark	101.239	0.015	---	---	---	---	---	---	---	---	---	0.101	101.368
SJ-263C-1035.0	North Betze	CL-dark	98.624	0.005	0.147	---	---	---	---	---	---	0.010	0.037	0.052	98.875
SJ-263C-1035.0	North Betze	CL-dark	99.155	0.010	0.031	0.715	---	---	0.008	---	---	---	0.008	---	99.927
SJ-305C-1041.2	North Betze	CL-dark	100.291	---	---	0.673	---	---	---	---	0.004	---	---	0.004	100.974
SJ-305C-1041.2	North Betze	CL-dark	100.641	---	0.012	0.638	---	---	---	---	---	---	---	---	101.296
SJ-305C-1041.2	North Betze	CL-dark	99.446	---	0.011	0.906	---	---	0.011	---	---	---	---	---	100.383
SJ-305C-1041.2	North Betze	CL-dark	99.787	---	0.016	0.975	---	---	0.009	---	---	---	---	0.010	100.803
SJ-305C-1041.2	North Betze	CL-dark	100.156	---	0.017	0.344	---	---	---	---	---	---	---	0.005	100.524
SJ-305C-1041.2	North Betze	CL-dark	99.677	0.006	0.023	0.644	---	---	---	---	0.009	---	---	---	100.362
SJ-305C-1041.2	North Betze	CL-dark	98.756	---	---	0.696	---	0.014	---	---	---	---	---	---	99.472
SJ-305C-1041.2	North Betze	CL-dark	98.294	---	0.008	0.760	---	---	0.013	---	---	---	---	0.012	99.087
SJ-305C-1041.2	North Betze	CL-dark	97.459	---	0.023	0.751	---	---	---	---	---	---	---	0.007	98.240
SJ-305C-1041.2	North Betze	CL-dark	93.297	---	0.054	0.689	---	0.014	---	---	0.009	---	0.041	---	94.107
SJ-305C-1041.2	North Betze	CL-dark	96.073	0.008	0.032	0.734	---	0.015	---	---	---	---	0.020	0.008	96.893
SJ-305C-1041.2	North Betze	CL-dark	98.915	---	0.011	0.779	---	---	---	---	---	---	0.014	0.004	99.726
SJ-305C-1041.2	North Betze	CL-dark	96.988	---	0.039	0.689	0.011	0.017	---	---	---	0.011	---	---	97.749
	Average Detection Limits:		0.006	0.004	0.005	0.007	0.021	0.005	0.006	0.014	0.005	0.004	0.006	0.004	

Appendix 2. Wavelength dispersive spectrometry data collected from ore stage and late-ore-stage quartz generations.

"---" Below detection limits

Sample	Ore zone	CL	Si	Fe	S	Al	As	Zn	Pb	Au	Ti	Ag	Mg	Sb	Total
Pit S1-120	Pit sample	CL-bright	102.790	---	0.008	---	---	---	---	0.058	---	0.005	0.008	---	102.179
Pit S1-120	Pit sample	CL-bright	99.777	---	---	0.032	---	0.007	0.012	---	---	0.003	---	---	99.839
Pit S1-120	Pit sample	CL-bright	97.585	---	---	0.728	---	0.010	---	---	---	---	---	0.031	98.357
Pit S1-120	Pit sample	CL-bright	99.553	---	0.005	0.425	---	---	---	---	---	---	---	0.048	100.032
Pit S1-120	Pit sample	CL-bright	99.471	---	---	---	---	0.003	---	---	---	0.003	---	0.022	99.501
Pit S1-120	Pit sample	CL-bright	99.468	---	---	0.005	---	0.005	---	---	---	0.005	---	0.023	99.508
Pit S1-120	Pit sample	CL-bright	98.407	0.021	0.025	0.006	---	---	0.007	---	---	0.004	---	---	98.470
Pit S1-120	Pit sample	CL-bright	98.553	0.005	---	---	---	---	---	---	---	0.005	0.007	---	98.576
Pit S1-120	Pit sample	CL-bright	99.707	---	0.006	0.749	---	0.011	---	---	---	---	0.007	0.004	100.486
Pit S1-120	Pit sample	CL-bright	98.449	---	---	---	---	0.006	---	---	---	---	0.008	0.231	98.696
Pit S1-120	Pit sample	CL-bright	98.606	---	---	0.137	---	---	---	---	---	0.005	---	0.211	98.966
Pit S1-120	Pit sample	CL-bright	99.983	---	0.009	---	---	---	---	---	---	---	---	0.040	100.035
Pit S1-120	Pit sample	CL-bright	99.361	---	---	---	---	---	---	---	---	---	---	0.013	99.381
Pit S1-120	Pit sample	CL-bright	99.270	---	---	---	---	0.007	0.009	---	---	---	---	0.011	99.306
SJ-263C-1035.0	North Betze	CL-multiple	101.818	0.005	---	---	---	---	---	---	---	0.007	---	0.267	102.097
SJ-263C-1035.0	North Betze	CL-multiple	101.273	0.007	---	---	---	---	---	---	---	---	---	0.187	101.473
SJ-263C-1035.0	North Betze	CL-multiple	101.077	---	---	---	---	---	---	---	---	---	0.007	0.123	101.207
SJ-263C-1035.0	North Betze	CL-multiple	100.171	---	---	---	---	---	---	---	---	---	0.016	0.011	100.204
SJ-263C-1035.0	North Betze	CL-multiple	102.397	0.007	0.012	---	---	---	0.013	---	---	---	---	0.173	102.605
SJ-263C-1035.0	North Betze	CL-multiple	101.441	0.008	---	---	---	---	---	---	---	---	---	0.191	101.642
SJ-263C-1035.0	North Betze	CL-multiple	101.440	0.007	---	---	---	---	---	---	---	---	---	0.120	101.577
SJ-305C-1041.2	North Betze	CL-multiple	101.662	---	---	0.069	---	---	---	---	---	0.012	---	0.030	101.775
SJ-305C-1041.2	North Betze	CL-multiple	101.460	0.005	---	---	---	---	0.009	---	0.012	---	---	0.243	101.739
SJ-305C-1041.2	North Betze	CL-multiple	102.047	---	---	---	---	---	---	---	---	---	---	0.105	102.152
SJ-305C-1041.2	North Betze	CL-multiple	100.491	---	0.023	0.048	---	---	---	---	---	---	0.019	0.099	100.685
SJ-305C-1041.2	North Betze	CL-multiple	101.196	0.006	0.006	---	---	---	---	---	---	---	---	0.020	101.238
SJ-305C-1041.2	North Betze	CL-multiple	101.050	---	0.023	---	---	---	---	---	---	---	---	0.007	101.081
SJ-305C-1041.2	North Betze	CL-multiple	101.770	0.013	0.009	---	---	---	---	---	---	---	0.006	0.187	101.993
SJ-305C-1041.2	North Betze	CL-multiple	99.129	---	0.011	0.474	---	---	---	---	---	---	---	0.006	99.626
SJ-305C-1041.2	North Betze	CL-multiple	95.207	---	0.195	0.033	---	0.011	---	---	---	---	0.045	0.021	95.512
	Average Detection Limits:		0.006	0.004	0.005	0.007	0.021	0.005	0.006	0.014	0.005	0.004	0.006	0.004	

APPENDIX III

MICROTHERMOMETRY DATA

Microthermometry was conducted on all four types of fluid inclusions identified in ore stage quartz at Betze-Post. Homogenization and ice melting temperatures were determined on a computer automated Linkman-style fluid inclusion stage. Homogenization temperatures and ice melting temperatures were constrained by analyzing the contraction and expansion of the vapor bubble within individual fluid inclusions. Salinities were calculated based on pressure determinations derived by Hall et al. (1988).

Appendix 3. Microthermometric data collected from fluid inclusions in ore stage quartz.

Sample	Ore zone	Origin	Assemblage	~Freezing T	Ice Melting T	Salinity*	T(h)**
PNC-471-1019.0	North Post	Primary	F2a2				155.0
PNC-471-1019.0	North Post	Primary	F2a2				175.0
SJ-456C-1167.0	North Betze	Primary	C2-a	-36	-2.5	4.18	165.0
SJ-456C-1167.0	North Betze	Primary	C2-B				235.0
SJ-456C-1167.0	North Betze	Primary	C2-B				215.0
SJ-456C-1167.0	North Betze	Primary	C2-B				215.0
SJ-456C-1167.0	North Betze	Primary	C2-B		-2.5	4.18	175.0
SJ-456C-1167.0	North Betze	Primary	C2-B	-48	-2.5	4.18	175.0
SJ-456C-1167.0	North Betze	Primary	C2-B		-2.5	4.18	185.0
SJ-456C-1167.0	North Betze	Primary	C2-B				185.0
SJ-456C-1167.0	North Betze	Primary	C2-B				195.0
SJ-456C-1167.0	North Betze	Primary	C2-B				195.0
SJ-456C-1167.0	North Betze	Primary	C2-B				195.0
SJ-456C-1167.0	North Betze	Primary	C2-B				135.0
SJ-456C-1167.0	North Betze	Primary	C2-B				175.0
SJ-456C-1167.0	North Betze	Primary	C2-B		-3.0	4.96	205.0
SJ-456C-1167.0	North Betze	Primary	C2-B		-2.3	3.87	195.0
SJ-456C-1167.0	North Betze	Primary	C2-B		-2.4	4.03	205.0
SJ-456C-1167.0	North Betze	Primary	C2-B				215.0
SJ-456C-1167.0	North Betze	Primary	C2-B				175.0
SJ-305C-1128.5	North Betze	Primary	F2a1		-3.2	5.3	195.0
SJ-305C-1128.5	North Betze	Primary	F2a1				165.0
SJ-456C-1161.9	North Betze	Primary	F8a1	-43.0	-2.4	4.03	185.0
SJ-456C-1161.9	North Betze	Primary	F8a1	-43.0	-2.5	4.18	185.0
SJ-456C-1161.9	North Betze	Primary	F8a1	-43.0	-2.5	4.18	195.0
SJ-456C-1161.9	North Betze	Primary	F8a1		-2.5	4.18	185.0
SJ-456C-1161.9	North Betze	Primary	F8a1				215.0
SJ-456C-1161.9	North Betze	Primary	F8a4				225.0
SJ-456C-1161.9	North Betze	Primary	F8a4				225.0
SJ-263C-1027.0	North Betze	Primary	F5a1				275.0
SJ-263C-1027.0	North Betze	Primary	F5a1				275.0
SJ-263C-1027.0	North Betze	Primary	F5a1				205.0
SJ-263C-1027.0	North Betze	Primary	F5a6				175.0
SJ-263C-1027.0	North Betze	Primary	F5a6				175.0
PNC-471-1019.0	North Post	$Unknown_A$	F2a1		-2.6	4.34	195.0
PNC-471-1019.0	North Post	$Unknown_A$	F2a1		-2.4	4.03	195.0
PNC-471-1019.0	North Post	$Unknown_A$	F2a1				195.0
PNC-471-1019.0	North Post	$Unknown_A$	F2a1				175.0
PNC-471-1025.0	North Post	$Unknown_A$	F3a4				195.0
PNC-471-1025.0	North Post	$Unknown_A$	F3a4				115.0
PNC-471-1025.0	North Post	$Unknown_A$	F3a5	-40.0	-1.0	1.74	135.0
PNC-471-1025.0	North Post	$Unknown_A$	F3a5				165.0

*Calculated salinity (wt% NaCl equivalent) based on equation derived by Hall et al., 1988

**Homogenization temperature (degrees Celsius)

Appendix 3. Microthermometric data collected from fluid inclusions in ore stage quartz.

Sample	Ore zone	Origin	Assemblage	~Freezing T	Ice Melting T	Salinity*	T(h)**
PNC-471-1025.0	North Post	$Unknown_A$	F3a5	-40.0	-1.0	1.74	165.0
PNC-471-1025.0	North Post	$Unknown_A$	F3a5		-1.6	2.74	245.0
PNC-471-1025.0	North Post	$Unknown_A$	F3a5				115.0
PNC-471-1025.0	North Post	$Unknown_A$	F3a5				125.0
PNC-471-1025.0	North Post	$Unknown_A$	F3a5				145.0
SJ-475C-17.6	Betze	$Unknown_A$	F2a2	-45.1	-2.3	3.87	185.0
SJ-475C-17.6	Betze	$Unknown_A$	F2a2	-45.1	-2.3	3.87	175.0
SJ-475C-17.6	Betze	$Unknown_A$	F2a2				215.0
SJ-475C-17.6	Betze	$Unknown_A$	F2a2				205.0
SJ-475C-17.6	Betze	$Unknown_A$	F2a2		-2.4	4.03	235.0
SJ-475C-17.6	Betze	$Unknown_A$	F2a2				155.0
SJ-475C-17.6	Betze	$Unknown_A$	F2a2				185.0
SJ-475C-17.6	Betze	$Unknown_A$	F2a2				255.0
SJ-475C-17.6	Betze	$Unknown_A$	F2a2				175.0
SJ-475C-17.6	Betze	$Unknown_A$	F2a2				215.0
SJ-475C-17.6	Betze	$Unknown_A$	F2a2				285.0
SJ-305C-1128.5	North Betze	$Unknown_A$	F2a2	-42.0	-3.3	5.41	205.0
SJ-305C-1128.5	North Betze	$Unknown_A$	F2a2				95.0
SJ-305C-1128.5	North Betze	$Unknown_A$	F2a3				145.0
SJ-305C-1128.5	North Betze	$Unknown_A$	F2a3				205.0
SJ-263C-1041.5	North Betze	$Unknown_A$	F4a4				175.0
SJ-263C-1041.5	North Betze	$Unknown_A$	F4a4				75.0
SJ-263C-1041.5	North Betze	$Unknown_A$	F4a4				75.0
SJ-263C-1041.5	North Betze	$Unknown_A$	F4a2	-38.5	-1.7	2.90	185.0
SJ-263C-1027.0	North Betze	$Unknown_A$	F5a1				265.0
SJ-263C-1027.0	North Betze	$Unknown_A$	F5a1				175.0
SJ-263C-1027.0	North Betze	$Unknown_A$	F5a1				135.0
SJ-263C-1027.0	North Betze	$Unknown_A$	F5a1				245.0
SJ-263C-1027.0	North Betze	$Unknown_A$	F5a2				195.0
SJ-263C-1027.0	North Betze	$Unknown_A$	F5a2				165.0
SJ-263C-1027.0	North Betze	$Unknown_A$	F5a2				195.0
SJ-263C-1027.0	North Betze	$Unknown_A$	F5a2				145.0
SJ-263C-1027.0	North Betze	$Unknown_A$	F5a3				135.0
SJ-263C-1027.0	North Betze	$Unknown_A$	F5a3				185.0
SJ-263C-1027.0	North Betze	$Unknown_A$	F5a3				255.0
SJ-263C-1027.0	North Betze	$Unknown_A$	F5a3				175.0
SJ-263C-1027.0	North Betze	$Unknown_A$	F5a8				185.0
SJ-263C-1027.0	North Betze	$Unknown_A$	F5a8				175.0
SJ-263C-1027.0	North Betze	$Unknown_A$	F5a8				165.0

*Calculated salinity (wt% NaCl equivalent) based on equation derived by Hall et al., 1988

**Homogenization temperature (degrees Celsius)

Appendix 3. Microthermometric data collected from fluid inclusions in ore stage quartz.

Sample	Ore zone	Origin	Assemblage	~Freezing T	Ice Melting T	Salinity*	T(h)**
BZ-960C-1193.8	Screamer	$Unknown_A$	F1a1				95.0
BZ-960C-1193.8	Screamer	$Unknown_A$	F1a1				185.0
BZ-960C-1193.8	Screamer	$Unknown_A$	F1a1				165.0
BZ-960C-1193.8	Screamer	$Unknown_A$	F1a1				245.0
BZ-960C-1193.8	Screamer	$Unknown_A$	F1a1				205.0
BZ-960C-1193.8	Screamer	$Unknown_A$	F1a1				145.0
BZ-960C-1193.8	Screamer	$Unknown_A$	F1a1				175.0
BZ-960C-1193.8	Screamer	$Unknown_A$	F1a1				165.0
BZ-960C-1193.8	Screamer	$Unknown_A$	F1a1				165.0
BZ-960C-1193.8	Screamer	$Unknown_A$	F1a1				205.0
BZ-960C-1193.8	Screamer	$Unknown_A$	F1a1				195.0
BZ-960C-1193.8	Screamer	$Unknown_A$	F1a1				185.0
BZ-960C-1193.8	Screamer	$Unknown_A$	F1a1				195.0
BZ-960C-1193.8	Screamer	$Unknown_A$	F1a1				215.0
BZ-960C-1193.8	Screamer	$Unknown_A$	F1a1				235.0
BZ-960C-1193.8	Screamer	$Unknown_A$	F1a1				205.0
BZ-960C-1193.8	Screamer	$Unknown_A$	F1a2				185.0
BZ-960C-1193.8	Screamer	$Unknown_A$	F1a2				175.0
BZ-960C-1193.8	Screamer	$Unknown_A$	F1a2				175.0
BZ-960C-1193.8	Screamer	$Unknown_A$	F1a3				205.0
BZ-960C-1193.8	Screamer	$Unknown_A$	F1a3				125.0
BZ-960C-1193.8	Screamer	$Unknown_A$	F1a3				125.0
BZ-960C-1193.8	Screamer	$Unknown_A$	F1a3				195.0
BZ-960C-1193.8	Screamer	$Unknown_A$	F1a4				135.0
BZ-960C-1193.8	Screamer	$Unknown_A$	F1a4	-33.2	-1.0	1.74	185.0
BZ-960C-1193.8	Screamer	$Unknown_A$	F1a4				125.0
BZ-960C-1193.8	Screamer	$Unknown_A$	F1a4	-40.5	-1.0	1.74	165.0
BZ-960C-1193.8	Screamer	$Unknown_A$	F1a4				175.0
BZ-960C-1193.8	Screamer	$Unknown_A$	F1a4				145.0
BZ-960C-1193.8	Screamer	$Unknown_A$	F1a4				165.0
BZ-960C-1193.8	Screamer	$Unknown_A$	F1a4				175.0
BZ-960C-1193.8	Screamer	$Unknown_A$	F1a4				175.0
BZ-960C-1193.8	Screamer	$Unknown_A$	F1a4				175.0
BZ-960C-1193.8	Screamer	$Unknown_A$	F1a4	-36.2	-1.7	2.90	195.0
BZ-960C-1193.8	Screamer	$Unknown_A$	F1a4				185.0
BZ-960C-1193.8	Screamer	$Unknown_A$	F1a4				195.0
BZ-960C-1193.8	Screamer	$Unknown_A$	F1a4				185.0

*Calculated salinity (wt% NaCl equivalent) based on equation derived by Hall et al., 1988

**Homogenization temperature (degrees Celsius)

Appendix 3. Microthermometric data collected from fluid inclusions in ore stage quartz.

Sample	Ore zone	Origin	Assemblage	~Freezing T	Ice Melting T	Salinity*	T(h)**
BZ-960C-1193.8	Screamer	$Unknown_A$	F1a5				125.0
BZ-960C-1193.8	Screamer	$Unknown_A$	F1a5				125.0
BZ-960C-1193.8	Screamer	$Unknown_A$	F1a5				185.0
BZ-960C-1193.8	Screamer	$Unknown_A$	F1a5				145.0
BZ-960C-1193.8	Screamer	$Unknown_A$	F1a5				185.0
BZ-960C-1193.8	Screamer	$Unknown_A$	F1a5				205.0
BZ-960C-1193.8	Screamer	$Unknown_A$	F1a7	-42.7	-2.4	4.03	165.0
BZ-960C-1193.8	Screamer	$Unknown_A$	F1a7	-40.5	-2.4	4.03	175.0
BZ-960C-1193.8	Screamer	$Unknown_A$	F1a7				125.0
BZ-960C-1193.8	Screamer	$Unknown_A$	F1a7				185.0
BZ-960C-1193.8	Screamer	$Unknown_A$	F1a8				145.0
BZ-960C-1193.8	Screamer	$Unknown_A$	F1a8				135.0
BZ-960C-1193.8	Screamer	$Unknown_A$	F1a8				125.0
BZ-960C-1193.8	Screamer	$Unknown_A$	F1a8				175.0
BZ-960C-1193.8	Screamer	$Unknown_A$	F1a9	-41.2	-2.3	3.87	165.0
BZ-960C-1193.8	Screamer	$Unknown_A$	F1a9				165.0
BZ-960C-1193.8	Screamer	$Unknown_A$	F1a9		-3.2	5.26	265.0
BZ-960C-1193.8	Screamer	$Unknown_A$	F1a9				195.0
BZ-960C-1193.8	Screamer	$Unknown_A$	F1a9				85.0
BZ-960C-1193.8	Screamer	$Unknown_A$	F1a9	-41.5	-2.4	4.03	195.0
SJ-552C-1054.5	Screamer	$Unknown_A$	F3a3	-43.6	-3.3	5.41	185.0
SJ-552C-1054.5	Screamer	$Unknown_A$	F3a3	-38.5	-2.8	4.65	185.0
SJ-552C-1054.5	Screamer	$Unknown_A$	F3a3	-42.9	-1.9	3.23	195.0
SJ-552C-1054.5	Screamer	$Unknown_A$	F3a3	-42.5	-2.7	4.49	165.0
SJ-305C-1041.2	North Betze	Secondary	C1-A-1				185.0
SJ-305C-1041.2	North Betze	Secondary	C1-A-1				185.0
SJ-305C-1041.2	North Betze	Secondary	C1-A-1				175.0
SJ-305C-1041.2	North Betze	Secondary	C1-A-1				105.0
SJ-305C-1041.2	North Betze	Secondary	C1-A-1		-2.5	4.18	175.0
SJ-305C-1041.2	North Betze	Secondary	C1-A-1		-2.5	4.18	185.0
SJ-305C-1041.2	North Betze	Secondary	C1-A-1				225.0
SJ-305C-1041.2	North Betze	Secondary	C1-A-1				185.0
SJ-305C-1041.2	North Betze	Secondary	C1-A-1		-2.6	4.34	215.0
SJ-305C-1041.2	North Betze	Secondary	C1-A-1				105.0
SJ-305C-1041.2	North Betze	Secondary	C1-A-1				215.0
SJ-305C-1041.2	North Betze	Secondary	C1-A-1				185.0
SJ-305C-1041.2	North Betze	Secondary	C1-A-1		-2.9	4.80	245.0
SJ-263C-1027.0	North Betze	Secondary	F5a9				255.0
SJ-263C-1027.0	North Betze	Secondary	F5a9				195.0
BZ-960C-1193.8	Screamer	Secondary	F1a6				165.0

*Calculated salinity (wt% NaCl equivalent) based on equation derived by Hall et al., 1988

**Homogenization temperature (degrees Celsius)

Appendix 3. Microthermometric data collected from fluid inclusions in ore stage quartz.

Sample	Ore zone	Origin	Assemblage	~Freezing T	Ice Melting T	Salinity*	T(h)**
BZ-960C-1193.8	Screamer	Secondary	F1a6				205.0
BZ-960C-1193.8	Screamer	Secondary	F1a6				185.0
BZ-960C-1193.8	Screamer	Secondary	F1a6				175.0
PNC-471-1025.0	North Post	$Unknown_S$	F3a2				85.0
PNC-471-1025.0	North Post	$Unknown_S$	F3a3				85.0
SJ-473C-781.5	Betze	$Unknown_S$	F1a1		-2.6	4.34	195.0
SJ-456C-1161.9	North Betze	$Unknown_S$	F8a3				175.0
SJ-263C-1027.0	North Betze	$Unknown_S$	F5a9				195.0

*Calculated salinity (wt% NaCl equivalent) based on equation derived by Hall et al., 1988

**Homogenization temperature (degrees Celsius)

APPENDIX IV

STABLE ISOTOPE DATA

$\delta^{18}O$ and δD signatures were measured in all stages of the quartz paragenesis. $\delta^{18}O$ signatures were measured by in-situ secondary ion mass spectrometry (SIMS) analyses. SIMS was integrated with cathodoluminescence studies to pinpoint discrete generations of quartz at Betze-Post.

δD signatures of inclusion fluids in ore stage quartz were measured using a helium carrier continuous flow thermochemical conversion gas chromatograph coupled to a Delta mass spectrometer. $\delta^{18}O$ analyses of quartz samples that host analyzed fluid inclusions were measured using conventional techniques by Clayton and Mayeda, 1963). Samples were sent to the USGS in Denver and analyses were conducted by Al Hofstra.

The $\delta^{18}O$ signatures of the fluid responsible for the precipitation of ore stage quartz were calculated using the fractionation equation between quartz and water as derived by Matsuhisa et al. (1979). This equation calculates a fractionation factor between quartz and the fluid assuming that they are in equilibrium with one another. A temperature of 200ºC was selected based on measured fluid inclusion data and a fractionation factor of 12‰ was calculated for this study. At 200°C quartz is enriched relative to the fluid by 12 ‰.

Appendix 4. Stable isotope values measured in quartz generations at Betze-Post.

Sample	Ore zone	Mineral	$\delta^{18}O_{QTZ}$ (‰)*	Error (‰)	δD_{H2O} (‰)**	Error (‰)	$\delta^{18}O_{Qtz}$(‰)***	Error (‰)	$\delta^{18}O_{H2O}$[1] (‰)
Pre-ore-stage									
SJ-305C-1041.2	North Betze	quartz	19.26	2.33					
SJ-305C-1041.2	North Betze	quartz	17.76	1.17					
SJ-305C-1041.2	North Betze	quartz	19.21	1.40					
Ore Stage									
RM97-2C-633.0	Deep Post	jasperoid	24.11	1.38					12.11
RM97-2C-633.0	Deep Post	jasperoid	2.26	1.36					-9.74
P-175C-1245.0	Deep Post	jasperoid	23.96	1.33					11.96
P-175C-1245.0	Deep Post	jasperoid	24.01	1.13					12.01
RM97-2C-488.0	Deep Post	jasperoid	25.30	1.56					13.30
RM97-9C-315.6	Deep Post	jasperoid	20.90	1.28					8.90
SJ-562CA-664.1	Betze	jasperoid	6.05	3.71					-5.95
SJ-562CA-664.1	Betze	jasperoid	9.80	1.87					-2.20
SJ-305C-1041.2	North Betze	jasperoid	15.62	1.27					3.62
SJ-305C-1041.2	North Betze	jasperoid			-107	5	13.8	0.2	1.8
SJ-305C-1041.2	North Betze	jasperoid			-127	5	13.8	0.2	1.8
SJ-305C-1041.2	North Betze	jasperoid			-142	5	13.8	0.2	1.8
SJ-305C-1069.7	North Betze	jasperoid	11.98	1.62					-0.02
SJ-305C-1069.7	North Betze	jasperoid	12.22	1.35					0.22
SJ-305C-1069.7	North Betze	jasperoid	10.98	1.34					-1.02
SJ-457C-1052.5	North Betze	jasperoid	3.80	1.23					-8.20
SJ-457C-1052.5	North Betze	jasperoid	13.27	1.17					1.27
SJ-457C-1052.5	North Betze	jasperoid	15.92	1.35					3.92

* Measured $\delta^{18}O$ signature of quartz using in-situ secondary ion mass spectrometry (SIMS) analysis

** Measured δD signature of inclusion fluids using helium carrier continuous flow thermochemical conversion gas chromatography

*** Measured $\delta^{18}O$ signature of quartz host using conventional methods by Clayton and Mayeda (1963).

[1] Calculated $\delta^{18}O$ signature of ore stage fluids using fractionation equation for quartz↔H_2O from Matsuhisa et. al., 1979; calculated using a trapping T of 200°C and assuming fluid and mineral are in equilibrium

Appendix 4. Stable isotope values measured in quartz generations at Betze-Post.

Sample	Ore zone	Mineral	$\delta^{18}O_{QTZ}$ (‰)*	Error (‰)	δD_{H2O} (‰)**	Error (‰)	$\delta^{18}O_{Qtz}$ (‰)***	Error (‰)	$\delta^{18}O_{H2O}$[1] (‰)
SJ-457C-1052.5	North Betze	jasperoid	2.55	1.54					-9.45
SJ-457C-1052.5	North Betze	jasperoid	-0.19	1.45					-12.19
SJ-456C-1167.0	North Betze	jasperoid	4.71	1.66					-7.29
SJ-456C-1167.0	North Betze	jasperoid	9.20	5.46					-2.80
SJ-456C-1167.0	North Betze	jasperoid			-175	5	11.6	0.2	-0.4
SJ-263C-1042.1	North Betze	jasperoid	18.97	3.18					6.97
SJ-457C-1052.0	North Betze	jasperoid	23.71	1.39					11.71
SJ-457C-1052.0	North Betze	jasperoid	4.21	1.42					-7.79
SJ-457C-1052.0	North Betze	jasperoid	8.05	1.36					-3.95
SJ-457C-1052.0	North Betze	jasperoid	8.70	1.56					-3.30
SJ-263C-1051.0	North Betze	jasperoid	13.09	1.51					1.09
SJ-457C-1026.0	North Betze	jasperoid	8.85	1.11					-3.15
SJ-457C-1026.0	North Betze	jasperoid	10.79	3.01					-1.21
SJ-456C-1161.9	North Betze	jasperoid			-171	5	11.2	0.2	-0.8
SJ-456C-1161.9	North Betze	jasperoid			-161	5	11.2	0.2	-0.8
SJ-456C-1161.9	North Betze	jasperoid			-175	5	11.2	0.2	-0.8
BZ-960C-1197.5	Screamer	jasperoid	5.51	2.12					-6.49
BZ-915C-1073.1	Screamer	jasperoid	24.56	1.85					12.56
BZ-915C-1073.1	Screamer	jasperoid	9.15	1.13					-2.85
Late-ore-stage									
P-175C-1312.0	Deep Post	drusy quartz	14.48	1.62					2.48
P-175C-1312.0	Deep Post	drusy quartz	6.20	2.02					-5.8
SJ-562CA-664.1	Betze	drusy quartz	4.36	2.29					-7.64
SJ-305C-1041.2	North Betze	drusy quartz	5.47	4.18					-6.53

* Measured $\delta^{18}O$ signature of quartz using in-situ secondary ion mass spectrometry (SIMS) analysis

** Measured δD signature of inclusion fluids using helium carrier continuous flow thermochemical conversion gas chromatography

*** Measured $\delta^{18}O$ signature of quartz host using conventional methods by Clayton and Mayeda (1963).

[1] Calculated $\delta^{18}O$ signature of ore stage fluids using fractionation equation for quartz↔H_2O from Matsuhisa et. al., 1979; calculated using a trapping T of 200°C and assuming fluid and mineral are in equilibrium

Appendix 4. Stable isotope values measured in quartz generations at Betze-Post.

Sample	Ore zone	Mineral	$\delta^{18}O_{QTZ}$ (‰)*	Error (‰)	δD_{H2O} (‰)**	Error (‰)	$\delta^{18}O_{Qtz}$ (‰)***	Error (‰)	$\delta^{18}O_{H2O}$[1] (‰)
SJ-305C-1069.7	North Betze	drusy quartz	7.94	1.30					-4.06
SJ-305C-1069.7	North Betze	drusy quartz	3.20	1.29					-8.80
SJ-305C-1069.7	North Betze	drusy quartz	3.60	1.39					-8.40
SJ-305C-1069.7	North Betze	drusy quartz	12.19	2.00					0.19
SJ-305C-1069.7	North Betze	drusy quartz	6.85	2.07					-5.15
SJ-305C-1069.7	North Betze	drusy quartz	11.98	1.42					-0.02
SJ-305C-1069.7	North Betze	drusy quartz	9.83	1.25					-2.17
SJ-456C-1167.0	North Betze	drusy quartz	8.55	1.86					-3.45
SJ-456C-1167.0	North Betze	drusy quartz	6.85	1.62					-5.15
SJ-456C-1167.0	North Betze	jsp/drusy quartz			-190	5	10.5	0.2	-1.5
SJ-457C-1101.8	North Betze	drusy quartz	12.09	2.32					0.09
SJ-457C-1101.8	North Betze	drusy quartz	12.14	2.05					0.14
BZ-960C-1197.5	Screamer	drusy quartz	3.36	1.73					-8.64
BZ-960C-1197.5	Screamer	drusy quartz	1.67	1.83					-10.33
Post-ore-stage									
SJ-475C-150.0	Betze	drusy quartz	3.21	1.61					
SJ-475C-150.0	Betze	drusy quartz	-0.03	2.07					
SJ-475C-150.0	Betze	drusy quartz	3.01	2.13					
SJ-475C-150.0	Betze	drusy quartz	1.17	1.93					
SJ-475C-150.0	Betze	drusy quartz	-0.83	2.52					
SJ-475C-150.0	Betze	drusy quartz	2.76	2.15					
SJ-475C-150.0	Betze	drusy quartz	-0.08	2.02					
SJ-475C-150.0	Betze	drusy quartz	0.22	1.83					

* Measured $\delta^{18}O$ signature of quartz using in-situ secondary ion mass spectrometry (SIMS) analysis

** Measured δD signature of inclusion fluids using helium carrier continuous flow thermochemical conversion gas chromatography

*** Measured $\delta^{18}O$ signature of quartz host using conventional methods by Clayton and Mayeda (1963).

[1] Calculated $\delta^{18}O$ signature of ore stage fluids using fractionation equation for quartz↔H_2O from Matsuhisa et. al., 1979; calculated using a trapping T of 200°C and assuming fluid and mineral are in equilibrium

Appendix 4. Stable isotope values measured in quartz generations at Betze-Post.

Sample	Ore zone	Mineral	$\delta^{18}O_{QTZ}$ (‰)*	Error (‰)	δD_{H2O} (‰)**	Error (‰)	$\delta^{18}O_{Qtz}$ (‰)***	Error (‰)	$\delta^{18}O_{H2O}$[1] (‰)
SJ-475C-150.0	Betze	drusy quartz	1.67	2.52					
SJ-475C-150.0	Betze	drusy quartz	1.82	1.82					
SJ-475C-150.0	Betze	drusy quartz	5.16	2.34					
SJ-475C-150.0	Betze	drusy quartz	5.96	1.73					
SJ-475C-150.0	Betze	drusy quartz	6.01	1.75					
SJ-562CA-664.1	Betze	drusy quartz	2.61	1.74					
SJ-305C-1041.2	North Betze	drusy quartz	9.22	1.55					
SJ-305C-1041.2	North Betze	drusy quartz	10.21	1.67					
SJ-305C-1041.2	North Betze	drusy quartz	10.48	1.31					
SJ-305C-1069.7	North Betze	drusy quartz	12.72	1.13					
SJ-305C-1069.7	North Betze	drusy quartz	2.46	1.88					
Pit S1-120	North Betze	drusy quartz			-183	5	4.8	0.2	
Pit S1-120	North Betze	drusy quartz			-184	5	4.8	0.2	
Pit S1-120	North Betze	drusy quartz			-163	5	3.4	0.2	
Pit S1-120	North Betze	drusy quartz			-174	5	3.4	0.2	
BZ-960C-1197.5	Screamer	drusy quartz	-3.77	1.93					

* Measured $\delta^{18}O$ signature of quartz using in-situ secondary ion mass spectrometry (SIMS) analysis

** Measured δD signature of inclusion fluids using helium carrier continuous flow thermochemical conversion gas chromatography

*** Measured $\delta^{18}O$ signature of quartz host using conventional methods by Clayton and Mayeda (1963).

[1] Calculated $\delta^{18}O$ signature of ore stage fluids using fractionation equation for quartz↔H_2O from Matsuhisa et. al., 1979; calculated using a trapping T of 200°C and assuming fluid and mineral are in equilibrium

REFERENCES

Alvarez, A. R. and Noble, D. C., 1988, Sedimentary rock-hosted disseminated precious metal mineralization at Purisima Concepcion, Yauricocha district, central Peru: Economic Geology, v. 83, p. 1368-1378.

Arehart, G. B., Chryssoulis, S. L., and Kesler, S. E., 1993, Gold and arsenic in iron sulfides from sediment-hosted disseminated gold deposits: Implications for depositional processes: Economic Geology, v. 88, p. 171-185.

Arehart, G.B., 1996, Characteristics and origin of sediment-hosted disseminated gold deposits: A review: Ore Geology Reviews, v. 11, p. 383-403.

Ashley, R. P., Cunningham, C. G., Bostick, N. H., Dean, W. E., and Chou, I. M., 1991, Geology and geochemistry of three sedimentary-rock-hosted disseminated gold deposits in Guizhou Province, People's Republic of China: Ore Geology Review, v. 6, p. 133-151.

Bakken, B. M., 1990, Gold mineralization, wall-rock alteration, and the geochemical evolution of the hydrothermal system in the main ore-body, Carlin mine: Unpublished Ph.D. dissertation, Stanford, CA, Stanford University, 236p.

Bakken, B.M., and Einaudi, M.T., 1986, Spatial and temporal relations between wall rock alteration and gold mineralization, Main pit, Carlin Gold Mine, Nevada, U.S.A.: Macdonald, A.J., ed., Gold '86: Willowdale, ON, Canada, Konsult International, p. 388-403.

Bettles, K.H., 2002, Exploration and geology, 1962 to 2002, at the Goldstrike property, Carlin trend, Nevada: Economic Geology Special Publication 9, p. 275-298.

Christensen, O. D., 1995, The Carlin Trend giant gold camp: Is it the strata, the structure, or the stocks? *in* Clarke, A. H. ed., Proceedings of the second Giant Ore Deposits Workshop, Ontario, Canada, p. 340-357.

Clayton, R. N. and Mayeda, T. K., 1963, The use of bromine pentafluoride in the extraction of oxygen from oxides and silicates for isotopic analysis: Geochemica et Cosmochemica Acta, v. 27, p. 43-52.

Cline, J.S., 2001, Timing of gold and arsenic sulfide mineral deposition at the Getchell Carlin-type gold deposit, North-central Nevada: Economic Geology, v. 96, p. 75-90.

Cline, J.S. and Hofstra, A.H., 2000, Ore-fluid evolution at the Getchell Carlin-type gold deposit, Nevada, USA: European Journal of Mineralogy, v. 12, p. 195-212.

Cline, J.S., Hofstra, A.H., Landis, G.P., and Rye, R.O., 1996, Stable isotope and fluid inclusion evidence for a deep sourced ore fluid at the Getchell Carlin-type gold deposit, Nevada [ext. abs.]: Pan-American Current Research on Fluid Inclusions, Sixth Biennial, Madison, Wisconsin, May 30-June 1, 1996, Programs and abstracts, p. 33-35.

Cline, J.S., Stuart, F.M., Hofstra, A.H., Tretbar, D.R., Riciputi, L., and Premo, W., 2002, He, Nd, and stable isotopes constraints on Carlin-type ore fluid components, Getchell, NV, USA: Geological Society of America Abstracts with Program, v. 34, no. 6, p. 141.

Cline, J. S., Hofstra, A. H., Muntean, J., L., Tosdal, R. M., and Hickey, K. A., 2003, Sedimentary rock-hosted disseminated gold deposits: Part 1, Carlin-type gold deposits in Nevada, USA: District comparisons, essential features, and viable models: 100th Anniversary Volume, Society of Economic Geologists, Littleton, Colorado (In review).

Cohen, A.J., 1960, Substitutional and interstitial aluminum impurity in quartz, structure, and color center interrelationships: Journal of Physical and Chemical Solids, v. 13, p. 321-325.

Emsbo, P, 1999, Origin of the Meikle high grade gold deposit from the superposition of Late Devonian sedex and mid-Tertiary Carlin-type gold mineralization: Unpublished Ph.D. thesis, Golden, Colorado, Colorado School of Mines, 394 p.

Emsbo, P., Hutchinson, R.W., Hofstra, A.H., Volk, J.A., Bettles, K.H., Baschuk, G.J., and Johnson, C.A., 1999, Syngenetic Au on the Carlin trend: Implications for Carlin-type deposits: Geology, v. 27, p. 59-62.

Emsbo, P., Hofstra, A.H., Lauha, E.A., Griffin, G.L., and Hutchinson, R.W., 2003, Origin of high-grade gold ore, source of ore fluid components, and genesis of the Meikle and neighboring Carlin-type deposits, Northern Carlin Trend, Nevada: Economic Geology, v. 98, p. 1069-1100.

Evans, J.G., 1980, Geology of the Rodeo Creek and Welches Canyon Quadrangles, Eureka County, Nevada: U.S. Geological Survey Bulletin 1473, 81 p.

Faure, K., 2003, δD values of fluid inclusion water in quartz and calcite ejecta from active geothermal systems; do values reflect those of original hydrothermal water?: Economic Geology, v. 98, p. 657-660.

Furley, R., 2001, Sequence stratigraphic framework for the Silurian-Devonian Bootstrap Limestone, Roberts Mountains, and Devonian Popovich formations, northern Carlin Trend, Elko and Eureka counties, Nevada: Unpublished thesis, Colorado School of Mines, Golden, CO, 194p.

Garwin, S. L., Hendri, D., and Lauricella, P. F., 1995, The geology of the Mesel deposit, north Sulawesi, Indonesia: Proceedings of the PACRIM '95 conference, p. 221-226.

Grauch, V. J. S., Rodriguez, B. D., and Wodden, J. L., 2003, Geophysical and Isotopic constraints on crustal structure related to mineral trends in north-central Nevada and implications for tectonic history: Economic Geology, v. 98, p. 269-286.

Groff, J.A., Heizler, M.T., McIntosh, W.C., and Norman, D.I., 1997, $^{40}Ar/^{39}Ar$ dating and mineral paragenesis for Carlin-type gold deposits along the Getchell trend, Nevada: Evidence for Cretaceous and Tertiary gold mineralization: Economic Geology, v. 92, p. 601-622.

Henkelman, C., 2004, Pyrite Geochemistry across the Betze-Post Deposit, Northern Carlin Trend, Nevada: Unpublished M.S. thesis, Las Vegas, University of Nevada, 150 p.

Henkelman, C., 2004, Can variations in pyrite chemistry across the Betze-Post deposit provide clues to gold deposition and improve exploration techniques?: Proceedings of the Ralph J. Roberts Center for Research in Economic Geology (CREG) 2003 Year-End Research Meeting.

Henkelman, C., Lubben, J.D., and Cline, J.S., 2003, Variations in Pyrite chemistry as clues to gold deposition at the Goldstrike system, Carlin Trend, Nevada USA: in Eliopoulos, D. G., eds, Mineral Exploration and Sustainable Development, Proceedings of the Seventh Biennial SGA Meeting, Athens, Greece, v. 2, p. 981-984.

Hickey, K. A., 2003, Restoration of the Late-Eocene landscape in the Carlin-Jerritt Canyon mining district: Constraining depth of mineralization for Carlin-type Au-deposits using low-temperature apatite thermochronology: Geological Society of America Abstracts with Programs, v. 35, p. 358.

Hickey, K. A., Haynes, S. R., Tosdal, R. M., and Mortensen, J. K., 2003, Cretaceous-Palaeogene denudation, volcanism and faulting in the Carlin-Jerritt Canyon mining district, northeastern Nevada: implications for the paleogeographic and tectonic environment of Carlin-type gold deposits: in Eliopoulos, D. G., Mineral Exploration and Sustainable Development, Proceedings of the Seventh Biennial SGA Meeting, Athens, Greece, v. 2, p. 685-688.

Hoefs, J., 1997, Stable Isotope Geochemistry: Berlin, Springer, 202 p.

Hofstra, A.H., 1994, Geology and genesis of the Carlin-type gold deposits in the Jerritt Canyon district, Nevada: Unpublished Ph.D. dissertation, Boulder, University of Colorado, 719 p.

Hofstra, A. H., Snee, L. W., Rye, R. O., Folger, H. W., Phinisey, J. D., Loranger, R. J., Dahl, A. R., Naeser, C. W., Stein, H. J., and Lewchuck, M., 1999, Age constraints on Jerritt Canyon and other Carlin-type gold deposits in the western United States – relationship to mid-Tertiary extension and magmatism: Economic Geology, v. 94, p. 769-802.

Hofstra, A.H., Leventhal, J.S., Northrop, H.R., Landis, G.P., Rye, R.O., Birak, D.J., and Dahl, A.R., 1991, Genesis of sediment-hosted disseminated-gold deposits by fluid mixing and sulfidization: Chemical-reaction-path modeling of ore-depositional processes documented in the Jerritt Canyon district, Nevada: Geology, v. 19, p. 36-40.

Hofstra, A.H. and Cline, J.S., 2000, Characteristics and models for Carlin-type gold deposits: Vikre, P., Thompson, T.B., Bettles, K., Christensen, O., and Parratt, R. eds., Society of Economic Geology Reviews, v. 13, p. 163-220.

Holland, P. T., Beaty, D. W., and Snow, G. G., 1988, Comparitive elemental and oxygen isotope geochemistry of jasperoid in the northern Great Basin: Evidence for distinctive fluid evolution in gold-producing hydrothermal systems: Economic Geology, v. 83, p. 1401-1423.

Hotz, P. W. and Willden, R., 1964, Geology and mineral deposits of the Osgood Mountains quadrangle, Humboldt County, Nevada: U.S. Geological Survey Professional Paper 431, 128p.

Ilchick, R. P., 1994, Geology and geochemistry of the Vantage gold deposits, Alligator Ridge-Bald Mountain mining district, Nevada: Economic Geology, v. 85, p. 50-75.

Kalceff, M.A.S., Phillips, M.R., Moon, A.R., and Kalceff, W., 2000, Cathodoluminescence micro characterization of silicon dioxide polymorphs: in Pagel, M, Barbin, V., and Ohnenstetter, D., eds., Cathodoluminescence in Geosciences, Springer, Berlin Heidelberg New York, 514 p.

Kerkhof, A.M. and Simon, K., 2001, Trace element redistribution in metamorphic quartz and fluid inclusion modification: Observations by cathodoluminescence: European Current Research On Fluid Inclusions, Porto 2001, v. 7, p. 447-450.

Kuehn, C.A. and Rose, A.W., 1992, Geology and geochemistry of wall-rock alteration at the Carlin-type gold deposit, Nevada: Economic Geology, v. 87, p. 1697-1721.

Kuehn, C.A. and Rose, A.W., 1995, Carlin gold deposits, Nevada: Origin in a deep zone of mixing between normally pressured and overpressured fluids: Economic Geology, v. 90, p. 17-36.

Lamb, J.B., 1995, A petrographic and fluid inclusion study of the Purple Vein and Post-Betze orebodies, Carlin, Nevada: Unpublished M.S. thesis, Las Vegas, University of Nevada, 126 p.

Lamb, J.B. and Cline, J.S., 1997, Depths of formation of the Meikle and Post-Betze deposits: Society of Economic Geologists Guidebook Series, v. 28, p. 101-108.

Leonardson, R.W., and Rahn, J.E., 1996, Geology of the Betze-Post gold deposits, Eureka County, Nevada, *in* Coyner, A.R., and Fahey, P.L., eds., Geology and Ore Deposits of the American Cordillera: Geological Society of Nevada Symposium Proceedings, v. 1, p. 61-94.

Mao, S. H., 1991, Occurrence and distribution of invisible gold in a Carlin-type gold deposit in China: American Mineralogist, v. 76, 1964-1972.

Matsuhisa, Y., Goldsmith, J.R., and Clayton, R.N., 1979, Oxygen isotopic fractionation in the system quartz-albite-anorthite-water: Geochemica et Cosmochimica Acta, v. 43, p. 1131-1140.

Muller, A., 2000, Cathodoluminescence and characteristics of defect structures in quartz with applications to the study of granitic rocks: Ph.D. Dissertation, zur Erlangung des Doktorgrades der Mathematisch-Naturwissenschaftlichen Fakultaten der Georg-August-Universitat zu Gottingen, 229 p.

Nevada Bureau of Mines and Geology, 1997, Nevada Geology: Newsletter of the NBMG, Reno, Nevada, v. 32, 4 p.

Nutt, C. J. and Hofstra, A. H., 2003, Alligator Ridge district, east-central Nevada: Carlin-type gold mineralization at shallow depths: Economic Geology, v. 98, p. 1225-1241.

Radtke, A.S., Rye, R.O., and Dickson, F.W., 1980, Geology and stable isotope studies of the Carlin gold deposit, Nevada: Economic Geology, v.75, p. 641-672.

Radtke, A. S., 1985, Geology of the Carlin deposit, Nevada: U.S. Geological Survey Professional Paper 1267, 124p.

Roberts, R.J., Radtke, A.S., Coats, R.R., Silberman, M.L., and McKee, E.H., 1971, Gold-bearing deposits in north-central Nevada and southwestern Idaho, with a section on periods of plutonism in north-central Nevada: Economic Geology, v. 66, p. 15-33.

Roedder, E. and Bodnar, R. J., 1980, Geologic pressure determinations from fluid inclusion studies: Annual Review of Earth and Planetary Sciences, v. 8, p. 263-301.

Shigehiro, M., 1999, Mineral paragenesis and ore fluids at the Turquoise Ridge gold deposit, Nevada: Unpublished M.S. thesis, Las Vegas, University of Nevada, 152 p.

Silberling, N. J. and Roberts, R. J., 1962, Pre-Tertiary stratigraphy and structure of northwest Nevada: Geological Society of America Special Paper, v. 72, 58p.

Sillitoe, R. H., and Bonham, H. F. Jr., 1990, Sediment-hosted deposits: Distal products of magmatic-hydrothermal systems: Geology, v. 18, p. 157-161.

Sprunt, E., 1981, Causes of quartz cathodoluminescence colors: Scanning Electron Microscopy, p. 525-535.

Stewart, J. H., 1980, Geology of Nevada: Nevada Bureau of Mines and Geology Special Publication, v. 4, 136p.

Thorman, C. H., Ketner, K. B., and Peterson, F., 1990, The Elko orogeny – Late Jurassic orogenesis in the Cordilleran miogeocline: Geological Society of America Abstracts with Programs, v. 22, p. 88.

Thorman, C. H., Ketner, K. B., and Peterson, F., 1992, The Middle to Late Jurassic Elko orogeny in eastern Nevada and western Utah: Geological Society of America Abstracts with Programs, v. 24, p. 66.

Tosdal, R.M., Wooden, J.L., and Kistler, R.W., 2000, Inheritance of Nevadan mineral belts from Neoproterozoic continental breakup: *in* Cluer, J.K., Price, J.G., Struhsacker, E.M., Hardyman, R.F., and Morris, C.L., eds., Geology and Ore Deposits 2000: The Great Basin and Beyond: Geological Society of Nevada Symposium Proceedings, p. 451-466.

Volk, J.A., Weakly, C., Penick, M., and Lander, A., 2001, Structural geology of the Goldstrike property, north-central Nevada: Geological Society of Nevada Special Publication 33, p. 361-379.

Watt, G.R., Wright, P, Galloway, S, and McLean, C, 1997, Cathodoluminescence and trace element zoning in quartz phenocrysts and xenocrysts: Geochmica et Cosmochimica Acta, v. 61, p. 4337-4348.

Weaver, K. D., 2001, The geochemistry of gold-bearing and gold-free pyrite and marcasite from the Getchell gold deposit, Humboldt County, Nevada: Unpublished M.S. thesis, Las Vegas, Nevada, University of Nevada Las Vegas, 133 p.

Weaver, K. D. and Cline, J. S., 1999, Geochemistry of ore-stage and non-ore pyrite and marcasite from the Getchell Carlin-type gold deposit, Nevada: Geological Society of America Abstracts with Programs, v. 31, p. A106.

Wells, D. J. and Mullens, T. E., 1973, Gold-bearing arsenian pyrite determined by microprobe analysis, Cortez and Carlin Gold Mines, Nevada: Economic Geology, v. 68, p. 187-201.

VITA

Graduate College
University of Nevada, Las Vegas

Jared D. Lubben

Local Address:
4775 Summit Ridge Drive
Apt 2040
Reno, NV 89503

Degrees:
Bachelor of Science, Geology, 2000
Winona State University

Master of Science, Geology, 2004
University of Nevada, Las Vegas

Special Honors and Awards:
UNLV GREAT (Graduate Research Training) Assistantship, (2003)
UNLV Graduate Student Travel Grant, $400.00, (2003)
Ralph Roberts Center for Research in Economic Geology (CREG) Research Grant, (2003), (2002)
UNLV Geoscience Departmental Research Grant, $500.00 (2003), $750.00 (2002)
Society of Economic Geologists Research Grant, $1000.00 (2002)
Geological Society of America Research Grant, $1800.00 (2002)
Winona State University Academic Achievement Award (2000)
Winona State University Dean's List (2000)

Publications:

Lubben, J.D., Cline, J.S., and Fairhurst, R.J., 2003, Cathodoluminescence in quartz: Clues to ore paragenesis and ore fluid properties at the Goldstrike Carlin-type gold deposit, northern Nevada: GSA Abstracts with Programs, v. 35, n. 6 p. 267

Henkelman, C., Lubben, J.D., and Cline, J.S., 2003, Variations in Pyrite Chemistry as Clues to Gold Deposition at the Goldstrike System, Carlin Trend, Nevada USA: Mineral Exploration and Sustainable Development, Proceedings of the Seventh Biennial SGA Meeting, Athens, Greece, p. 981-984

Lubben, J.D., Henkelman, C., and Cline, J.S., 2003, Using Fluid Inclusions to Constrain Ore Fluid Properties at the Goldstrike Carlin-type Gold System, Nevada, USA: ACTA Mineralogica-Petrographica Abstract Series, Proceedings of the 17th Biennial ECROFI Meeting, Szeged, Hungary, v. 2, p. 114-115

Lubben, J.D., Henkelman, C., and Cline, J.S., 2003, Chemistry, textures, and fluid Inclusions in quartz: Clues to ore fluid sources at the North Betze ore zone, Goldstrike Carlin-type gold system, Northern Carlin Trend, Nevada: GSA Abstracts with Programs. v. 35, n. 4, p. 60-61

Thesis Title: Silicification across the Betze-Post Carlin-type Au deposit: Clues to ore fluid properties and sources, Northern Carlin Trend, Nevada

Thesis Examination Committee:

Chairperson, Dr. Jean S. Cline, Ph. D.
Committee Member, Dr. Eugene I. Smith, Ph. D.
Committee Member, Dr. Robert J. Fairhurst, Ph. D.
Graduate Faculty Representative, Dr. Barbara A. Luke, Ph. D.